Cloud Microphysics in Global Cloud Resolving Models

Tatsuya Seiki[1,1], Woosub Roh[2,2], and Masaki Satoh[2,2]

[1]Japan Agency for Marine-Earth Science and Technology
[2]Atmosphere and Ocean Research Institute, The University of Tokyo

November 30, 2022

Abstract

Global cloud resolving models (GCRMs) are a new type of general circulation model that explicitly calculates the growth of cloud systems with fine spatial resolutions and more than 10 GCRMs have been developed at present. This chapter of the monograph reviews cloud microphysics schemes used in GCRMs with introductions to the recent progress and researches with GCRMs. Especially, research progress using a pioneer of GCRMs, Nonhydrostatic ICosahedral Atmospheric Model (NICAM), is focused. Since GCRMs deal with climatology and meteorology, it is a challenging issue to establish cloud microphysics schemes for GCRMs. A brief history of the development of cloud microphysics schemes and cloud-radiation coupling in NICAM is described. In addition, current progress in analytical techniques using satellite simulators is described. The combined use of multi-optical sensors enables us to constrain uncertain processes in cloud microphysics without artificial tuning. As a result, cloud microphysics schemes used in the NICAM naturally represent cloud systems, and hence, the radiative budget is well balanced with little optimization. Finally, a new satellite and a ground validation campaign are introduced for future work.

Cloud Microphysics in Global Cloud Resolving Models

Tatsuya Seiki[1], Woosub Roh[2], Masaki Satoh[2]

1: Japan Agency for Marine-Earth Science and Technology

Yokohama Institute for Earth Sciences

2: The University of Tokyo, Atmosphere and Ocean Research

Institute

Corresponding Author: Masaki Satoh (satoh@aori.u-tokyo.ac.jp)

This article is submitted for

"Earth's Climate and Weather: Dominant Variability and Disastrous Extremes"

AGU Geophysical Monograph Series

accepted July 11, 2021

Key words

- Global cloud resolving models
- Cloud microphysics
- Climate
- Climate change
- Weather forecasting
- Cloud radiative forcing
- Model evaluation
- Satellite simulators
- Satellite observations
- Ground observations

Abstract

Global cloud resolving models (GCRMs) are a new type of general circulation model that explicitly calculates the growth of cloud systems with fine spatial resolutions and more than 10 GCRMs have been developed at present. This chapter of the monograph reviews cloud microphysics schemes used in GCRMs with introductions to the recent progress and researches with GCRMs. Especially, research progress using a pioneer of GCRMs, Nonhydrostatic ICosahedral Atmospheric Model (NICAM), is focused. Since GCRMs deal with climatology and meteorology, it is a challenging issue to establish cloud microphysics schemes for GCRMs. A brief history of the development of cloud microphysics schemes and cloud-radiation coupling in NICAM is described. In addition, current progress in analytical techniques using satellite simulators is described. The combined use of multi-optical sensors enables us to constrain uncertain processes in cloud microphysics without artificial tuning. As a result, cloud microphysics schemes used in the NICAM naturally represent cloud systems, and hence, the radiative budget is well balanced with little optimization. Finally, a new satellite and a ground validation campaign are introduced for future work.

1. Introduction

This chapter of the monograph reviews cloud microphysics schemes used in global cloud resolving models (GCRMs) with introductions to the recent progress and researches with GCRMs. Section 1 briefly introduces the background and design of GCRMs. Cloud microphysics schemes in GCRMs are reviewed in Section 2 and model evaluation using optical sensors are reviewed in Section 3. Especially, research progress using a pioneer of GCRMs, Nonhydrostatic ICosahedral Atmospheric Model (NICAM), is focused. Finally, Section 4 summarizes this chapter. Acronyms of numerical models, satellites, and optical instruments are described in Table 1.

1.1 Global cloud resolving models

Climatology and meteorology have separated spatiotemporal scales and hence have been individually investigated in separate research communities (see Figure 1). However, ongoing climate change increases social risks such as record breaking intense precipitation, intense tropical cyclones, and extensive flood damage. Recent extreme events have been intensively analyzed around the world and have been edited as a special issue for "Explaining Extreme Events from a Climate Perspective" for the Bulletin of the American Meteorological Society every year starting in 2011 (e.g., Herring et al., 2019). To meet social demands, the World Climate Research Programme (WCRP) has promoted research on "weather and climate extremes" as one of the current grand challenges (https://www.wcrp-climate.org/grand-challenges/grand-challenges-overview). The two research communities have started to work together to tackle this issue across spatiotemporal scales.

For the next decade, the WCRP has newly proposed lighthouse activities (https://www.wcrp-climate.org/wcrp-ip-la), in which a "digital twin of Earth" is to be utilized for modeling earth systems more realistically (e.g. Bauer et al., 2021). Recent advances in parallel computing have

enabled us to achieve global atmospheric simulations with finer horizontal resolution (e.g., Wedi, 2014; Satoh et al., 2017; Schär et al., 2020). Thus, motivation and research infrastructure are now prepared for global cloud resolving simulations that fill the scale gap between climate research and weather forecasting.

In the UK, for example, the UPSCALE (UK on PRACE: weather-resolving Simulations of Climate for globAL Environmental risk) project was organized for global weather prediction using a general circulation model (GCM) with a horizontal resolution of up to 25 km (Mizielinski et al., 2014). In Europe, multi-high-resolution GCMs have been used for predicting regional climate as the PRocess-based climate sIMulation: AdVances in high-resolution modelling and European climate Risk Assessment (PRIMAVERA) project (https://www.primavera-h2020.eu/). In the Pan-Pacific region, the International laboratory for High-resolution Earth System Prediction (iHESP) project has started to examine intense cyclones for decadal prediction by using a 25-km atmosphere and 10-km ocean-coupled GCM (Zhang et al., 2020; Chang et al., 2020). Finally, the High Resolution Model Intercomparison Project (HighResMIP) was coordinated as a part of the Coupled Model Intercomparison Project Phase 6 (CMIP6) for examining the capability of capturing mesoscale phenomena using GCMs only by increasing the horizontal resolution up to 25 km (Haarsma et al., 2016; Roberts et al., 2018). However, in HighResMIP, most participants are conventional GCMs, which do not predict precipitating hydrometeors (e.g., rain, snow, graupel, and hail) [cloud microphysics in CMIP6 models are described in the ES-DOC Explorer (https://explore.es-doc.org/)] and rely on parameterizations for representing convective clouds, although some GCMs have recently incorporated explicit calculations for rain and snow [ARPEGE-Climat (Roehrig et al., 2020), CAM (Morrison and Gettelman, 2008; Song et al., 2012; Gettelman and Morrison, 2015), ECHAM/ICON-A (Posselt and Lohmann, 2008; Sant et al., 2015),

IFS (Forbes et al., 2011), MIROC (Michibata et al., 2019), and UM-Global Atmosphere (Boutle et al., 2014; Walters et al., 2019)]. Explicit (grid-scale) representations of convective clouds are necessary for seamlessly simulating the interaction between a mesoscale convective system and its environmental state at finer resolutions (e.g., Miyakawa et al., 2012; Takasuka et al. 2015). Climate models without convective parameterizations can successfully better represent some aspects of climate states than those with convective parameterizations by increasing horizontal resolution even if the climate models cannot fully resolve convective clouds (e.g., Senf et al., 2020; Stevens et al., 2020; Vergara-Temprado et al., 2020; Wedi et al., 2020).

In the era of global simulations with horizontal resolutions of a few kilometers, nonhydrostatic dynamical cores (e.g., Saito et al., 2007) are required for resolving convection in an environmental state (e.g., Kato and Saito, 1995; Weisman et al., 1997; Yang et al., 2017). In addition, cloud microphysics for precipitating hydrometeors should be explicitly calculated as is done in mesoscale models. Global atmospheric models that explicitly calculate the growth of cloud systems are a new type of GCM and are now called global cloud resolving models (Satoh et al., 2019). In particular, explicit representation of smaller clouds is a great advantage of GCRMs compared to conventional GCMs even if the cloud microphysics in GCMs become sophisticated (details are described in Section 3.2). Global cloud resolving models are now practically available for various research fields in many countries thanks to prevailing massive parallel computers and advanced network environments. For example, Nakano et al. (2017) demonstrated that forecasts of tropical cyclones generally improve by using three GCRMs with the horizontal resolution of less than 10 km. In contrast to operational global numerical weather prediction models (e.g., Kalnay et al., 1990; Zhang et al., 2019), GCRMs are not restricted by operating time and hence can be used for challenging issues in terms of spatiotemporal resolution and complexity of physics.

Currently, the first international intercomparison project for GCRMs, the initiative DYnamics of the Atmospheric general circulation Modeled On Non-hydrostatic Domains (DYAMOND), has been organized (Stevens et al., 2019) and GCRMs are becoming established (See Figure 2). Table 2 summarizes the GCRMs that have been developed at present. Note that multimodel framework (MMF) is another approach to modeling convective cloud systems in GCMs (e.g., Tao et al., 2009).

1.2. A baseline for spatial resolutions

Cloud microphysics schemes for GCRMs are designed to work with horizontal resolutions from 1 to 15 km based on 15 years of experience with global high-resolution simulations using the NICAM. Similarly, a common cloud microphysics scheme is used in a unified system for weather-to-seasonal prediction developed in the United States of America that uses a horizontal resolution of 13 km for medium-range weather prediction and a horizontal resolution of 3 km for global cloud resolving simulations [The geophysical fluid dynamics laboratory (GFDL) System for High-resolution prediction on Earth-to-Local Domains (SHiELD), Harris et al., 2020]. In addition, IFS has been well evaluated with a horizontal resolution of 9 km, and its results are comparable to IFS with a horizontal resolution of 1.4 km in many aspects (Wedi et al., 2020). Thus, IFS with a horizontal resolution of 9 km works for research purpose in terms of practical use, although Wedi et al. (2020) emphasized the advantages of using a 1 km resolution for resolving deep convection by IFS.

As a pioneer of GCRMs, the NICAM was developed in the early 2000s (Tomita et al., 2001; Satoh, 2002; Satoh, 2003; Tomita and Satoh, 2004) and has been improved over the past twenty years (Satoh et al., 2008a; Satoh et al., 2014; Kodama et al., 2021). NICAM developers first conducted cloud resolving simulations with horizontal resolutions of up to 3.5 km on an Aqua-

Planet (Tomita et al., 2005) and then achieved cloud resolving simulations with realistic land-ocean distributions (Miura et al., 2007a; 2007b). Miyamoto et al. (2013) finally attained the world's first global simulations with a subkilometer horizontal resolution (Figure 3) on the K computer with 20,480 nodes (163,840 cores).

Global statistics of convective cores from subkilometer simulations have shown that the number of convective cores does not converge, even at a 870 m resolution (Miyamoto et al., 2013; Kajikawa et al., 2016). Sueki et al. (2019) further investigated the resolved size of convective cores over the tropics and found similar results at a horizontal resolution of 50 m. In general, convective cores were found to become resolved at a horizontal resolution of 1/6 of their sizes (Miyamoto et al., 2013; Miyamoto et al., 2015; Kajikawa et al., 2016) and to become fully resolved at horizontal resolutions of 1/40 to 1/20 of their sizes (Sueki et al., 2019).

On the other hand, it has been found that individual convective cores are not necessarily resolved for capturing large-scale convective systems that last longer than the daily scale (cf. Figure 1) or some aspects of climate states as mentioned above. For example, in practice, a NICAM with a horizontal resolution of 14 km is widely used for Madden-Julian oscillation (MJO), tropical cyclones, and extratropical cyclones. A NICAM with a horizontal resolution of 14 km successfully shows the top-performing skill score of the MJO prediction (Miyakawa et al., 2014). Similarly, a NICAM with a horizontal resolution of 14 km successfully reproduces tropical cyclones (e.g., Oouchi et al., 2009; Taniguchi et al., 2010; Yanase et al., 2010; Nakano et al., 2015), as was done using a NICAM with finer horizontal resolutions (e.g., Fudeyasu et al., 2008; Yamada et al., 2016; Nakano et al., 2017). In particular, the eyewall structure has been clearly captured for intense tropical cyclones (Yamada et al., 2010; Yamada and Satoh, 2013; Yamada et al., 2017), although

158 the detailed wind structure of tropical cyclones was not sufficiently resolved even at a horizontal
159 resolution of 7 km (Miyamoto et al., 2014 and see also Figure 3).

160 We conclude that a horizontal resolution of 14 km, which roughly captures meso-beta-scale
161 (20 - 200 km) cloud systems according to Sueki et al. (2019), is a baseline for global cloud (system)
162 resolving simulations without cumulus parameterizations provided by the NICAM. In terms of the
163 response of clouds to global warming, the response of clouds smaller than 40 to 100 km is found
164 to be very different from the response of larger clouds (Noda et al., 2014; Noda et al., 2016). In
165 terms of the radiative budget, the global mean values almost converged at a horizontal resolution
166 of 3.5 km and did not significantly differ at horizontal resolutions equal to or finer than 14 km
167 (Kajikawa et al., 2016), whereas global simulations with horizontal resolutions of 28 km or 56 km
168 suffer from nonnegligible radiation biases (Seiki et al., 2015b; Kodama et al., 2021). The radiative
169 budget (cloud amount) is found to be affected by the numerical settings of physical processes
170 rather than horizontal resolution (Seiki et al., 2014; 2015a; Roh et al., 2017; Kodama et al., 2021),
171 as was shown in other GCMs (e.g., Meehl et al., 2019). Therefore, we efficiently optimize a cloud
172 microphysics scheme at a horizontal resolution of 14 km in a strategic way and then fine-tune
173 cloud microphysics at finer objective horizontal resolutions because of their high computational
174 cost.

175

176

177 **1.3. How to evaluate cloud microphysics**

178 Explicit coupling between radiation and cloud microphysics enables us to evaluate cloud
179 microphysics through cloud radiative forcing (e.g., Hashino et al., 2016). Moreover, the use of a
180 consistent assumption between the radiative transfer model and cloud microphysics represents
181 cloud radiative forcing depending on the particle shape and growth stage of cloud systems (Seiki

et al., 2014; 2015a; Thompson et al., 2016; Matsui et al., 2018). In addition, the coupling reduces the freedom of tunable model parameters. This substantially reduces efforts for model optimization and hence provides model developers an insight into the improvements in model performance (e.g., Kodama et al., 2021).

Satellite simulators push forward the idea of cloud-radiation coupling for the purpose of model evaluation, data assimilation, and observing system simulation experiments (e.g., Masunaga et al., 2010). Satellite simulators compile forward radiative transfer models that use model results as an atmospheric environment to match remote sensing (Figure 4). Thanks to satellite simulators, various types of cloud systems and their dominant cloud microphysics can be evaluated from various aspects by using multisensor analyses. Model evaluations using satellite simulators are reviewed in Section 3 in greater detail.

1.4. Benefits to optimizing Cloud Radiative Forcing

Cloud radiative forcing (CRF) is considered the most important parameter to optimize in the performance of cloud microphysics in GCRMs, whereas initialization and reproducibility of specific events are important for mesoscale models. Climate states are realized in the semiequilibrium condition of the energy balance; it is difficult to understand the causal relationship in the balanced state (e.g., Stevens and Feingold, 2009; Morrison et al., 2012). Therefore, one may design a cloud microphysics scheme that represents correct physical mechanisms with few tuning parameters and then optimize the CRF. Uncertainties in CRF significantly affect climate projection through various pathways of cloud feedback (e.g., Meehl et al., 2020; Sherwood et al., 2020). In terms of practical use for long-term simulations, CRF should be optimized because climate drift is inevitable because of energy imbalance (e.g., Stockdale, 1997).

One can strategically evaluate cloud microphysics schemes by using in situ observations or remote sensing whose objective is a specific type of cloud (details are described in Section 2). Cloud radiative forcing differs by cloud type (e.g., Hartmann et al., 1992): distributions of cloud types are climatologically determined by region and season (Rossow and Schiffer, 1999). In general, longwave CRF is dominated by high clouds; shortwave CRF is dominated by high thick clouds and low clouds; both longwave and shortwave CRF are effective over the intertropical convergence zone. In particular, cirrus generally has a strong long CRF even with a small optical thickness (Liou, 1986; Ackermann et al., 1988; Fu and Liou, 1993; Jensen et al., 1994) and extensively covers the upper troposphere (e.g., Liou, 1986; Rossow and Schiffer, 1999; Sassen et al., 2008; Haladay and Stephens, 2009; Hagihara et al., 2010) and hence has a strong influence on a broad range of atmospheric layers. In addition, low-level clouds are commonly biased as "too few and too bright" among GCMs (Nam et al., 2012) and have been a major source of uncertainties in climate sensitivity (e.g., Bony and Dufresne, 2005; Zhang et al., 2013; Andrews et al., 2015). In particular, a negative bias in low-level clouds strongly increases the downward shortwave radiative flux to the sea surface and consequently affects atmospheric circulation through ocean feedback (e.g., Kang et al., 2009; Trenbirth and Fasullo, 2010; Kay et al., 2016; Hyder et al., 2018). On the other hand, in the Arctic region, supercooled liquid water in low-level clouds strongly contributes to the longwave CRF to enhance sea ice (land surface ice) melting (e.g., Curry et al., 1993; Shupe et al., 2004; Francis et al., 2005; Bennartz et al., 2013; Kapsh et al., 2013; 2016). Recently, these strong impacts of CRF from various cloud types on climate states have been used for making a scale to measure the reliability of climate projections as "emergent constraints on future climate change" (e.g., Hall et al., 2019). Current progress in understanding climate sensitivity and cloud feedback is comprehensively reviewed in Sherwood et al. (2020).

Improvements in cloud radiative forcing evidently have positive feedback to improvements in model performances through cloud radiation interactions (e.g., Tao et al., 1996). For instance, satellite observations indicate that cirrus clouds generally support invigoration of convective clouds over the tropics through longwave CRF (Masunaga and Bony, 2018; Masunaga and Mapes, 2020). More specifically, the longwave component of the CRF has strong impacts on the structure and track of tropical cyclones (Fovell et al., 2010; Bu et al., 2014; 2017) and the onset of MJO (Takasuka et al., 2018). Thus, a cloud microphysics scheme, which is evaluated in terms of CRF, is expected to also work for case studies (e.g., Arakane et al., 2014; Sato et al., 2015; Yamada et al., 2016), regional weather prediction (e.g., Miyoshi et al., 2016; Nasuno et al., 2017; Harris et al., 2020), and regional climate research (e.g., Adachi et al., 2017; 2019; Adachi and Tomita, 2020).

1.5. Global and regional simulations

The hybrid use of a GCRM for global and regional simulations accelerates the evaluation of cloud microphysics using in situ measurements (see Figure 5 and details are described in Section 2). The use of in situ measurements [e.g., the Atmospheric Radiation Measurement (ARM)] will greatly contribute to improvements in GCRMs, as was done for GCMs (e.g., Randall et al., 2016). However, it is not efficient to perform global high-resolution simulations for comparison to in situ observations. Therefore, the NICAM employs two types of regional settings that are easily switched with a namelist in the running configuration. One is a stretched grid system on a global domain [so-called stretched NICAM (Tomita, 2008a; Uchida et al., 2016; Shibuya et al. 2016), see Figure 5b]. The other picks up one diamond panel of the icosahedron and uses the panel as the regional domain [so-called diamond NICAM (Uchida et al., 2017), see Figure 5c]. Both grid systems share icosahedral grid data, numerical operators, and physical packages with the original global settings. In addition, the single-column model has also been prepared (Seiki and Roh, 2020).

252 This kind of regional setting is also used in other GCRMs [ICON (Zängl et al., 2014; Stevens et
253 al., 2020), FV3 (Harris et al., 2019; 2020); MPAS (Skamarock, 2012; 2018); and UM (Davies et
254 al., 2005)].

255 In addition, portable usage of cloud microphysics among GCRMs, mesoscale models, and
256 LES models will complement the evaluation of cloud microphysics and will develop the
257 application of cloud microphysics. Cloud microphysics schemes in the NICAM are shared with
258 SCALE (Nishizawa et al., 2015; Sato et al., 2015), which works as a mesoscale model and a large
259 eddy simulation model. SCALE is highly optimized for massive parallel supercomputers with
260 codesign by researchers in computational science and computer science (https://scale.riken.jp/)
261 and hence can be used for ultrafine atmospheric simulations with a grid resolution of finer than 10
262 m (Sato et al., 2018) and for experimental applications such as prediction of the electric field by
263 solving the Poisson equation (Sato et al., 2019). In addition, one can examine the performance of
264 the cloud microphysics schemes in the NICAM in comparison to more complex schemes such as
265 a spectral bin cloud microphysics scheme or a Lagrangian particle model by using SCALE (e.g.,
266 Sato et al., 2015; 2018). This common usage of cloud microphysics is also found between ICON
267 and COSMO and between MPAS and WRF. In addition, one can use common packages for cloud
268 modeling to obtain widely used cloud microphysics schemes [e.g., Kinematic Driver (Shipway
269 and Hill, 2012); and libcloudph++ (Arabas et al., 2015; Jaruga and Pawlowska, 2018)].
270

271 **2. Cloud microphysics in the NICAM**

272 A brief history of the development of cloud microphysics schemes and related processes is
273 described in this section. The NICAM has various options for bulk cloud microphysics schemes
274 that assume particle size distribution (PSD) as specific analytic functions. Single-moment bulk

cloud microphysics schemes (SMBs) predict the total mass concentration, and double-moment bulk cloud microphysics schemes (DMBs) predict the total number concentration in addition to the total mass concentration to represent the time evolution of PSDs of hydrometeors. Spectral bin cloud microphysics schemes have not yet worked for global simulations with the NICAM because of the difficulty of tuning with their expensive computational cost. Single-moment bulk cloud microphysics schemes are widely used for GCRMs because of their simplicity and cheaper computational cost. Table 3 summarizes the cloud microphysics schemes used in the DYAMOND GCRMs. Most cloud microphysics in the DYAMOND GCRMs have not yet been comprehensively evaluated for global simulations and some GCRMs have individually started to analyze elemental variables such as surface precipitation (e.g., Arnold et al., 2020; Dueben et al., 2020; Hohenegger et al. 2020). Therefore, performances of cloud microphysics in GCRMs other than NICAM have not yet been sufficiently documented. Hereafter we focus on cloud microphysics in NICAM.

Thermodynamics in cloud microphysics schemes are modified to match the NICAM. In particular, the total air density and the moist internal energy are exactly conserved in common procedures such as diagnosis of the saturated vapor pressure (see Satoh 2003 and Satoh et al., 2008a, for details). Gravitational sedimentation is commonly solved using a semi-Lagrangian scheme, which is conservative and positive definite (Xiao et al. 2003).

2.1. Single-moment bulk cloud microphysics scheme with five water categories

The NICAM team began realistical global cloud resolving simulations with a SMB with five water categories proposed by Grabowski (1998) (hereafter G98). This scheme predicts the specific water content of vapor, cloud water and rain (*qv*, *qc*, and *qr*, respectively) and diagnoses the

299 specific water content of cloud ice and snow (*qi* and *qs*, respectively) by using temperature. The
300 concept of G98 is to represent different latent heat between the ice phase and liquid phase (e.g.,
301 latent heat of vaporization Lv = 2.50e6 J kg^{-1} and latent heat of sublimation Ls = 2.83e6 J kg^{-1} at
302 atmospheric temperature Ta = 273 K) and different terminal velocities between rain and snow
303 (typically 3 to 7 m s^{-1} for rain and at most 1 m s^{-1} for snow in G98), although G98 cannot deal with
304 melting and freezing due to the diagnosis. The diagnosis of ice categories is also used in other
305 SMBs for weather prediction (e.g., Lopez, 2002; Khairoutdinov and Randall, 2003). As G98 is
306 simple, there are only four tunable processes: auto-conversion and accretion of cloud water, auto-
307 conversion and accretion of cloud ice, terminal velocity of rain, and terminal velocity of snow.
308 Therefore, radiative fluxes of G98 were optimized by modifying the terminal velocity of snow (Iga
309 et al., 2007) with the assumed effective radii of cloud ice and snow as 40 μm.
310 These five category types of cloud microphysics do not separate dense ice (graupel and hail)
311 and light ice (snow) and hence do not capture differences in dominant growth processes between
312 convective precipitation systems (riming and accretion) and stratiform precipitation systems
313 (aggregation). In addition, the diagnosis of cloud ice and snow results in the absence of the melting
314 layer (freezing layer). These characteristics are apparently observed in the vertical structure of
315 radar echo by reference to satellite observations (Satoh et al., 2008b; Masunaga et al., 2008).
316 Nevertheless, G98 sufficiently worked to capture deep convective systems over the tropics, such
317 as tropical cyclones (e.g., Fudeyasu et al., 2008; Oouchi et al., 2009; Taniguchi et al., 2010; Yanase
318 et al., 2010) and MJO (e.g., Miura et al., 2007; Nasuno et al., 2009; Taniguchi et al., 2010;
319 Miyakawa et al., 2012).
320

2.2. Single-moment bulk cloud microphysics scheme with six water categories

The NICAM contains a SMB with six water categories referred to as NSW6 (NICAM single-moment bulk cloud microphysics with six water categories). This scheme predicts the specific water content of vapor, cloud water, rain, cloud ice, snow, and graupel (*qv*, *qc*, *qr*, *qi*, *qs*, and *qg*, respectively). Tomita (2008b) simplified a six-category type based on Lin et al. (1983) and Rutledge and Hobbs (1984) by omitting hail production and replacing the interaction between cloud water and cloud ice with a saturation adjustment to reduce the computational cost. These simplifications allow NSW6 to be similar to G98 except for microphysical processes involving graupel. Kodama et al. (2012) optimized the longwave CRF by modifying the timescale of the auto-conversion of cloud ice to snow. The 2012 version of the NICAM (NICAM.12), which was generally used for published works from 2012 to 2019 [e.g., an atmospheric model intercomparison project (AMIP) type experiment (Kodama et al., 2015)], was established based on this version of NSW6. The reproducibility and forecasting skills for tropical cyclones, MJO, and boreal-summer intra-seasonal oscillation improved by using NSW6 (e.g., Miyakawa et al., 2014; Miyakawa and Kikuchi, 2018; Nakano et al., 2015; 2017; Nakano and Kikuchi, 2019; Kikuchi et al., 2017).

Major revision of microphysical processes involving rain, snow, and graupel in NSW6 was accomplished by Roh and Satoh (2014) using the stretched NICAM by reference to TRMM satellite observations. The objectives of the revisions were to capture the vertical structure of convective systems over the tropics and to separately capture different types of cloud systems. Specifically, a rescaled bimodal shape of snow particle size distribution and variable bulk snow density were assumed following Field et al. (2005) and Thompson et al. (2008); excessive graupel was suppressed by switching off accretion of snow and cloud ice by graupel following Lang et al. (2007) and by changing the intercept parameter of the graupel particle size distribution following

345 Gilmore et al. (2004); and a variable formulation of the intercept parameter of the rain particle size
346 distribution was incorporated to represent stratiform rain systems following Zhang et al. (2008).
347 In addition, the saturation adjustment for cloud ice was replaced with vapor deposition and
348 sublimation to solve well-known issues (e.g., Gettelman et al., 2010). These modifications
349 significantly increased cloud ice and snow globally, and decreased graupel in the mid-latitudes.
350 As a result, vertical profiles of ice water content from this version of NSW6 more closely
351 approximated the satellite observations compared with those from NSW6 in NICAM.12 (Figure
352 6a-6c).

353 Finally, the cloud radiative forcing was successfully improved by explicitly coupling cloud
354 microphysics and radiative transfer using the coupling procedure provided by Seiki et al. (2014)
355 [Kodama et al., (2021); details are described in Section 2.4]. The 2016 version of the NICAM
356 (NICAM.16), which has been used for published works after 2020 [e.g., production for
357 HighResMIP (Kodama et al., 2021)], was established based on this version of NSW6.

358 The next version of NSW6 is now under development. Global simulations with NSW6 were
359 found to suffer from the underestimation bias in low-level mixed-phase clouds in the midlatitudes
360 to polar regions (Kodama et al., 2015; Hashino et al., 2016; Roh et al., 2020). Recently, Seiki and
361 Roh (2020) improved the bias by replacing rain-production terms with the auto-conversion and
362 accretion parameterizations by Khairoutdinov and Kogan (2000), an ice nucleation term with
363 heterogeneous ice nucleation by Phillips et al. (2007), and suppressing vapor deposition and riming
364 with reasonable thresholds. These modifications successfully prolonged the lifetime of mixed-
365 phase low-level clouds by sustaining supercooled liquid water. A similar approach was used to
366 improve low-level mixed-phase clouds by Furtado and Field (2017) with UM and Engdahl et al.

(2020) with AROME. The improvements were made using a single-column model, and hence, the new settings are now tested for long-term global simulations.

2.3. Double-moment bulk cloud microphysics scheme with six water categories

The NICAM contains a DMB with six water categories referred to as NDW6 (NICAM double-moment bulk cloud microphysics with six water categories). This scheme predicts the specific water content of vapor, cloud water, rain, cloud ice, snow, and graupel (*qv*, *qc*, *qr*, *qi*, *qs*, and *qg*, respectively) and the number concentration of each hydrometeor category (*nc*, *nr*, *ni*, *ns*, and *ng*, respectively). Seiki and Nakajima (2014) developed NDW6 based on Seifert and Beheng (2001; 2006) and Seifert (2008) (hereafter SB) with minor modifications (e.g., saturation adjustment of cloud water is replaced with condensation/evaporation). The SB scheme was evaluated in terms of surface precipitation but not for CRF (e.g., Seifert et al., 2006). As a result, large biases in outgoing longwave radiation at the top of the atmosphere (OLR) were found in global simulations with NDW6 (Figure 7a). This version of NDW6 is referred to as NDW6-SN14.

Seiki et al. (2014) elaborated ice modeling of NDW6 to improve the OLR biases originating from cirrus clouds: the heterogeneous ice nucleation scheme was replaced with the scheme based on Phillips et al. (2007), who referred to experimental data from field campaign observations by Demott et al. (2003); nonsphericity was incorporated into ice cloud microphysics assuming power-law relationships between the projected area and the particle mass and between the maximum dimension and the particle mass based on Mitchell (1996); and nonsphericity was incorporated into CRF based on Fu (1996) and Fu et al. (1998) (details are described in Section 2.4). These improvements were examined using a stretched NICAM by reference to in situ sonde observations. These modifications significantly improved the OLR biases in global simulations (Figure 7b). This version of NDW6 is referred to as NDW6-S14.

391 Seiki et al. (2015b) incorporated homogeneous ice nucleation into NDW6 based on Ren and
392 McKenzie (2005) and Kärcher et al. (2006) to alleviate the underestimation bias in *ni* found by
393 Seiki et al. (2014). In addition, the lower limit of the sticking efficiency was incorporated into ice
394 aggregation because of a lack of experimental evidence at atmospheric temperatures colder than
395 253 K (Pruppacher and Klett, 1997). Uncertainties in the sticking efficiency were also discussed
396 in Li et al. (2010). The impacts of the former change on OLR, which caused a significant decrease
397 in OLR, were cancelled by the latter change, and thus, OLR did not significantly change in this
398 latest version of NDW6 (Figure 7c). This version of NDW6 is referred to as NDW6-S15 and is
399 implemented in NICAM.16. Ice water content from NDW6-S15 (NDW6 in NICAM.16) is a little
400 bit underestimated, especially just above the freezing level (Figure 6a, 6d). Ice cloud microphysics
401 in winter snowfall systems, in which interaction between cloud ice and snow dominated, are well
402 represented by NDW6-S15 (Kondo et al., 2021), and hence, hydrometeor interactions between
403 rain and graupel might be problematic. The bias in IWC and higher OLR over the tropics indicate
404 that NDW6-S15 underestimate high-density ice (graupel) originated by convection.
405 The remaining biases in OLR were found to originate from the spatial resolution of the
406 NICAM (Seiki et al., 2015b). Specifically, negative biases in OLR over the subtropical regions
407 originated from insufficient vertical resolution for capturing thin cirrus layers, and positive biases
408 in OLR over the tropics originated from insufficient horizontal resolution for capturing convective
409 organization. Both biases clearly diminish as vertical layers increase (Figure 7d) and horizontal
410 resolution increases (Figure 7e). Therefore, NDW6 does not need extensive tuning in terms of
411 CRF. In the current status of the NICAM (e.g., Stevens et al., 2019), 78 vertical layers with a layer
412 thickness of approximately 400 m in the free troposphere are used as a standard setting based on
413 Seiki et al. (2015b).

414

415 **2.4. Coupling procedure between cloud microphysics and radiative transfer**

416 Cloud radiative forcing significantly differs based on the assumption of single-scattering
417 properties (SSPs). For example, the nonsphericity of ice particles had an impact on outgoing solar
418 radiation at the top of the atmosphere (OSR) by more than 100 W m^{-2} in a cirrus case [Seiki et al.
419 (2014) and see Figure 8], and an invalid assumption of effective radii as a globally fixed value,
420 which was used in NICAM.12, caused nonnegligible biases in both OLR and OSR [10 to 20 W m^{-2}
421 from the tropics to mid-latitudes (Seiki et al., 2015a; Kodama et al., 2021), and see Figure 9].
422 These biases in CRF are comparable to or greater than the biases originating from uncertainties in
423 cloud microphysics. Thus, it is better to optimize cloud microphysics after explicitly coupling
424 cloud microphysics and radiative transfer. Importance of cloud-radiation coupling for numerical
425 weather prediction was discussed also using other models (e.g., Thompson et al., 2016; Matsui et
426 al., 2018).

427 Cloud microphysics is coupled with radiative transfer through SSPs of hydrometeors. The
428 single-scattering properties strongly depend on the ratio of particle size to wavelength (e.g.,
429 Hansen and Travis, 1974); hence, SSPs are generally prepared as a look-up table of effective radii
430 at each wavelength band in radiative transfer models. In the NICAM, radiative transfer is
431 calculated with a broadband model mstrnX (Sekiguchi and Nakajima, 2008), which requires the
432 extinction coefficient per unit volume of hydrometeor particles, scattering coefficients per unit
433 volume of the hydrometeor particles, and moments of the phase function (asymmetry factor and
434 truncation factor) used for the delta two-stream approximation (Nakajima et al., 2000). Thus, input
435 data to the coupling procedure are the volume of the hydrometeors and effective radii derived from
436 cloud microphysics.

In the latest version of the NICAM [NICAM.16 (Kodama et al., 2021)], nonsphericity is newly assumed for the SSP of ice hydrometeors because nonsphericity has been found to have a strong impact on both shortwave radiation (e.g., Pollack and Cuzzi, 1980; Takano and Liou, 1989, 1995; Stephens et al., 1990; Macke, 1993; Yang and Liou, 1995; MacFarquhar et al., 1999; Fu, 2007) and longwave radiation (e.g., Ackerman and Stephens, 1987; Mitchell and Arnott, 1994; Mitchell et al., 1996). A nonspherical database provided by Fu (1996) and Fu et al. (1998) was compiled for the wavelength bands used in mstrnX, and then the SSP look-up table was prepared in the range of effective radii from 1 μm to 1 mm (Seiki et al., 2014). One may choose another nonspherical SSP database that has options to choose specific shapes, such as Yang et al. (2013) [e.g., NU-WRF (Matsui et al., 2018); MIROC (Tatabe et al., 2019)]. Seiki et al. (2014) found that the dependence of the asymmetry factor on the effective radii, which vary by particle shape, is key to determining the cloud albedo of cirrus, as shown in Figure 8.

The definition of the effective radii of nonspherical ice particles is another issue for nonspherical modeling because the "effective" size is not obvious for irregular shapes in contrast to a sphere. Therefore, the concept of "effective distance", which is defined by the ratio of the volume to the projected area, was proposed by Mitchell and Arnott (1994). The concept was confirmed by Fu (1998) by reference to light scattering calculated using the finite difference time domain method. Following equations (3.11) in Fu (1996) or (2.5) in Fu et al. (1998), the effective radii of ice hydrometeors *re* are defined as follows:

$re_j \equiv \frac{3}{4\rho_{\mathrm{ice}}} \frac{\rho_a q_j}{\int_0^\infty A_j(x) f_j(x) dx}$, $(j = i, s, g)$	(1)

where ρ_a is the air density, ρ_{ice} = 916.7 kg m^{-3} is the ice density, A is the projected area, x is the particle mass, and f is the particle mass distribution.

458 Equation (1) is analytically integrated with the power-law relationship between A and x for
459 each hydrometeor category ($A = \gamma x^{\sigma}$). In NDW6, particle models compiled by Mitchell (1996) are
460 used: hexagonal columns for cloud ice, assemblages of planar polycrystals in cirrus clouds for
461 snow, and lump graupel for graupel (Seiki et al., 2014). In NSW6, sponge-like spherical ice is
462 assumed for cloud ice and graupel, and two-dimensional fractal shapes (e.g., $A \propto D^2$ and $x \propto D^2$)
463 are assumed for snow (Roh and Satoh, 2014; Kodama et al., 2021). Thus, the effective radii of
464 snow are assumed to be constant (res = 125 μm). The cloud radiative forcing of NSW6
465 significantly decreases with this assumption for the effective radii (see NSW6, NSW6-Mie, and
466 NSW6-Mie-ReFIX in Figure 9).
467
468 **2.5. Impact of precipitating hydrometeors on the radiation budget**
469 The impacts of precipitating hydrometeors on CRF can be examined by means of the new
470 look-up table. CMIP3 and CMIP5 GCMs commonly have large biases in CRF over the ITCZ
471 region (Li et al., 2013). Past studies suggested that these biases originated from the lack of CRF
472 by precipitating hydrometeors in conventional GCMs (e.g., Waliser et al., 2011; Li et al., 2014;
473 2016). Chen et al. (2018) analyzed the role of precipitating hydrometeors by using an off-line
474 radiation model with NICAM results and found that the layering structure of snow underlying
475 cloud ice had impacts on OLR over the tropics and storm-track regions up to 2 W m^{-2} Similarly,
476 snow has strong impacts on OSR up to 3 W m^{-2} in the summer hemisphere.
477 The degree of the possible biases related to precipitating hydrometeors could differ by model
478 (Matsui et al., 2018; Michibata et al. 2019), but it is evident that the systematic effect of
479 precipitating hydrometeors on radiation is nonnegligible in terms of climate projection. Recently,
480 precipitating hydrometeors have been found to have important indirect effects on aerosol-cloud

interactions (so-called buffering effects) with MIROC (Michibata and Suzuki, 2020; Michibata et al., 2020).

2.6. Differences between SMBs and DMBs

Representation of changing number concentrations is essential for representing realistic cloud growth. Figure 10 shows the typical cloud microphysical processes used in SMBs and DMBs. It is clearly seen that most processes change the number concentrations in addition to the mass concentration. SMBs generally deal with this issue by assuming PSD functions (qj and nj relationship) based on observations. Thus, the performance of SMBs relies on the diagnosis technique of PSDs.

The complexity and dependence of cloud microphysical processes inevitably differ between DMBs and SMBs regardless of the diagnosis technique of PSDs. For example, condensation increases only qr, but evaporation decreases both qr and nr (e.g., Morrison and Grabowski, 2008). In addition, larger liquid droplets are more likely to freeze [heterogeneous and homogeneous freezing of supercooled liquid water (e.g., Bigg 1953; Fukuta and Schaller, 1982; Khvorostyanov and Curry, 2009)], but smaller ice crystals more easily melt away. This kind of asymmetry between a pair of growth and decay processes (see the pairs of arrows in Figure 10) induces hysteresis, and hence, cannot be represented by SMBs. As a result, SMBs necessarily simplify these processes and modify the balance among the hydrometeor interactions. The ratio of the tendency between the mass concentration and the number concentration $[(\partial qj/\partial t)/(\partial nj/\partial t)]$ differs by process, and hence, these inconsistencies in the tendency result in bias in the mean particle mass $\bar{x}j = (\rho_a qj/nj)$ or mean particle diameter $\overline{Dj}$ when using SMBs.

Biases in the mean particle mass (diameter) feedback to the performance of cloud microphysics schemes through the dependence of particle-growth equations (e.g., Igel et al., 2015;

505 Seiki et al., 2015; Seiki and Roh, 2020). The dependences of cloud-related processes on bulk cloud
506 microphysical parameters are summarized in Table 4. For example, in collisional processes, the
507 collisional cross section is proportional to the square of the particle diameter. In addition, in
508 evaporation (sublimation) and condensation (deposition), vapor flux onto the particles is
509 proportional to their surface area (square of the particle diameter). Moreover, terminal velocity,
510 which is contained in many microphysical processes, is mostly determined by the particle diameter
511 (Bohm, 1989; 1992; Mitchell, 1996). In terms of CRF, the extinction efficiency is represented as
512 a function of the size parameter, and the extinction cross-section is proportional to the square of
513 the particle radii as mentioned in Section 2.4. Thus, strong feedbacks of xj (or Dj) to cloud
514 microphysics and CRF imply that cloud microphysics can potentially be evaluated by monitoring
515 xj (or Dj) from observations. Specifically, optical sensors, which are sensitive to various moments
516 of particle radii, are powerful tools to define the growth mode of clouds. Evaluation of cloud
517 microphysics in the NICAM using satellite observations is described in Section 3.
518

519 **3. Model evaluation using optical sensors**

520 **3.1 Sensitivity of optical sensors**

521 There are two kinds of optical sensors to observe clouds and precipitating hydrometeors.
522 Passive sensors can observe the radiance from clouds and precipitation and have more spatial
523 coverage than active sensors. Active sensors have a transmitter and a receiver and can detect the
524 vertical profiles of clouds and precipitation, but they have a smaller swath than passive sensors.
525 Thus, the combined use of the two types of optical sensors can complementarily reveal the nature
526 of cloud systems in detail. In addition, satellite sensors have different characteristics depending on

527 the wavelength of the sensor. The major satellites used for model evaluation are summarized in
528 Table 5.

529 Visible (Vis) channels can observe optically thick clouds, and the observations are limited
530 during daytime. Visible channels have been widely used for estimating warm-cloud optical
531 properties [e.g., optical thickness and effective radius (Nakajima and King, 1990)]. The infrared
532 (IR) channels, especially from 10 to 13 μm wavelength, are sensitive to cloud-top temperature and
533 can detect even very thin cirrus clouds. Infrared channels have also been utilized for detecting
534 cloud optical properties (e.g., Iwabuchi et al., 2016; 2018). The combined use of VIS and IR
535 channels has been used for categorizing cloud systems using the cloud optical thickness and cloud-
536 top temperature [e.g., the International Satellite Cloud Climatology Project cloud category
537 proposed by Rossow and Schiffer (1999)].

538 Passive microwaves are sensitive to precipitating hydrometeors. Low frequency microwaves
539 (<20 GHz) are used to capture the emissions from the path-integrated water content of rain over
540 the ocean. On the other hand, high-frequency microwaves (>80 GHz) are used for capturing
541 scattering signals of large ice particles such as snow and graupel over land and ocean. These
542 various frequencies of microwave observations enable us to obtain integrated column information
543 about precipitating hydrometeors, particularly in deep convective systems.

544 Active microwave observations referred to as radar are now available at 94 GHz/3.2 mm (so-
545 called cloud radar) and at 13.6 GHz/2.2 cm and 35.5 GHz/8.5 mm (so-called precipitation radar).
546 In addition, lidar with wavelengths of 532 and 1064 nm is available. In general, the backscattering
547 coefficient rapidly decreases at size parameters ($2\pi r/\lambda$) smaller than 1 according to Mie theory,
548 and hence, the detectable particle size differs by the frequency/wavelength. In addition, too strong
549 backscattering results in strong attenuation of return signals. The Cloud Profilin Radar (CPR) on

CloudSat can clearly detect vertical profiles of nonprecipitating and light-precipitating clouds and slightly detect intense precipitating clouds due to attenuation (Stephens et al. 2008). CALIOP on CALIPSO can detect optical thin cirrus and the thermodynamic phase of clouds using the depolarization ratio (Winker et al., 2009). The precipitation radar on TRMM and GPM core satellites can detect the vertical profiles of precipitating clouds but cannot detect nonprecipitating clouds (Hou et al., 2014). Even when using GPM satellite observations, it is difficult to accurately capture extreme precipitation systems such as hail storms due to strong attenuation, multiple scattering, and spatial inhomogeneity (e.g., Mroz et al., 2018). Thus, the combined use of lidar, cloud radar, and precipitation radar enables us to integrate an understanding of cloud organization from shallow clouds to deep convective clouds.

Consistency in the assumption of cloud microphysics between a model and a satellite retrieval algorithm is an important issue. For example, so-called Z-R and k-Z relationships, which implicitly assume a PSD, are used in the retrieval of precipitation flux using PR (Iguchi et al., 2009). However, the assumptions are generally not used in cloud microphysics schemes. In contrast, some cloud microphysics schemes (e.g., Milbrandt and Yau, 2005; Seifert, 2008) have more degrees of freedom to represent PSDs than these retrieval algorithms. In addition, satellite products inherently suffer from contamination: a product consists of a major portion of an objective physical parameter and a minor portion of other physical parameters. For example, in the past, it was difficult to separate cloud water paths from liquid water paths in the retrieval of microwaves (Elsaesser et al., 2017). It is still difficult to retrieve snowfall over sea ice or land ice using microwaves. Thus, we need to understand the characteristics of optical sensors in comparing model results to satellite observations.

572 Satellite simulators solve the issue by directly comparing emulated satellite signals from
573 model results to level 1 satellite data (see Figure 4). This comparison method enables us to share
574 microphysical assumptions between a model and satellite simulators. On the other hand, it is
575 difficult to interpret radiance-based comparisons to find biases in cloud microphysics schemes.
576 Current progress in analytical techniques using satellite simulators is described in the following
577 sections. Note that the accuracy of emulated satellite signals depends on the forward radiative
578 transfer calculation method used in a satellite simulator and hence it needs to be examined,
579 especially in data assimilation (e.g., Okamoto, 2017; Okamoto et al., 2019). At present, various
580 satellite simulators (optical sensor simulators) have been developed [e.g., COSP (Bodas-Salcedo
581 et al., 2011; Swales et al., 2018), CRTM (Chen et al., 2008; Ding et al., 2011), ECSIM (Voor et
582 al., 2007; Reverdy et al., 2015), Joint-Simulator (Hashino et al., 2013; Satoh et al., 2016),
583 POLARRIS (Matsui et al., 2019), RTTOV (Saunders et al., 2018), SDSU (Masunaga et al. 2010),
584 and Goddard-SDSU (Matsui et al., 2013; 2014)].
585

586 **3.2 Evaluation of the size distribution of cloud systems**
587 The horizontal resolution of GCRMs that is comparable to satellite observations is a milestone
588 for the evaluation of cloud representation. For example, infrared channels on a geostationary
589 satellite MTSAT, which were frequently used for capturing cirrus clouds (e.g., Inoue, 1987; Mapes
590 and Houze, 1993), had a footprint size of approximately 4 km. Thus, cloud size can be newly
591 evaluated by the advent of GCRMs, whereas cloud fraction is derived from macrophysics in
592 conventional GCMs (e.g., Watanabe et al., 2009; Park et al., 2014). Horizontal inhomogeneity in
593 cloud distribution develops as the cloud regime changes (Kawai and Teixeira, 2010; 2012), and
594 hence, explicit representation of cloud systems is the unique approach of GCRMs. One can use

595 GCRMs' cloud distribution to evaluate sub-grid inhomogeneity assumed in conventional GCMs
596 (e.g., Watanabe et al., 2009; Hotta et al., 2020).

597 The split-window technique, which uses brightness temperature of 11 μm and 12 μm, is
598 generally applied to classify high clouds (e.g., Inoue, 1987; Liou, 2002). In addition, OLR or IWP
599 can also be applicable to classifying relatively thick high clouds over the subtropics to tropics (e.g.,
600 Inoue and Ackerman, 2002; Inoue et al., 2006; 2008; 2010). The size distribution of high clouds
601 derived from MTSAT was well reproduced by the NICAM with a horizontal resolution of 3.5 km
602 (Inoue et al., 2008), and smaller clouds are likely to be underestimated as the horizontal resolution
603 decreases to 7 km or 14 km (Inoue et al., 2008; Noda et al., 2014). Recently, CloudSat and
604 CALPSO satellite observations have also been available for estimating cloud sizes with the
605 categorization of cloud types (e.g., Seiki et al., 2019)

606 A new issue arises from the NICAM simulations: formation processes of smaller high clouds,
607 which are not well represented in GCRMs or conventional GCMs. Even small clouds make a large
608 contribution to the total CRF over the tropics due to their large population. This is true for the
609 response of high clouds to global warming (Noda et al., 2014; 2016). Simulated results from the
610 NICAM indicated that the response of high clouds with cloud radii smaller than 50 km to global
611 warming significantly differs from the response with cloud radii larger than 100 km (Noda et al.,
612 2014; 2016). In particular, the robustness of the fixed anvil temperature (FAT) hypothesis
613 (Hartmann and Larson, 2002; Zelinka and Hartmann, 2010) is found to depend on cloud sizes
614 (Noda et al., 2016). Figure 11 shows an example of the different responses of high clouds to global
615 warming by cloud size. The OLR change under global warming attributes to a change in
616 emissivity, a change in cloud top temperature, and a change in clear sky radiation. A reduction in
617 the emissivity is found to be dominant in the response of smaller thin cirrus whereas an increase

618 in the cloud top temperature is dominant in the response of larger clouds as was established by
619 conventional GCMs with the FAT hypothesis. Moreover, Noda et al. (2019) argued that convective
620 self-aggregation (e.g., Wing et al., 2017) does not sufficiently work to reduce CRF over the tropics
621 from cloud-size analysis using global high-resolution simulations. Note that cirrus clouds contain
622 very small-scale structures, such as uncinus and streak structures (e.g., Heymsfield, 1975), which
623 can be captured by using large eddy simulation models (e.g., Sölch and Kärcher, 2011). Thus, the
624 response of smaller cirrus formations to climate change is an underdeveloped issue.
625

626 **3.3 Evaluation of vertical structure of cloud systems**

627 The vertical structures of precipitating cloud systems from NICAM simulations have been
628 evaluated using active sensors: TRMM-PR, CloudSat-CPR, and CALIPSO-CALIOP. In
629 particular, TRMM-PR has a footprint of 5 km, and hence, rain microphysics is directly evaluated
630 without assuming subgrid variability. TRMM-PR enables us to evaluate the difference in the
631 vertical structure of precipitation flux between convective cloud systems and stratiform cloud
632 systems (Takayabu, 2002; Satoh et al., 2008b). Here, the physical parameter "precipitation flux"
633 has inconsistency in the terminal velocities of precipitating hydrometeors between the NICAM
634 and TRMM algorithms. Therefore, the evaluation of models using retrieved products is not an
635 apple-to-apple comparison. After Satoh et al. (2008b), we generally used satellite simulators to
636 evaluate the vertical structures of cloud systems.

637 The contoured frequency by altitude diagram (CFAD), which illustrates the probability
638 density function of the radar reflectivity at each vertical level, is frequently used for evaluating the
639 vertical structure of cloud systems (e.g., Marchand et al., 2009; Matsui et al., 2016). Atmospheric
640 temperature is also used as the vertical axis of the CFAD to capture differences in the freezing

level and the tropopause level by latitude. The shape of the CFAD is sensitive to cloud microphysics or assumptions of particle shapes (e.g., Masunaga et al., 2008; Satoh et al., 2010; Hashino et al., 2013). In addition to the CFAD, a cloud-top beta-temperature radar-conditioned diagram was also proposed by Hashino et al. (2013) to analyze the relationship between ice water content and ice effective radii. The sensitivity of cloud microphysics to the CFAD was clearly observed within only 7 days from NICAM simulations (e.g., Satoh et al., 2010; Roh and Satoh, 2014; Roh et al., 2017). Therefore, we did not require longer simulations (e.g., seasonal to annual simulations) to evaluate cloud microphysics schemes using satellite observations.

Nakajima et al. (2010) proposed a contoured frequency by using the optical depth diagram (CFODD), which uses the cloud optical depth from the cloud top (COD) as the vertical axis, by using Aqua and CloudSat satellite observations. This alternative diagram successfully captures the transition of the droplet growth mode from condensational growth to collisional growth by means of the characteristics that the COD is directly related to the liquid water path and effective radius (Suzuki et al., 2010; 2011). Auto-conversion and accretion in warm clouds have been globally evaluated by using the CFODD (Suzuki et al., 2013; 2015). Kuba et al. (2015) analyzed the detectable cloud microphysics in the CFODD using a spectral bin cloud microphysics scheme.

In terms of the evaluation of cloud microphysics schemes in the NICAM, Kuba et al. (2020) found that the CFODD is sensitive to the shape parameters assumed in the PSD function from the comparison between NDW6 and a spectral bin cloud microphysics scheme. The contoured frequency by optical depth diagram can also be utilized for the evaluation of vertical structures of cirrus clouds by combining CloudSat and CALIPSO satellite observations (Seiki et al., 2015b). One can easily analyze the CFODD for cirrus clouds by using the EarthCARE Research Product

663 Monitor (https://www.eorc.jaxa.jp/EARTHCARE/research_product/ecare_monitor.html)
664 provided by the Japan Aerospace Exploration Agency.
665

666 **3.4 Evaluation of cloud organization**

667 Masunaga et al. (2005) proposed an analytical method to categorize cloud systems using
668 cloud-top temperature and radar echo top height from TRMM satellite observations (see Figure
669 12a). The categorized cloud systems were found to be closely related to large scale circulation
670 (Masunaga and Kumerrow, 2006). Thus, the cloud-top and rain-top diagrams can be used for the
671 evaluation of cloud organization in GCRMs (e.g., Masunaga et al., 2008). Recently, Roh and Satoh
672 (2018) proposed a method to extend the observable coverage by using the polarization-corrected
673 brightness temperature at 89 GHz (PCT89) instead of radar echo to detect the rain-top height.

674 Matsui et al. (2009) further established a method to systematically evaluate the cloud
675 microphysics scheme [Triple-Sensor Three-Step Evaluation Framework (T3EF)]: comparisons of
676 1) the cloud-top and rain-top diagram from IR radiance and radar echo, 2) CFAD from radar echo,
677 and 3) cumulative probability distribution of PCT85 from a high-frequency microwave imager.
678 T3EF clearly revealed problematic processes in a cloud microphysics scheme (Li et al., 2010).
679 NSW6 was successfully revised by using T3EF (Roh and Satoh, 2014; Roh et al., 2017, and see
680 Figure 12).
681

682 **3.5 Evaluation of hydrometeor classes**

683 Global observations of the depolarization ratio from CALIOP enable us to discriminate the
684 thermodynamic phase of hydrometeors and the shape of ice particles (Hu et al., 2009; 2010;
685 Yoshida et al., 2010; Saito et al., 2016). Recently, the GCM-Oriented CALIPSO Cloud Product

686 (CALIPSO-GOCCP) was released for easy comparison between models and CALIPSO satellite
687 observations (Chepfer et al., 2010). One can evaluate the frequency of occurrence of liquid and ice
688 clouds to evaluate the freezing process in cloud microphysics schemes using GOCCP (Cesana and
689 Chepfer, 2012). The GCM results were more consistently evaluated by satellite observations with
690 the aid of a satellite simulator (Cesana and Chepfer, 2013; Cesana et al., 2015). Note that
691 hydrometeor classification using CALIOP is limited to nonprecipitating particles near the cloud
692 top due to the limitation of attenuation (e.g., Hagihara et al., 2014).

693 Roh et al. (2020) developed a single parameterization to diagnose the depolarization ratio
694 from the backscattering coefficient and then evaluated NSW6 and NDW6 using the hydrometeor
695 discrimination method proposed by Yoshida et al. (2010) (see Figure 13). NSW6 underestimated
696 mixed-phase low-level clouds over the Southern Ocean due to poor representation of supercooled
697 liquid water, whereas NDW6 reproduced mixed-phase low-level clouds well. The bias in NSW6
698 was successfully alleviated by Seiki and Roh (2020), as described in Section 2.2.

699 Large particles can be evaluated using cloud radar and precipitation radar. Kikuchi et al.
700 (2017) proposed a hydrometeor classification method using only CPR radar echo and atmospheric
701 temperature based on the CloudsSat-CALIPSO combined dataset. Recently, hydrometeor
702 classification using GPM-DPR satellite observations has been developed. Snow, rain, and mixed-
703 phase clouds are categorized by using Ku-band radar echo and the dual-frequency ratio (Liao and
704 Meneghini, 2011; 2016; Liao et al., 2020). In addition, the hail detection method was newly
705 proposed by Seiki (2021). Future work should evaluate the microphysics of precipitating
706 hydrometeors using CPR and DPR.
707

3.6 Challenging issues in satellite simulators

A challenging new satellite project is now underway: The Earth Clouds, Aerosol and Radiation Explorer (EarthCARE, Illingworth et al. 2015) satellite, which is a joint mission by the European Space and Japanese Aerospace Exploration Agencies. The EarthCARE satellite has multiple passive and active sensors (Figure 14): Cloud Profiling Radar (CPR), ATmospheric LIDar (ATLID), Multi Spectral Imager (MSI), and Broad Band Radiometer (BBR). The CPR on EarthCARE has a Doppler capability to provide information on the terminal velocity of rain and ice and convective motions. Multiple sensors have synergy to understand the interaction between clouds and aerosols and to provide new insights into cloud microphysics related to vertical motion for evaluating GCRMs. It is confirmed that the EarthCARE satellite will be launched in 2023.

Global cloud resolving models can be used for the observing system simulation experiments (OSSE) to evaluate retrieval algorithms for optical sensors at the planning stage of new satellite projects. A NICAM with a Joint-Simulator was used to create the EarthCARE-like radiances to estimate the accuracy of the retrieved Doppler velocity. In particular, OSSE using the NICAM were helpful to investigate the noise of Doppler velocity of CPR depending on the instrument setting (pulse repetition frequency) before the launch (Hagihara et al., 2021).

There are ongoing challenging issues in the development of satellite simulators. First, satellite simulators will be utilized to estimate a range of uncertainties from the observations, as was done by Hagihara et al. (2021). Second, the sensitivity of the nonspherical assumption to cloud representation is also a challenging issue. Several satellite simulators consider the nonspherical shapes of ice from a database using the discrete dipole approximation (DDA) and T-matrix (e.g., Hashino et al. 2013; Matsui et al. 2019). In addition, the application of depolarization provides insight into nonspherical modeling (Matsui et al., 2019). Finally, the 3D radiation of clouds is a long-standing issue (e.g., Benner and Evans 2001; Okata et al. 2017), whereas radiative transfer is

732 generally calculated in the vertical dimension. Three-dimensional scattering from cloud sides will
733 be nonnegligible when the horizontal resolution of GCRMs increases to finer than 1 km (global
734 LES). Monte Carlo simulations or other 3D techniques will be introduced into satellite simulators.
735

736 **3.7 Ground validation for satellites and models**

737 The ULTra-sIte for Measuring Atmosphere of Tokyo metropolitan Environment
738 (ULTIMATE) project has started to validate satellite observations and cloud microphysics
739 schemes in numerical models by using intensive ground observation data in Japan. The
740 ULTIMATE project obtained several active sensors to detect the vertical distributions of clouds
741 and precipitation. For example, polarimetric Doppler radars were set to derive information about
742 the size distributions, hydrometeor types, and terminal velocity of hydrometeors. In addition,
743 several weather radars (c-band polarimetric radars, x-band phased array polarimetric radar, and w-
744 band cloud radar) work in cooperation around the Tokyo metropolitan area (Figure 15). Wind
745 profiler network and data acquisition system (WINDAS, Ishihara et al. 2006) data are also
746 available to observe the vertical profiles of wind. To utilize these ground radar networks, the
747 POLArimetric Radar Retrieval and Instrument Simulator (POLARRIS, Matsui et al. 2019) is
748 newly introduced into the Joint-Simulator. The synergy of intensive ground, remote-sensing
749 observations and satellite data will contribute to the understanding of microphysical processes and
750 improvements of microphysics in GCRMs.

751 **4. Summary**

752 This chapter reviewed the cloud microphysics in GCRMs and the way to improve cloud
753 microphysics. From the twenty-year history of NICAM development, we recognized that the
754 combined use of multi-optical sensors enables us to constrain uncertain processes in cloud

755 microphysics without artificial tuning. As a result, cloud microphysics schemes used in the
756 NICAM naturally represent cloud systems, and hence, the radiative budget is well balanced with
757 little optimization. On the other hand, some cloud systems have not yet been evaluated because of
758 the diversity of cloud systems in Earth and the limited sensitivity of spaceborne optical sensors.
759 The evaluation method using satellite simulators is underdeveloped, and new satellites will be
760 continuously planned and launched. In addition, intensive ground observation systems and satellite
761 observations are complementary to each other. Thus, a new frontier for cloud microphysics
762 development is still spreading toward the future.
763
764 **Acknowledgments**
765 The CloudSat and CERES satellite products were obtained from the NASA Langley Research
766 Center Atmospheric Science Data Center. Authors were supported by the Integrated Research
767 Program for Advancing Climate Models (TOUGOU) Grant (JPMXD0717935457) and "Program
768 for Promoting Researches on the Supercomputer Fugaku" (Large Ensemble Atmospheric and
769 Environmental Prediction for Disaster Prevention and Mitigation) (JPMXP1020351142), which
770 are promoted by the Ministry of Education, Culture, Sports, Science and Technology (MEXT),
771 Japan. Authors were supported by the EarthCARE Program, Earth Observation Research Center
772 of JAXA, and Program for Promoting Technological Development of Transportation (Ministry of
773 Land, Infrastructure, Transport and Tourism of Japan), and Japan Society for the Promotion of
774 Science, Grant-in-Aid for Scientific Research B (20H01967) for Ultra Site for Measuring
775 Atmosphere of Tokyo Metropolitan Environment and Collaboration Studies with High-Resolution
776 Atmospheric Models (ULTIMATE).
777
778

779 **Reference**

780 Ackerman, S. A., & Stephens, G. L. (1987). The Absorption of Solar Radiation by Cloud Droplets:
781 An Application of Anomalous Diffraction Theory. *Journal of the Atmospheric Sciences*,
782 *44*(12), 1574–1588. https://doi.org/10.1175/1520-
783 0469(1987)044<1574:TAOSRB>2.0.CO;2

784 Ackerman, T. P., Liou, K.-N., Valero, F. P. J., & Pfister, L. (1988). Heating Rates in Tropical
785 Anvils. *Journal of the Atmospheric Sciences*, *45*(10), 1606–1623.
786 https://doi.org/10.1175/1520-0469(1988)045<1606:HRITA>2.0.CO;2

787 Adachi, S. A., Nishizawa, S., Yoshida, R., Yamaura, T., Ando, K., Yashiro, H., Kajikawa, Y., &
788 Tomita, H. (2017). Contributions of changes in climatology and perturbation and the resulting
789 nonlinearity to regional climate change. *Nature Communications*, *8*(1), 2224.
790 https://doi.org/10.1038/s41467-017-02360-z

791 Adachi, S. A., Nishizawa, S., Ando, K., Yamaura, T., Yoshida, R., Yashiro, H., Kajikawa, Y., &
792 Tomita, H. (2019). An evaluation method for uncertainties in regional climate projections.
793 *Atmospheric Science Letters*, *20*(1), e877. https://doi.org/10.1002/asl.877

794 Adachi, S. A., & Tomita, H. (2020). Methodology of the Constraint Condition in Dynamical
795 Downscaling for Regional Climate Evaluation: A Review. Journal of Geophysical Research:
796 Atmospheres, 125(11), e2019JD032166. https://doi.org/10.1029/2019JD032166

797 Andrews, T., Gregory, J. M., & Webb, M. J. (2015). The Dependence of Radiative Forcing and
798 Feedback on Evolving Patterns of Surface Temperature Change in Climate Models. *Journal*
799 *of Climate*, *28*(4), 1630–1648. https://doi.org/10.1175/JCLI-D-14-00545.1

800 Arabas, S., Jaruga, A., Pawlowska, H., & Grabowski, W. W. (2015). libcloudph++ 1.0: A single-
801 moment bulk, double-moment bulk, and particle-based warm-rain microphysics library in

C++. *Geoscientific Model Development*, *8*(6), 1677–1707. https://doi.org/10.5194/gmd-8-1677-2015

Arakane, S., Satoh, M., & Yanase, W. (2014). Excitation of Deep Convection to the North of Tropical Storm Bebinca (2006). *Journal of the Meteorological Society of Japan. Ser. II*, *92*(2), 141–161. https://doi.org/10.2151/jmsj.2014-201

Arnold, N. P., Putman, W. M., & Freitas, S. R. (2020). Impact of Resolution and Parameterized Convection on the Diurnal Cycle of Precipitation in a Global Nonhydrostatic Model. *Journal of the Meteorological Society of Japan. Ser. II*, *98*(6), 1279–1304. https://doi.org/10.2151/jmsj.2020-066

Austin, R. T., & Stephens, G. L. (2001). Retrieval of stratus cloud microphysical parameters using millimeter-wave radar and visible optical depth in preparation for CloudSat: 1. Algorithm formulation. *Journal of Geophysical Research: Atmospheres*, *106*(D22), 28233–28242. https://doi.org/10.1029/2000JD000293

Austin, R. T., Heymsfield, A. J., & Stephens, G. L. (2009). Retrieval of ice cloud microphysical parameters using the CloudSat millimeter-wave radar and temperature. *Journal of Geophysical Research: Atmospheres*, *114*(D8). https://doi.org/10.1029/2008JD010049

Bauer, P., Stevens, B., & Hazeleger, W. (2021). A digital twin of Earth for the green transition. *Nature Climate Change*, *11*(2), 80–83. https://doi.org/10.1038/s41558-021-00986-y

Bennartz, R., Shupe, M. D., Turner, D. D., Walden, V. P., Steffen, K., Cox, C. J., Kulie, M. S., Miller, N. B., & Pettersen, C. (2013). July 2012 Greenland melt extent enhanced by low-level liquid clouds. *Nature*, *496*(7443), 83–86. https://doi.org/10.1038/nature12002

823 Benner, T. C., & Evans, K. F. (2001). Three-dimensional solar radiative transfer in small tropical
824 cumulus fields derived from high-resolution imagery. *Journal of Geophysical Research:*
825 *Atmospheres*, *106*(D14), 14975–14984. https://doi.org/10.1029/2001JD900158
826 Bigg, E. K. (1953). The formation of atmospheric ice crystals by the freezing of droplets. *Quarterly*
827 *Journal of the Royal Meteorological Society*, *79*(342), 510–519.
828 https://doi.org/10.1002/qj.49707934207
829 Bodas-Salcedo, A., Webb, M. J., Bony, S., Chepfer, H., Dufresne, J.-L., Klein, S. A., Zhang, Y.,
830 Marchand, R., Haynes, J. M., Pincus, R., & John, V. O. (2011). COSP: Satellite simulation
831 software for model assessment. *Bulletin of the American Meteorological Society*, *92*(8),
832 1023–1043. https://doi.org/10.1175/2011BAMS2856.1
833 Böhm, H. P. (1989). A General Equation for the Terminal Fall Speed of Solid Hydrometeors.
834 *Journal of the Atmospheric Sciences*, *46*(15), 2419–2427. https://doi.org/10.1175/1520-
835 0469(1989)046<2419:AGEFTT>2.0.CO;2
836 Böhm, J. P. (1992). A general hydrodynamic theory for mixed-phase microphysics. Part I: Drag
837 and fall speed of hydrometeors. *Atmospheric Research*, *27*(4), 253–274.
838 https://doi.org/10.1016/0169-8095(92)90035-9
839 Bony, S., & Dufresne, J.-L. (2005). Marine boundary layer clouds at the heart of tropical cloud
840 feedback uncertainties in climate models. *Geophysical Research Letters*, *32*(20).
841 https://doi.org/10.1029/2005GL023851
842 Boutle, I. A., Eyre, J. E. J., & Lock, A. P. (2014). Seamless Stratocumulus Simulation across the
843 Turbulent Gray Zone. *Monthly Weather Review*, *142*(4), 1655–1668.
844 https://doi.org/10.1175/MWR-D-13-00229.1

Bu, Y. P., Fovell, R. G., & Corbosiero, K. L. (2014). Influence of Cloud–Radiative Forcing on Tropical Cyclone Structure. *Journal of the Atmospheric Sciences*, *71*(5), 1644–1662. https://doi.org/10.1175/JAS-D-13-0265.1

Bu, Y. P., Fovell, R. G., & Corbosiero, K. L. (2017). The Influences of Boundary Layer Mixing and Cloud-Radiative Forcing on Tropical Cyclone Size. *Journal of the Atmospheric Sciences*, *74*(4), 1273–1292. https://doi.org/10.1175/JAS-D-16-0231.1

Bubnová, R., Hello, G., Bénard, P., & Geleyn, J.-F. (1995). Integration of the Fully Elastic Equations Cast in the Hydrostatic Pressure Terrain-Following Coordinate in the Framework of the ARPEGE/Aladin NWP System. *Monthly Weather Review*, *123*(2), 515–535. https://doi.org/10.1175/1520-0493(1995)123<0515:IOTFEE>2.0.CO;2

Cesana, G., & Chepfer, H. (2012). How well do climate models simulate cloud vertical structure? A comparison between CALIPSO-GOCCP satellite observations and CMIP5 models. *Geophysical Research Letters*, *39*(20). https://doi.org/10.1029/2012GL053153

Cesana, Grégory, & Chepfer, H. (2013). Evaluation of the cloud thermodynamic phase in a climate model using CALIPSO-GOCCP. *Journal of Geophysical Research: Atmospheres*, *118*(14), 7922–7937. https://doi.org/10.1002/jgrd.50376

Cesana, G., Waliser, D. E., Jiang, X., & Li, J.-L. F. (2015). Multimodel evaluation of cloud phase transition using satellite and reanalysis data. *Journal of Geophysical Research: Atmospheres*, *120*(15), 7871–7892. https://doi.org/10.1002/2014JD022932

Chang, P., Zhang, S., Danabasoglu, G., Yeager, S. G., Fu, H., Wang, H., Castruccio, F. S., Chen, Y., Edwards, J., Fu, D., Jia, Y., Laurindo, L. C., Liu, X., Rosenbloom, N., Small, R. J., Xu, G., Zeng, Y., Zhang, Q., Bacmeister, J., … Wu, L. (2020). An Unprecedented Set of High-Resolution Earth System Simulations for Understanding Multiscale Interactions in Climate

Variability and Change. *Journal of Advances in Modeling Earth Systems*, *12*(12), e2020MS002298. https://doi.org/10.1029/2020MS002298

Chen, Y., Weng, F., Han, Y., & Liu, Q. (2008). Validation of the Community Radiative Transfer Model by using CloudSat data. *Journal of Geophysical Research: Atmospheres*, *113*(D8). https://doi.org/10.1029/2007JD009561

Chen, Y.-W., Seiki, T., Kodama, C., Satoh, M., & Noda, A. T. (2018). Impact of Precipitating Ice Hydrometeors on Longwave Radiative Effect Estimated by a Global Cloud-System Resolving Model. *Journal of Advances in Modeling Earth Systems*, *10*(2), 284–296. https://doi.org/10.1002/2017MS001180

Chepfer, H., Bony, S., Winker, D., Cesana, G., Dufresne, J. L., Minnis, P., Stubenrauch, C. J., & Zeng, S. (2010). The GCM-Oriented CALIPSO Cloud Product (CALIPSO-GOCCP). *Journal of Geophysical Research: Atmospheres*, *115*(D4). https://doi.org/10.1029/2009JD012251

Curry, J. A., Schramm, J. L., & Ebert, E. E. (1993). Impact of clouds on the surface radiation balance of the Arctic Ocean. *Meteorology and Atmospheric Physics*, *51*(3), 197–217. https://doi.org/10.1007/BF01030494

Davies, T., Cullen, M. J. P., Malcolm, A. J., Mawson, M. H., Staniforth, A., White, A. A., & Wood, N. (2005). A new dynamical core for the Met Office's global and regional modelling of the atmosphere. *Quarterly Journal of the Royal Meteorological Society*, *131*(608), 1759–1782. https://doi.org/10.1256/qj.04.101

DeMott, P. J., Cziczo, D. J., Prenni, A. J., Murphy, D. M., Kreidenweis, S. M., Thomson, D. S., Borys, R., & Rogers, D. C. (2003). Measurements of the concentration and composition of nuclei for cirrus formation. *Proceedings of the National Academy of Sciences*, *100*(25), 14655–14660. https://doi.org/10.1073/pnas.2532677100

Ding, S., Yang, P., Weng, F., Liu, Q., Han, Y., van Delst, P., Li, J., & Baum, B. (2011). Validation of the community radiative transfer model. *Journal of Quantitative Spectroscopy and Radiative Transfer*, *112*(6), 1050–1064. https://doi.org/10.1016/j.jqsrt.2010.11.009

Dueben, P. D., Wedi, N., Saarinen, S., & Zeman, C. (2020). Global Simulations of the Atmosphere at 1.45 km Grid-Spacing with the Integrated Forecasting System. *Journal of the Meteorological Society of Japan. Ser. II*, *98*(3), 551–572. https://doi.org/10.2151/jmsj.2020-016

Elsaesser, G. S., O'Dell, C. W., Lebsock, M. D., Bennartz, R., Greenwald, T. J., & Wentz, F. J. (2017). The Multisensor Advanced Climatology of Liquid Water Path (MAC-LWP). *Journal of Climate*, *30*(24), 10193–10210. https://doi.org/10.1175/JCLI-D-16-0902.1

Engdahl, B. J. K., Thompson, G., & Bengtsson, L. (2020). Improving the representation of supercooled liquid water in the HARMONIE-AROME weather forecast model. *Tellus A: Dynamic Meteorology and Oceanography*, *72*(1), 1–18. https://doi.org/10.1080/16000870.2019.1697603

Field, P. R., Hogan, R. J., Brown, P. R. A., Illingworth, A. J., Choularton, T. W., & Cotton, R. J. (2005). Parametrization of ice-particle size distributions for mid-latitude stratiform cloud. *Quarterly Journal of the Royal Meteorological Society*, *131*(609), 1997–2017. https://doi.org/10.1256/qj.04.134

Forbes, R., Tompkins, A. M., & Untch, A. (2011). *A new prognostic bulk microphysics scheme for the IFS*. ECMWF. https://doi.org/10.21957/bf6vjvxk

Fovell, R. G., Corbosiero, K. L., Seifert, A., & Liou, K.-N. (2010). Impact of cloud-radiative processes on hurricane track. *Geophysical Research Letters*, *37*(7). https://doi.org/10.1029/2010GL042691

914 Francis, J. A., Hunter, E., Key, J. R., & Wang, X. (2005). Clues to variability in Arctic minimum
915 sea ice extent. *Geophysical Research Letters*, *32*(21). https://doi.org/10.1029/2005GL024376
916 Fu, Q. (2007). A New Parameterization of an Asymmetry Factor of Cirrus Clouds for Climate
917 Models. *Journal of the Atmospheric Sciences*, *64*(11), 4140–4150.
918 https://doi.org/10.1175/2007JAS2289.1
919 Fu, Q., & Liou, K. N. (1993). Parameterization of the Radiative Properties of Cirrus Clouds.
920 *Journal of the Atmospheric Sciences*, *50*(13), 2008–2025. https://doi.org/10.1175/1520-
921 0469(1993)050<2008:POTRPO>2.0.CO;2
922 Fu, Q., Yang, P., & Sun, W. B. (1998). An Accurate Parameterization of the Infrared Radiative
923 Properties of Cirrus Clouds for Climate Models. *Journal of Climate*, *11*(9), 2223–2237.
924 https://doi.org/10.1175/1520-0442(1998)011<2223:AAPOTI>2.0.CO;2
925 Fudeyasu, H., Wang, Y., Satoh, M., Nasuno, T., Miura, H., & Yanase, W. (2008). Global cloud-
926 system-resolving model NICAM successfully simulated the lifecycles of two real tropical
927 cyclones. *Geophysical Research Letters*, *35*(22). https://doi.org/10.1029/2008GL036003
928 Fukuta, N., & Schaller, R. C. (1982). Ice Nucleation by Aerosol Particles. Theory of Condensation-
929 Freezing Nucleation. *Journal of the Atmospheric Sciences*, *39*(3), 648–655.
930 https://doi.org/10.1175/1520-0469(1982)039<0648:INBAPT>2.0.CO;2
931 Furtado, K., & Field, P. (2017). The Role of Ice Microphysics Parametrizations in Determining
932 the Prevalence of Supercooled Liquid Water in High-Resolution Simulations of a Southern
933 Ocean Midlatitude Cyclone. *Journal of the Atmospheric Sciences*, *74*(6), 2001–2021.
934 https://doi.org/10.1175/JAS-D-16-0165.1
935 Gettelman, A., Liu, X., Ghan, S. J., Morrison, H., Park, S., Conley, A. J., Klein, S. A., Boyle, J.,
936 Mitchell, D. L., & Li, J.-L. F. (2010). Global simulations of ice nucleation and ice

supersaturation with an improved cloud scheme in the Community Atmosphere Model. *Journal of Geophysical Research: Atmospheres*, *115*(D18). https://doi.org/10.1029/2009JD013797

Gettelman, A., & Morrison, H. (2015). Advanced Two-Moment Bulk Microphysics for Global Models. Part I: Off-Line Tests and Comparison with Other Schemes. *Journal of Climate*, *28*(3), 1268–1287. https://doi.org/10.1175/JCLI-D-14-00102.1

Gilmore, M. S., Straka, J. M., & Rasmussen, E. N. (2004). Precipitation Uncertainty Due to Variations in Precipitation Particle Parameters within a Simple Microphysics Scheme. *Monthly Weather Review*, *132*(11), 2610–2627. https://doi.org/10.1175/MWR2810.1

Grabowski, W. W. (1998). Toward Cloud Resolving Modeling of Large-Scale Tropical Circulations: A Simple Cloud Microphysics Parameterization. *Journal of the Atmospheric Sciences*, *55*(21), 3283–3298. https://doi.org/10.1175/1520-0469(1998)055<3283:TCRMOL>2.0.CO;2

Haarsma, R. J., Roberts, M. J., Vidale, P. L., Senior, C. A., Bellucci, A., Bao, Q., Chang, P., Corti, S., Fučkar, N. S., Guemas, V., von Hardenberg, J., Hazeleger, W., Kodama, C., Koenigk, T., Leung, L. R., Lu, J., Luo, J.-J., Mao, J., Mizielinski, M. S., … von Storch, J.-S. (2016). High Resolution Model Intercomparison Project (HighResMIP v1.0) for CMIP6. *Geoscientific Model Development*, *9*(11), 4185–4208. https://doi.org/10.5194/gmd-9-4185-2016

Hagihara, Yuichiro, Okamoto, H., & Yoshida, R. (2010). Development of a combined CloudSat-CALIPSO cloud mask to show global cloud distribution. *Journal of Geophysical Research: Atmospheres*, *115*(D4). https://doi.org/10.1029/2009JD012344

Hagihara, Yuichiro, Okamoto, H., & Luo, Z. J. (2014). Joint analysis of cloud top heights from CloudSat and CALIPSO: New insights into cloud top microphysics. *Journal of Geophysical Research: Atmospheres*, *119*(7), 4087–4106. https://doi.org/10.1002/2013JD020919

Hagihara, Y., Ohno, Y., Horie, H., Roh, W., Satoh, M., Kubota, T., & Oki, R. (2021). Assessments of Doppler Velocity Errors of EarthCARE Cloud Profiling Radar Using Global Cloud System Resolving Simulations: Effects of Doppler Broadening and Folding. *IEEE Transactions on Geoscience and Remote Sensing*, 1–9. https://doi.org/10.1109/TGRS.2021.3060828

Haladay, T., & Stephens, G. (2009). Characteristics of tropical thin cirrus clouds deduced from joint CloudSat and CALIPSO observations. *Journal of Geophysical Research: Atmospheres*, *114*(D8). https://doi.org/10.1029/2008JD010675

Hall, A., Cox, P., Huntingford, C., & Klein, S. (2019). Progressing emergent constraints on future climate change. *Nature Climate Change*, *9*(4), 269–278. https://doi.org/10.1038/s41558-019-0436-6

Hansen, J. E., & Travis, L. D. (1974). Light scattering in planetary atmospheres. *Space Science Reviews*, *16*(4), 527–610. https://doi.org/10.1007/BF00168069

Harris, L. M., Rees, S. L., Morin, M., Zhou, L., & Stern, W. F. (2019). Explicit Prediction of Continental Convection in a Skillful Variable-Resolution Global Model. *Journal of Advances in Modeling Earth Systems*, *11*(6), 1847–1869. https://doi.org/10.1029/2018MS001542

Harris, L., Zhou, L., Lin, S.-J., Chen, J.-H., Chen, X., Gao, K., Morin, M., Rees, S., Sun, Y., Tong, M., Xiang, B., Bender, M., Benson, R., Cheng, K.-Y., Clark, S., Elbert, O. D., Hazelton, A., Huff, J. J., Kaltenbaugh, A., … Stern, W. (2020). GFDL SHiELD: A Unified System for Weather-to-Seasonal Prediction. *Journal of Advances in Modeling Earth Systems*, *12*(10), e2020MS002223. https://doi.org/10.1029/2020MS002223

Hartmann, D. L., Ockert-Bell, M. E., & Michelsen, M. L. (1992). The Effect of Cloud Type on Earth's Energy Balance: Global Analysis. *Journal of Climate*, *5*(11), 1281–1304. https://doi.org/10.1175/1520-0442(1992)005<1281:TEOCTO>2.0.CO;2

Hartmann, D. L., & Larson, K. (2002). An important constraint on tropical cloud—Climate feedback. *Geophysical Research Letters*, *29*(20), 12-1-12–14. https://doi.org/10.1029/2002GL015835

Hashino, T., Satoh, M., Hagihara, Y., Kubota, T., Matsui, T., Nasuno, T., & Okamoto, H. (2013). Evaluating cloud microphysics from NICAM against CloudSat and CALIPSO. *Journal of Geophysical Research: Atmospheres*, *118*(13), 7273–7292. https://doi.org/10.1002/jgrd.50564

Hashino, T., Satoh, M., Hagihara, Y., Kato, S., Kubota, T., Matsui, T., Nasuno, T., Okamoto, H., & Sekiguchi, M. (2016). Evaluating Arctic cloud radiative effects simulated by NICAM with A-train. *Journal of Geophysical Research: Atmospheres*, *121*(12), 7041–7063. https://doi.org/10.1002/2016JD024775

Herring, S. C., Christidis, N., Hoell, A., Hoerling, M. P., & Stott, P. A. (2019). Explaining Extreme Events of 2017 from a Climate Perspective. *Bulletin of the American Meteorological Society*, *100*(1), S1–S117. https://doi.org/10.1175/BAMS-ExplainingExtremeEvents2017.1

Heymsfield, A. (1975). Cirrus Uncinus Generating Cells and the Evolution of Cirriform Clouds. Part II: The Structure and Circulations of the Cirrus Uncinus Generating Head. *Journal of the Atmospheric Sciences*, *32*(4), 809–819. https://doi.org/10.1175/1520-0469(1975)032<0809:CUGCAT>2.0.CO;2

Hohenegger, C., Kornblueh, L., Klocke, D., Becker, T., Cioni, G., Engels, J. F., Schulzweida, U., & Stevens, B. (2020). Climate Statistics in Global Simulations of the Atmosphere, from 80

to 2.5 km Grid Spacing. *Journal of the Meteorological Society of Japan. Ser. II*, *98*(1), 73–91. https://doi.org/10.2151/jmsj.2020-005

Hotta, H., Suzuki, K., Goto, D., & Lebsock, M. (2020). Climate Impact of Cloud Water Inhomogeneity through Microphysical Processes in a Global Climate Model. Journal of Climate, 33(12), 5195–5212. https://doi.org/10.1175/JCLI-D-19-0772.1

Hou, A. Y., Kakar, R. K., Neeck, S., Azarbarzin, A. A., Kummerow, C. D., Kojima, M., Oki, R., Nakamura, K., & Iguchi, T. (2014). The Global Precipitation Measurement Mission. *Bulletin of the American Meteorological Society*, *95*(5), 701–722. https://doi.org/10.1175/BAMS-D-13-00164.1

Hu, Y., Winker, D., Vaughan, M., Lin, B., Omar, A., Trepte, C., Flittner, D., Yang, P., Nasiri, S. L., Baum, B., Holz, R., Sun, W., Liu, Z., Wang, Z., Young, S., Stamnes, K., Huang, J., & Kuehn, R. (2009). CALIPSO/CALIOP Cloud Phase Discrimination Algorithm. *Journal of Atmospheric and Oceanic Technology*, *26*(11), 2293–2309. https://doi.org/10.1175/2009JTECHA1280.1

Hu, Y., Rodier, S., Xu, K., Sun, W., Huang, J., Lin, B., Zhai, P., & Josset, D. (2010). Occurrence, liquid water content, and fraction of supercooled water clouds from combined CALIOP/IIR/MODIS measurements. *Journal of Geophysical Research: Atmospheres*, *115*(D4). https://doi.org/10.1029/2009JD012384

Hyder, P., Edwards, J. M., Allan, R. P., Hewitt, H. T., Bracegirdle, T. J., Gregory, J. M., Wood, R. A., Meijers, A. J. S., Mulcahy, J., Field, P., Furtado, K., Bodas-Salcedo, A., Williams, K. D., Copsey, D., Josey, S. A., Liu, C., Roberts, C. D., Sanchez, C., Ridley, J., … Belcher, S. E. (2018). Critical Southern Ocean climate model biases traced to atmospheric model cloud errors. *Nature Communications*, *9*(1), 3625. https://doi.org/10.1038/s41467-018-05634-2

1027 Iga, S., Tomita, H., Tsushima, Y., & Satoh, M. (2007). Climatology of a nonhydrostatic global
1028 model with explicit cloud processes. *Geophysical Research Letters*, *34*(22).
1029 https://doi.org/10.1029/2007GL031048
1030 Igel, A. L., Igel, M. R., & Heever, S. C. van den. (2015). Make It a Double? Sobering Results from
1031 Simulations Using Single-Moment Microphysics Schemes. *Journal of the Atmospheric*
1032 *Sciences*, *72*(2), 910–925. https://doi.org/10.1175/JAS-D-14-0107.1
1033 Iguchi, T., Kozu, T., Kwiatkowski, J., Meneghini, R., Awaka, J., & Okamoto, K. (2009).
1034 Uncertainties in the Rain Profiling Algorithm for the TRMM Precipitation Radar. *Journal of*
1035 *the Meteorological Society of Japan. Ser. II*, *87A*, 1–30. https://doi.org/10.2151/jmsj.87A.1
1036 Illingworth, A. J., Barker, H. W., Beljaars, A., Ceccaldi, M., Chepfer, H., Clerbaux, N., Cole, J.,
1037 Delanoë, J., Domenech, C., Donovan, D. P., Fukuda, S., Hirakata, M., Hogan, R. J.,
1038 Huenerbein, A., Kollias, P., Kubota, T., Nakajima, T., Nakajima, T. Y., Nishizawa, T., …
1039 Zadelhoff, G.-J. van. (2015). The EarthCARE Satellite: The Next Step Forward in Global
1040 Measurements of Clouds, Aerosols, Precipitation, and Radiation. *Bulletin of the American*
1041 *Meteorological Society*, *96*(8), 1311–1332. https://doi.org/10.1175/BAMS-D-12-00227.1
1042 Inoue, Tomotsugu, Ueda, H., & Inoue, T. (2006). Cloud Properties over the Bay of Bengal Derived
1043 from NOAA-9 Split Window Data and the TRMM PR Product. *Sola*, *2*, 41–44.
1044 https://doi.org/10.2151/sola.2006-011
1045 Inoue, Toshiro. (1987). A cloud type classification with NOAA 7 split-window measurements.
1046 *Journal of Geophysical Research: Atmospheres*, *92*(D4), 3991–4000.
1047 https://doi.org/10.1029/JD092iD04p03991
1048 Inoue, Toshiro, & Ackerman, S. A. (2002). Radiative Effects of Various Cloud Types as Classified
1049 by the Split Window Technique over the Eastern Sub-tropical Pacific Derived from

1050 Collocated ERBE and AVHRR Data. *Journal of the Meteorological Society of Japan. Ser. II*,
1051 *80*(6), 1383–1394. https://doi.org/10.2151/jmsj.80.1383
1052 Inoue, Toshiro, Satoh, M., Miura, H., & Mapes, B. (2008). Characteristics of Cloud Size of Deep
1053 Convection Simulated by a Global Cloud Resolving Model over the Western Tropical Pacific.
1054 *Journal of the Meteorological Society of Japan. Ser. II*, *86A*, 1–15.
1055 https://doi.org/10.2151/jmsj.86A.1
1056 Inoue, Toshiro, Satoh, M., Hagihara, Y., Miura, H., & Schmetz, J. (2010). Comparison of high-
1057 level clouds represented in a global cloud system–resolving model with CALIPSO/CloudSat
1058 and geostationary satellite observations. *Journal of Geophysical Research: Atmospheres*,
1059 *115*(D4). https://doi.org/10.1029/2009JD012371
1060 Ishihara, M., Kato, Y., Abo, T., Kobayashi, K., & Izumikawa, Y. (2006). Characteristics and
1061 Performance of the Operational Wind Profiler Network of the Japan Meteorological Agency.
1062 *Journal of the Meteorological Society of Japan. Ser. II*, *84*(6), 1085–1096.
1063 https://doi.org/10.2151/jmsj.84.1085
1064 Iwabuchi, H., Saito, M., Tokoro, Y., Putri, N. S., & Sekiguchi, M. (2016). Retrieval of radiative
1065 and microphysical properties of clouds from multispectral infrared measurements. *Progress*
1066 *in Earth and Planetary Science*, *3*(1), 32. https://doi.org/10.1186/s40645-016-0108-3
1067 Iwabuchi, H., Putri, N. S., Saito, M., Tokoro, Y., Sekiguchi, M., Yang, P., & Baum, B. A. (2018).
1068 Cloud Property Retrieval from Multiband Infrared Measurements by Himawari-8. *Journal of*
1069 *the Meteorological Society of Japan. Ser. II*, *96B*, 27–42. https://doi.org/10.2151/jmsj.2018-
1070 001

1071 Jaruga, A., & Pawlowska, H. (2018). libcloudph++ 2.0: Aqueous-phase chemistry extension of the
1072 particle-based cloud microphysics scheme. *Geoscientific Model Development*, *11*(9), 3623–
1073 3645. https://doi.org/10.5194/gmd-11-3623-2018
1074 Jensen, E. J., Kinne, S., & Toon, O. B. (1994). Tropical cirrus cloud radiative forcing: Sensitivity
1075 studies. *Geophysical Research Letters*, *21*(18), 2023–2026.
1076 https://doi.org/10.1029/94GL01358
1077 Kajikawa, Y., Miyamoto, Y., Yoshida, R., Yamaura, T., Yashiro, H., & Tomita, H. (2016).
1078 Resolution dependence of deep convections in a global simulation from over 10-kilometer to
1079 sub-kilometer grid spacing. *Progress in Earth and Planetary Science*, *3*(1), 16.
1080 https://doi.org/10.1186/s40645-016-0094-5
1081 Kalnay, E., Kanamitsu, M., & Baker, W. E. (1990). Global Numerical Weather Prediction at the
1082 National Meteorological Center. *Bulletin of the American Meteorological Society*, *71*(10),
1083 1410–1428. https://doi.org/10.1175/1520-0477(1990)071<1410:GNWPAT>2.0.CO;2
1084 Kang, S. M., Frierson, D. M. W., & Held, I. M. (2009). The Tropical Response to Extratropical
1085 Thermal Forcing in an Idealized GCM: The Importance of Radiative Feedbacks and
1086 Convective Parameterization. *Journal of the Atmospheric Sciences*, *66*(9), 2812–2827.
1087 https://doi.org/10.1175/2009JAS2924.1
1088 Kapsch, M.-L., Graversen, R. G., & Tjernström, M. (2013). Springtime atmospheric energy
1089 transport and the control of Arctic summer sea-ice extent. *Nature Climate Change*, *3*(8), 744–
1090 748. https://doi.org/10.1038/nclimate1884
1091 Kapsch, M.-L., Graversen, R. G., Tjernström, M., & Bintanja, R. (2016). The Effect of
1092 Downwelling Longwave and Shortwave Radiation on Arctic Summer Sea Ice. *Journal of*
1093 *Climate*, *29*(3), 1143–1159. https://doi.org/10.1175/JCLI-D-15-0238.1

1094 Kärcher, B., Hendricks, J., & Lohmann, U. (2006). Physically based parameterization of cirrus
1095 cloud formation for use in global atmospheric models. *Journal of Geophysical Research:*
1096 *Atmospheres*, *111*(D1). https://doi.org/10.1029/2005JD006219
1097 Kato, T., & Saito, K. (1995). Hydrostatic and Non-Hydrostatic Simulations of Moist Convection.
1098 *Journal of the Meteorological Society of Japan. Ser. II*, *73*(1), 59–77.
1099 https://doi.org/10.2151/jmsj1965.73.1_59
1100 Kawai, H., & Teixeira, J. (2010). Probability Density Functions of Liquid Water Path and Cloud
1101 Amount of Marine Boundary Layer Clouds: Geographical and Seasonal Variations and
1102 Controlling Meteorological Factors. *Journal of Climate*, *23*(8), 2079–2092.
1103 https://doi.org/10.1175/2009JCLI3070.1
1104 Kawai, H., & Teixeira, J. (2012). Probability Density Functions of Liquid Water Path and Total
1105 Water Content of Marine Boundary Layer Clouds: Implications for Cloud Parameterization.
1106 *Journal of Climate*, *25*(6), 2162–2177. https://doi.org/10.1175/JCLI-D-11-00117.1
1107 Kay, J. E., Wall, C., Yettella, V., Medeiros, B., Hannay, C., Caldwell, P., & Bitz, C. (2016). Global
1108 Climate Impacts of Fixing the Southern Ocean Shortwave Radiation Bias in the Community
1109 Earth System Model (CESM). *Journal of Climate*, *29*(12), 4617–4636.
1110 https://doi.org/10.1175/JCLI-D-15-0358.1
1111 Khairoutdinov, M., & Kogan, Y. (2000). A New Cloud Physics Parameterization in a Large-Eddy
1112 Simulation Model of Marine Stratocumulus. *Monthly Weather Review*, *128*(1), 229–243.
1113 https://doi.org/10.1175/1520-0493(2000)128<0229:ANCPPI>2.0.CO;2
1114 Khairoutdinov, M. F., & Randall, D. A. (2003). Cloud Resolving Modeling of the ARM Summer
1115 1997 IOP: Model Formulation, Results, Uncertainties, and Sensitivities. *Journal of the*

Atmospheric Sciences, *60*(4), 607–625. https://doi.org/10.1175/1520-0469(2003)060<0607:CRMOTA>2.0.CO;2

Khvorostyanov, V. I., & Curry, J. A. (2009). Critical humidities of homogeneous and heterogeneous ice nucleation: Inferences from extended classical nucleation theory. *Journal of Geophysical Research: Atmospheres*, *114*(D4). https://doi.org/10.1029/2008JD011197

Kikuchi, K., Kodama, C., Nasuno, T., Nakano, M., Miura, H., Satoh, M., Noda, A. T., & Yamada, Y. (2017). Tropical intraseasonal oscillation simulated in an AMIP-type experiment by NICAM. *Climate Dynamics*, *48*(7), 2507–2528. https://doi.org/10.1007/s00382-016-3219-z

Kikuchi, M., Okamoto, H., Sato, K., Suzuki, K., Cesana, G., Hagihara, Y., Takahashi, N., Hayasaka, T., & Oki, R. (2017). Development of Algorithm for Discriminating Hydrometeor Particle Types With a Synergistic Use of CloudSat and CALIPSO. *Journal of Geophysical Research: Atmospheres*, *122*(20), 11,022-11,044. https://doi.org/10.1002/2017JD027113

Kodama, C., Noda, A. T., & Satoh, M. (2012). An assessment of the cloud signals simulated by NICAM using ISCCP, CALIPSO, and CloudSat satellite simulators. *Journal of Geophysical Research: Atmospheres*, *117*(D12). https://doi.org/10.1029/2011JD017317

Kodama, Chihiro, Yamada, Y., Noda, A. T., Kikuchi, K., Kajikawa, Y., Nasuno, T., Tomita, T., Yamaura, T., Takahashi, H. G., Hara, M., Kawatani, Y., Satoh, M., & Sugi, M. (2015). A 20-Year Climatology of a NICAM AMIP-Type Simulation. Journal of the Meteorological Society of Japan. Ser. II, 93(4), 393–424. https://doi.org/10.2151/jmsj.2015-024

Kodama, Chihiro, Ohno, T., Seiki, T., Yashiro, H., Noda, A. T., Nakano, M., Yamada, Y., Roh, W., Satoh, M., Nitta, T., Goto, D., Miura, H., Nasuno, T., Miyakawa, T., Chen, Y.-W., & Sugi, M. (2021). The Nonhydrostatic ICosahedral Atmospheric Model for CMIP6 HighResMIP simulations (NICAM16-S): Experimental design, model description, and

impacts of model updates. *Geoscientific Model Development*, *14*(2), 795–820. https://doi.org/10.5194/gmd-14-795-2021

Kondo, M., Sato, Y., Inatsu, M., & Katsuyama, Y. (2021). Evaluation of cloud microphysical schemes for winter snowfall events in Hokkaido: A case study of snowfall by winter monsoon. *Sola*, *advpub*. https://doi.org/10.2151/sola.2021-012

Kuba, N., Suzuki, K., Hashino, T., Seiki, T., & Satoh, M. (2015). Numerical Experiments to Analyze Cloud Microphysical Processes Depicted in Vertical Profiles of Radar Reflectivity of Warm Clouds. *Journal of the Atmospheric Sciences*, *72*(12), 4509–4528. https://doi.org/10.1175/JAS-D-15-0053.1

Kuba, N., Seiki, T., Suzuki, K., Roh, W., & Satoh, M. (2020). Evaluation of Rain Microphysics Using a Radar Simulator and Numerical Models: Comparison of Two-Moment Bulk and Spectral Bin Cloud Microphysics Schemes. *Journal of Advances in Modeling Earth Systems*, *12*(3), e2019MS001891. https://doi.org/10.1029/2019MS001891

Lang, S., Tao, W.-K., Simpson, J., Cifelli, R., Rutledge, S., Olson, W., & Halverson, J. (2007). Improving Simulations of Convective Systems from TRMM LBA: Easterly and Westerly Regimes. *Journal of the Atmospheric Sciences*, *64*(4), 1141–1164. https://doi.org/10.1175/JAS3879.1

Li, J.-L. F., Waliser, D. E., Stephens, G., Lee, S., L'Ecuyer, T., Kato, S., Loeb, N., & Ma, H.-Y. (2013). Characterizing and understanding radiation budget biases in CMIP3/CMIP5 GCMs, contemporary GCM, and reanalysis. *Journal of Geophysical Research: Atmospheres*, *118*(15), 8166–8184. https://doi.org/10.1002/jgrd.50378

Li, J.-L. F., Forbes, R. M., Waliser, D. E., Stephens, G., & Lee, S. (2014). Characterizing the radiative impacts of precipitating snow in the ECMWF Integrated Forecast System global

1162 model. *Journal of Geophysical Research: Atmospheres*, *119*(16), 9626–9637.
1163 https://doi.org/10.1002/2014JD021450

1164 Li, J.-L. F., Lee, W.-L., Waliser, D., Wang, Y.-H., Yu, J.-Y., Jiang, X., L'Ecuyer, T., Chen, Y.-C.,
1165 Kubar, T., Fetzer, E., & Mahakur, M. (2016). Considering the radiative effects of snow on
1166 tropical Pacific Ocean radiative heating profiles in contemporary GCMs using A-Train
1167 observations. *Journal of Geophysical Research: Atmospheres*, *121*(4), 1621–1636.
1168 https://doi.org/10.1002/2015JD023587

1169 Li, X., Tao, W.-K., Matsui, T., Liu, C., & Masunaga, H. (2010). Improving a spectral bin
1170 microphysical scheme using TRMM satellite observations. *Quarterly Journal of the Royal*
1171 *Meteorological Society*, *136*(647), 382–399. https://doi.org/10.1002/qj.569

1172 Liao, Liang, & Meneghini, R. (2011). A Study on the Feasibility of Dual-Wavelength Radar for
1173 Identification of Hydrometeor Phases. *Journal of Applied Meteorology and Climatology*,
1174 *50*(2), 449–456. https://doi.org/10.1175/2010JAMC2499.1

1175 Liao, L., & Meneghini, R. (2016). A Dual-Wavelength Radar Technique to Detect Hydrometeor
1176 Phases. *IEEE Transactions on Geoscience and Remote Sensing*, *54*(12), 7292–7298.
1177 https://doi.org/10.1109/TGRS.2016.2599022

1178 Liao, Liang, Meneghini, R., Tokay, A., & Kim, H. (2020). Assessment of Ku- and Ka-band Dual-
1179 frequency Radar for Snow Retrieval. *Journal of the Meteorological Society of Japan. Ser. II*,
1180 *98*(6), 1129–1146. https://doi.org/10.2151/jmsj.2020-057

1181 Lin, S.-J. (2004). A "Vertically Lagrangian" Finite-Volume Dynamical Core for Global Models.
1182 *Monthly Weather Review*, *132*(10), 2293–2307. https://doi.org/10.1175/1520-
1183 0493(2004)132<2293:AVLFDC>2.0.CO;2

1184 Lin, S.-J., & Rood, R. B. (1997). An explicit flux-form semi-lagrangian shallow-water model on
1185 the sphere. *Quarterly Journal of the Royal Meteorological Society*, *123*(544), 2477–2498.
1186 https://doi.org/10.1002/qj.49712354416
1187 Lin, Y.-L., Farley, R. D., & Orville, H. D. (1983). Bulk Parameterization of the Snow Field in a
1188 Cloud Model. *Journal of Applied Meteorology and Climatology*, *22*(6), 1065–1092.
1189 https://doi.org/10.1175/1520-0450(1983)022<1065:BPOTSF>2.0.CO;2
1190 Liou, K. N. (2002). *An Introduction to Atmospheric Radiation*. Elsevier.
1191 Liou, K.-N. (1986). Influence of Cirrus Clouds on Weather and Climate Processes: A Global
1192 Perspective. *Monthly Weather Review*, *114*(6), 1167–1199. https://doi.org/10.1175/1520-
1193 0493(1986)114<1167:IOCCOW>2.0.CO;2
1194 Locatelli, J. D., & Hobbs, P. V. (1974). Fall speeds and masses of solid precipitation particles.
1195 *Journal of Geophysical Research (1896-1977)*, *79*(15), 2185–2197.
1196 https://doi.org/10.1029/JC079i015p02185
1197 Lopez, P. (2002). Implementation and validation of a new prognostic large-scale cloud and
1198 precipitation scheme for climate and data-assimilation purposes. *Quarterly Journal of the*
1199 *Royal Meteorological Society*, *128*(579), 229–257.
1200 https://doi.org/10.1256/00359000260498879
1201 Macke, A. (1993). Scattering of light by polyhedral ice crystals. *Applied Optics*, *32*(15), 2780–
1202 2788. https://doi.org/10.1364/AO.32.002780
1203 Malardel, S., Wedi, N., Deconinck, W., Diamantakis, M., Kuehnlein, C., Mozdzynski, G.,
1204 Hamrud, M., & Smolarkiewicz, P. (2016). *A new grid for the IFS*. ECMWF.
1205 https://doi.org/10.21957/zwdu9u5i

1206 Mapes, B. E., & Houze, R. A. (1993). Cloud Clusters and Superclusters over the Oceanic Warm
1207 Pool. *Monthly Weather Review*, *121*(5), 1398–1416. https://doi.org/10.1175/1520-
1208 0493(1993)121<1398:CCASOT>2.0.CO;2
1209 Marchand, R., Haynes, J., Mace, G. G., Ackerman, T., & Stephens, G. (2009). A comparison of
1210 simulated cloud radar output from the multiscale modeling framework global climate model
1211 with CloudSat cloud radar observations. *Journal of Geophysical Research: Atmospheres*,
1212 *114*(D8). https://doi.org/10.1029/2008JD009790
1213 Masunaga, Hirohiko, L'Ecuyer, T. S., & Kummerow, C. D. (2005). Variability in the
1214 Characteristics of Precipitation Systems in the Tropical Pacific. Part I: Spatial Structure.
1215 *Journal of Climate*, *18*(6), 823–840. https://doi.org/10.1175/JCLI-3304.1
1216 Masunaga, Hirohiko, & Kummerow, C. D. (2006). Observations of tropical precipitating clouds
1217 ranging from shallow to deep convective systems. *Geophysical Research Letters*, *33*(16).
1218 https://doi.org/10.1029/2006GL026547
1219 Masunaga, H., Satoh, M., & Miura, H. (2008). A joint satellite and global cloud-resolving model
1220 analysis of a Madden-Julian Oscillation event: Model diagnosis. *Journal of Geophysical*
1221 *Research: Atmospheres*, *113*(D17). https://doi.org/10.1029/2008JD009986
1222 Masunaga, Hirohiko, Matsui, T., Tao, W., Hou, A. Y., Kummerow, C. D., Nakajima, T., Bauer,
1223 P., Olson, W. S., Sekiguchi, M., & Nakajima, T. Y. (2010). Satellite Data Simulator Unit: A
1224 Multisensor, Multispectral Satellite Simulator Package. *Bulletin of the American*
1225 *Meteorological Society*, *91*(12), 1625–1632. https://doi.org/10.1175/2010BAMS2809.1
1226 Masunaga, Hirohiko, & Bony, S. (2018). Radiative Invigoration of Tropical Convection by
1227 Preceding Cirrus Clouds. *Journal of the Atmospheric Sciences*, *75*(4), 1327–1342.
1228 https://doi.org/10.1175/JAS-D-17-0355.1

1229 Masunaga, Hirohiko, & Mapes, B. E. (2020). A Mechanism for the Maintenance of Sharp Tropical
1230 Margins. *Journal of the Atmospheric Sciences*, *77*(4), 1181–1197.
1231 https://doi.org/10.1175/JAS-D-19-0154.1
1232 Matsui, Toshihisa, Zeng, X., Tao, W.-K., Masunaga, H., Olson, W. S., & Lang, S. (2009).
1233 Evaluation of Long-Term Cloud-Resolving Model Simulations Using Satellite Radiance
1234 Observations and Multifrequency Satellite Simulators. *Journal of Atmospheric and Oceanic*
1235 *Technology*, *26*(7), 1261–1274. https://doi.org/10.1175/2008JTECHA1168.1
1236 Matsui, Toshihisa, Iguchi, T., Li, X., Han, M., Tao, W.-K., Petersen, W., L'Ecuyer, T., Meneghini,
1237 R., Olson, W., Kummerow, C. D., Hou, A. Y., Schwaller, M. R., Stocker, E. F., &
1238 Kwiatkowski, J. (2013). GPM Satellite Simulator over Ground Validation Sites. *Bulletin of*
1239 *the American Meteorological Society*, *94*(11), 1653–1660. https://doi.org/10.1175/BAMS-D-
1240 12-00160.1
1241 Matsui, T., Santanello, J., Shi, J. J., Tao, W.-K., Wu, D., Peters-Lidard, C., Kemp, E., Chin, M.,
1242 Starr, D., Sekiguchi, M., & Aires, F. (2014). Introducing multisensor satellite radiance-based
1243 evaluation for regional Earth System modeling. *Journal of Geophysical Research:*
1244 *Atmospheres*, *119*(13), 8450–8475. https://doi.org/10.1002/2013JD021424
1245 Matsui, Toshi, Chern, J.-D., Tao, W.-K., Lang, S., Satoh, M., Hashino, T., & Kubota, T. (2016).
1246 On the Land–Ocean Contrast of Tropical Convection and Microphysics Statistics Derived
1247 from TRMM Satellite Signals and Global Storm-Resolving Models. *Journal of*
1248 *Hydrometeorology*, *17*(5), 1425–1445. https://doi.org/10.1175/JHM-D-15-0111.1
1249 Matsui, Toshi, Dolan, B., Rutledge, S. A., Tao, W.-K., Iguchi, T., Barnum, J., & Lang, S. E. (2019).
1250 POLARRIS: A POLArimetric Radar Retrieval and Instrument Simulator. *Journal of*

1251 *Geophysical Research: Atmospheres*, *124*(8), 4634–4657.
1252 https://doi.org/10.1029/2018JD028317

1253 Matsui, Toshi, Zhang, S. Q., Lang, S. E., Tao, W.-K., Ichoku, C., & Peters-Lidard, C. D. (2020).
1254 Impact of radiation frequency, precipitation radiative forcing, and radiation column
1255 aggregation on convection-permitting West African monsoon simulations. *Climate*
1256 *Dynamics*, *55*(1), 193–213. https://doi.org/10.1007/s00382-018-4187-2

1257 McFarquhar, G. M., Heymsfield, A. J., Macke, A., Iaquinta, J., & Aulenbach, S. M. (1999). Use
1258 of observed ice crystal sizes and shapes to calculate mean-scattering properties and
1259 multispectral radiances: CEPEX April 4, 1993, case study. *Journal of Geophysical Research:*
1260 *Atmospheres*, *104*(D24), 31763–31779. https://doi.org/10.1029/1999JD900802

1261 Meehl, G. A., Yang, D., Arblaster, J. M., Bates, S. C., Rosenbloom, N., Neale, R., Bacmeister, J.,
1262 Lauritzen, P. H., Bryan, F., Small, J., Truesdale, J., Hannay, C., Shields, C., Strand, W. G.,
1263 Dennis, J., & Danabasoglu, G. (2019). Effects of Model Resolution, Physics, and Coupling
1264 on Southern Hemisphere Storm Tracks in CESM1.3. *Geophysical Research Letters*, *46*(21),
1265 12408–12416. https://doi.org/10.1029/2019GL084057

1266 Meehl, G. A., Senior, C. A., Eyring, V., Flato, G., Lamarque, J.-F., Stouffer, R. J., Taylor, K. E.,
1267 & Schlund, M. (2020). Context for interpreting equilibrium climate sensitivity and transient
1268 climate response from the CMIP6 Earth system models. *Science Advances*, *6*(26), eaba1981.
1269 https://doi.org/10.1126/sciadv.aba1981

1270 Michibata, T., Suzuki, K., Sekiguchi, M., & Takemura, T. (2019). Prognostic Precipitation in the
1271 MIROC6-SPRINTARS GCM: Description and Evaluation Against Satellite Observations.
1272 *Journal of Advances in Modeling Earth Systems*, *11*(3), 839–860.
1273 https://doi.org/10.1029/2018MS001596

1274 Michibata, T., & Suzuki, K. (2020). Reconciling Compensating Errors Between Precipitation
1275 Constraints and the Energy Budget in a Climate Model. *Geophysical Research Letters*,
1276 *47*(12), e2020GL088340. https://doi.org/10.1029/2020GL088340
1277 Michibata, T., Suzuki, K., & Takemura, T. (2020). Snow-induced buffering in aerosol–cloud
1278 interactions. *Atmospheric Chemistry and Physics*, *20*(22), 13771–13780.
1279 https://doi.org/10.5194/acp-20-13771-2020
1280 Milbrandt, J. A., & Yau, M. K. (2005). A Multimoment Bulk Microphysics Parameterization. Part
1281 II: A Proposed Three-Moment Closure and Scheme Description. *Journal of the Atmospheric*
1282 *Sciences*, *62*(9), 3065–3081. https://doi.org/10.1175/JAS3535.1
1283 Mitchell, D. L. (1996). Use of Mass- and Area-Dimensional Power Laws for Determining
1284 Precipitation Particle Terminal Velocities. *Journal of the Atmospheric Sciences*, *53*(12),
1285 1710–1723. https://doi.org/10.1175/1520-0469(1996)053<1710:UOMAAD>2.0.CO;2
1286 Mitchell, D. L., & Arnott, W. P. (1994). A Model Predicting the Evolution of Ice Particle Size
1287 Spectra and Radiative Properties of Cirrus Clouds. Part II: Dependence of Absorption and
1288 Extinction on Ice Crystal Morphology. *Journal of the Atmospheric Sciences*, *51*(6), 817–832.
1289 https://doi.org/10.1175/1520-0469(1994)051<0817:AMPTEO>2.0.CO;2
1290 Miura, H., Satoh, M., Nasuno, T., Noda, A. T., & Oouchi, K. (2007). A Madden-Julian Oscillation
1291 Event Realistically Simulated by a Global Cloud-Resolving Model. *Science*, *318*(5857),
1292 1763–1765. https://doi.org/10.1126/science.1148443
1293 Miura, H., Satoh, M., Tomita, H., Noda, A. T., Nasuno, T., & Iga, S. (2007). A short-duration
1294 global cloud-resolving simulation with a realistic land and sea distribution. *Geophysical*
1295 *Research Letters*, *34*(2). https://doi.org/10.1029/2006GL027448

1296 Miyakawa, T., Takayabu, Y. N., Nasuno, T., Miura, H., Satoh, M., & Moncrieff, M. W. (2012).
1297 Convective Momentum Transport by Rainbands within a Madden–Julian Oscillation in a
1298 Global Nonhydrostatic Model with Explicit Deep Convective Processes. Part I: Methodology
1299 and General Results. *Journal of the Atmospheric Sciences*, *69*(4), 1317–1338.
1300 https://doi.org/10.1175/JAS-D-11-024.1
1301 Miyakawa, T., Satoh, M., Miura, H., Tomita, H., Yashiro, H., Noda, A. T., Yamada, Y., Kodama,
1302 C., Kimoto, M., & Yoneyama, K. (2014). Madden–Julian Oscillation prediction skill of a
1303 new-generation global model demonstrated using a supercomputer. *Nature Communications*,
1304 *5*(1), 3769. https://doi.org/10.1038/ncomms4769
1305 Miyakawa, T., & Kikuchi, K. (2018). CINDY2011/DYNAMO Madden-Julian oscillation
1306 successfully reproduced in global cloud/cloud-system resolving simulations despite weak
1307 tropical wavelet power. *Scientific Reports*, *8*(1), 11664. https://doi.org/10.1038/s41598-018-
1308 29931-4
1309 Miyamoto, Y., Satoh, M., Tomita, H., Oouchi, K., Yamada, Y., Kodama, C., & Kinter, J. (2014).
1310 Gradient Wind Balance in Tropical Cyclones in High-Resolution Global Experiments.
1311 *Monthly Weather Review*, *142*(5), 1908–1926. https://doi.org/10.1175/MWR-D-13-00115.1
1312 Miyamoto, Y., Yoshida, R., Yamaura, T., Yashiro, H., Tomita, H., & Kajikawa, Y. (2015). Does
1313 convection vary in different cloud disturbances? *Atmospheric Science Letters*, *16*(3), 305–
1314 309. https://doi.org/10.1002/asl2.558
1315 Miyoshi, T., Lien, G., Satoh, S., Ushio, T., Bessho, K., Tomita, H., Nishizawa, S., Yoshida, R.,
1316 Adachi, S. A., Liao, J., Gerofi, B., Ishikawa, Y., Kunii, M., Ruiz, J., Maejima, Y., Otsuka, S.,
1317 Otsuka, M., Okamoto, K., & Seko, H. (2016). “Big Data Assimilation” Toward Post-

Petascale Severe Weather Prediction: An Overview and Progress. *Proceedings of the IEEE*, *104*(11), 2155–2179. https://doi.org/10.1109/JPROC.2016.2602560

Mizielinski, M. S., Roberts, M. J., Vidale, P. L., Schiemann, R., Demory, M.-E., Strachan, J., Edwards, T., Stephens, A., Lawrence, B. N., Pritchard, M., Chiu, P., Iwi, A., Churchill, J., del Cano Novales, C., Kettleborough, J., Roseblade, W., Selwood, P., Foster, M., Glover, M., & Malcolm, A. (2014). High-resolution global climate modelling: The UPSCALE project, a large-simulation campaign. *Geoscientific Model Development*, *7*(4), 1629–1640. https://doi.org/10.5194/gmd-7-1629-2014

Morrison, H., & Gettelman, A. (2008). A New Two-Moment Bulk Stratiform Cloud Microphysics Scheme in the Community Atmosphere Model, Version 3 (CAM3). Part I: Description and Numerical Tests. *Journal of Climate*, *21*(15), 3642–3659. https://doi.org/10.1175/2008JCLI2105.1

Morrison, H., & Grabowski, W. W. (2008). Modeling Supersaturation and Subgrid-Scale Mixing with Two-Moment Bulk Warm Microphysics. *Journal of the Atmospheric Sciences*, *65*(3), 792–812. https://doi.org/10.1175/2007JAS2374.1

Morrison, H., de Boer, G., Feingold, G., Harrington, J., Shupe, M. D., & Sulia, K. (2012). Resilience of persistent Arctic mixed-phase clouds. *Nature Geoscience*, *5*(1), 11–17. https://doi.org/10.1038/ngeo1332

Mroz, K., Battaglia, A., Lang, T. J., Tanelli, S., & Sacco, G. F. (2018). Global Precipitation Measuring Dual-Frequency Precipitation Radar Observations of Hailstorm Vertical Structure: Current Capabilities and Drawbacks. *Journal of Applied Meteorology and Climatology*, *57*(9), 2161–2178. https://doi.org/10.1175/JAMC-D-18-0020.1

1340 Nakajima, T., & King, M. D. (1990). Determination of the Optical Thickness and Effective Particle
1341 Radius of Clouds from Reflected Solar Radiation Measurements. Part I: Theory. *Journal of*
1342 *the Atmospheric Sciences*, *47*(15), 1878–1893. https://doi.org/10.1175/1520-
1343 0469(1990)047<1878:DOTOTA>2.0.CO;2
1344 Nakajima, T., Tsukamoto, M., Tsushima, Y., Numaguti, A., & Kimura, T. (2000). Modeling of
1345 the radiative process in an atmospheric general circulation model. *Applied Optics*, *39*(27),
1346 4869–4878. https://doi.org/10.1364/AO.39.004869
1347 Nakajima, T. Y., Suzuki, K., & Stephens, G. L. (2010). Droplet Growth in Warm Water Clouds
1348 Observed by the A-Train. Part II: A Multisensor View. *Journal of the Atmospheric Sciences*,
1349 *67*(6), 1897–1907. https://doi.org/10.1175/2010JAS3276.1
1350 Nakano, Masuo, Sawada, M., Nasuno, T., & Satoh, M. (2015). Intraseasonal variability and
1351 tropical cyclogenesis in the western North Pacific simulated by a global nonhydrostatic
1352 atmospheric model. *Geophysical Research Letters*, *42*(2), 565–571.
1353 https://doi.org/10.1002/2014GL062479
1354 Nakano, Masuo, Wada, A., Sawada, M., Yoshimura, H., Onishi, R., Kawahara, S., Sasaki, W.,
1355 Nasuno, T., Yamaguchi, M., Iriguchi, T., Sugi, M., & Takeuchi, Y. (2017). Global 7 km mesh
1356 nonhydrostatic Model Intercomparison Project for improving TYphoon forecast (TYMIP-
1357 G7): Experimental design and preliminary results. *Geoscientific Model Development*, *10*(3),
1358 1363–1381. https://doi.org/10.5194/gmd-10-1363-2017
1359 Nakano, M., & Kikuchi, K. (2019). Seasonality of Intraseasonal Variability in Global Climate
1360 Models. *Geophysical Research Letters*, *46*(8), 4441–4449.
1361 https://doi.org/10.1029/2019GL082443

1362 Nam, C., Bony, S., Dufresne, J.-L., & Chepfer, H. (2012). The 'too few, too bright' tropical low-
1363 cloud problem in CMIP5 models. *Geophysical Research Letters*, *39*(21).
1364 https://doi.org/10.1029/2012GL053421
1365 Nasuno, T., Miura, H., Satoh, M., Noda, A. T., & Oouchi, K. (2009). Multi-scale Organization of
1366 Convection in a Global Numerical Simulation of the December 2006 MJO Event Using
1367 Explicit Moist Processes. *Journal of the Meteorological Society of Japan. Ser. II*, *87*(2), 335–
1368 345. https://doi.org/10.2151/jmsj.87.335
1369 Nasuno, T., Kikuchi, K., Nakano, M., Yamada, Y., Ikeda, M., & Taniguchi, H. (2017). Evaluation
1370 of the Near Real-Time Forecasts Using a Global Nonhydrostatic Model during the
1371 CINDY2011/DYNAMO. *Journal of the Meteorological Society of Japan. Ser. II*, *95*(6), 345–
1372 368. https://doi.org/10.2151/jmsj.2017-022
1373 Nishizawa, S., Yashiro, H., Sato, Y., Miyamoto, Y., & Tomita, H. (2015). Influence of grid aspect
1374 ratio on planetary boundary layer turbulence in large-eddy simulations. *Geoscientific Model*
1375 *Development*, *8*(10), 3393–3419. https://doi.org/10.5194/gmd-8-3393-2015
1376 Noda, A. T., Satoh, M., Yamada, Y., Kodama, C., & Seiki, T. (2014). Responses of Tropical and
1377 Subtropical High-Cloud Statistics to Global Warming. *Journal of Climate*, *27*(20), 7753–
1378 7768. https://doi.org/10.1175/JCLI-D-14-00179.1
1379 Noda, A. T., Seiki, T., Satoh, M., & Yamada, Y. (2016). High cloud size dependency in the
1380 applicability of the fixed anvil temperature hypothesis using global nonhydrostatic
1381 simulations. *Geophysical Research Letters*, *43*(5), 2307–2314.
1382 https://doi.org/10.1002/2016GL067742
1383 Noda, Akira T., Kodama, C., Yamada, Y., Satoh, M., Ogura, T., & Ohno, T. (2019). Responses of
1384 Clouds and Large-Scale Circulation to Global Warming Evaluated From Multidecadal

Simulations Using a Global Nonhydrostatic Model. *Journal of Advances in Modeling Earth Systems*, *11*(9), 2980–2995. https://doi.org/10.1029/2019MS001658

Okamoto, K. (2017). Evaluation of IR radiance simulation for all-sky assimilation of Himawari-8/AHI in a mesoscale NWP system. *Quarterly Journal of the Royal Meteorological Society*, *143*(704), 1517–1527. https://doi.org/10.1002/qj.3022

Okamoto, K., Sawada, Y., & Kunii, M. (2019). Comparison of assimilating all-sky and clear-sky infrared radiances from Himawari-8 in a mesoscale system. *Quarterly Journal of the Royal Meteorological Society*, *145*(719), 745–766. https://doi.org/10.1002/qj.3463

Okata, M., Nakajima, T., Suzuki, K., Inoue, T., Nakajima, T. Y., & Okamoto, H. (2017). A study on radiative transfer effects in 3-D cloudy atmosphere using satellite data. *Journal of Geophysical Research: Atmospheres*, *122*(1), 443–468. https://doi.org/10.1002/2016JD025441

Onishi, R., Sugiyama, D., & Matsuda, K. (2019). Super-Resolution Simulation for Real-Time Prediction of Urban Micrometeorology. *Sola*, *15*, 178–182. https://doi.org/10.2151/sola.2019-032

Oouchi, K., Noda, A. T., Satoh, M., Miura, H., Tomita, H., Nasuno, T., & Iga, S. (2009). A Simulated Preconditioning of Typhoon Genesis Controlled by a Boreal Summer Madden-Julian Oscillation Event in a Global Cloud-system-resolving Model. *Sola*, *5*, 65–68. https://doi.org/10.2151/sola.2009-017

Park, S., Bretherton, C. S., & Rasch, P. J. (2014). Integrating Cloud Processes in the Community Atmosphere Model, Version 5. *Journal of Climate*, *27*(18), 6821–6856. https://doi.org/10.1175/JCLI-D-14-00087.1

1407 Phillips, V. T. J., Donner, L. J., & Garner, S. T. (2007). Nucleation Processes in Deep Convection
1408 Simulated by a Cloud-System-Resolving Model with Double-Moment Bulk Microphysics.
1409 *Journal of the Atmospheric Sciences*, *64*(3), 738–761. https://doi.org/10.1175/JAS3869.1
1410 Pollack, J. B., & Cuzzi, J. N. (1980). Scattering by Nonspherical Particles of Size Comparable to
1411 a Wavelength: A New Semi-Empirical Theory and Its Application to Tropospheric Aerosols.
1412 *Journal of the Atmospheric Sciences*, *37*(4), 868–881. https://doi.org/10.1175/1520-
1413 0469(1980)037<0868:SBNPOS>2.0.CO;2
1414 Posselt, R., & Lohmann, U. (2008). Introduction of prognostic rain in ECHAM5: Design and
1415 single column model simulations. *Atmospheric Chemistry and Physics*, *8*(11), 2949–2963.
1416 https://doi.org/10.5194/acp-8-2949-2008
1417 Pruppacher, H. R., & Klett, J. D. (2010). *Microphysics of Clouds and Precipitation* (2nd ed.).
1418 Springer Netherlands. https://doi.org/10.1007/978-0-306-48100-0
1419 Putman, W. M., & Lin, S.-J. (2007). Finite-volume transport on various cubed-sphere grids.
1420 *Journal of Computational Physics*, *227*(1), 55–78. https://doi.org/10.1016/j.jcp.2007.07.022
1421 Putman, W. M., & Suarez, M. (2011). Cloud-system resolving simulations with the NASA
1422 Goddard Earth Observing System global atmospheric model (GEOS-5). *Geophysical*
1423 *Research Letters*, *38*(16). https://doi.org/10.1029/2011GL048438
1424 Randall, D. A., Genio, A. D. D., Donner, L. J., Collins, W. D., & Klein, S. A. (2016). The Impact
1425 of ARM on Climate Modeling. *Meteorological Monographs*, *57*(1), 26.1-26.16.
1426 https://doi.org/10.1175/AMSMONOGRAPHS-D-15-0050.1
1427 Ren, C., & Mackenzie, A. R. (2005). Cirrus parametrization and the role of ice nuclei. *Quarterly*
1428 *Journal of the Royal Meteorological Society*, *131*(608), 1585–1605.
1429 https://doi.org/10.1256/qj.04.126

1430 Reverdy, M., Chepfer, H., Donovan, D., Noel, V., Cesana, G., Hoareau, C., Chiriaco, M., & Bastin,
1431 S. (2015). An EarthCARE/ATLID simulator to evaluate cloud description in climate models.
1432 *Journal of Geophysical Research: Atmospheres*, *120*(21), 11,090-11,113.
1433 https://doi.org/10.1002/2015JD023919
1434 Roberts, M. J., Vidale, P. L., Senior, C., Hewitt, H. T., Bates, C., Berthou, S., Chang, P.,
1435 Christensen, H. M., Danilov, S., Demory, M.-E., Griffies, S. M., Haarsma, R., Jung, T.,
1436 Martin, G., Minobe, S., Ringler, T., Satoh, M., Schiemann, R., Scoccimarro, E., … Wehner,
1437 M. F. (2018). The Benefits of Global High Resolution for Climate Simulation: Process
1438 Understanding and the Enabling of Stakeholder Decisions at the Regional Scale. *Bulletin of*
1439 *the American Meteorological Society*, *99*(11), 2341–2359. https://doi.org/10.1175/BAMS-D-
1440 15-00320.1
1441 Roehrig, R., Beau, I., Saint-Martin, D., Alias, A., Decharme, B., Guérémy, J.-F., Voldoire, A.,
1442 Abdel-Lathif, A. Y., Bazile, E., Belamari, S., Blein, S., Bouniol, D., Bouteloup, Y., Cattiaux,
1443 J., Chauvin, F., Chevallier, M., Colin, J., Douville, H., Marquet, P., … Sénési, S. (2020). The
1444 CNRM Global Atmosphere Model ARPEGE-Climat 6.3: Description and Evaluation.
1445 *Journal of Advances in Modeling Earth Systems*, *12*(7), e2020MS002075.
1446 https://doi.org/10.1029/2020MS002075
1447 Roh, W., & Satoh, M. (2014). Evaluation of Precipitating Hydrometeor Parameterizations in a
1448 Single-Moment Bulk Microphysics Scheme for Deep Convective Systems over the Tropical
1449 Central Pacific. *Journal of the Atmospheric Sciences*, *71*(7), 2654–2673.
1450 https://doi.org/10.1175/JAS-D-13-0252.1

1451 Roh, W., Satoh, M., & Nasuno, T. (2017). Improvement of a Cloud Microphysics Scheme for a
1452 Global Nonhydrostatic Model Using TRMM and a Satellite Simulator. *Journal of the*
1453 *Atmospheric Sciences*, *74*(1), 167–184. https://doi.org/10.1175/JAS-D-16-0027.1
1454 Roh, W., & Satoh, M. (2018). Extension of a Multisensor Satellite Radiance-Based Evaluation for
1455 Cloud System Resolving Models. *Journal of the Meteorological Society of Japan. Ser. II*,
1456 *96*(1), 55–63. https://doi.org/10.2151/jmsj.2018-002
1457 Roh, W., Satoh, M., Hashino, T., Okamoto, H., & Seiki, T. (2020). Evaluations of the
1458 Thermodynamic Phases of Clouds in a Cloud-System-Resolving Model Using CALIPSO and
1459 a Satellite Simulator over the Southern Ocean. *Journal of the Atmospheric Sciences*, *77*(11),
1460 3781–3801. https://doi.org/10.1175/JAS-D-19-0273.1
1461 Rossow, W. B., & Schiffer, R. A. (1999). Advances in Understanding Clouds from ISCCP.
1462 *Bulletin of the American Meteorological Society*, *80*(11), 2261–2288.
1463 https://doi.org/10.1175/1520-0477(1999)080<2261:AIUCFI>2.0.CO;2
1464 Rutledge, S. A., & Hobbs, P. V. (1984). The Mesoscale and Microscale Structure and Organization
1465 of Clouds and Precipitation in Midlatitude Cyclones. XII: A Diagnostic Modeling Study of
1466 Precipitation Development in Narrow Cold-Frontal Rainbands. *Journal of the Atmospheric*
1467 *Sciences*, *41*(20), 2949–2972. https://doi.org/10.1175/1520-
1468 0469(1984)041<2949:TMAMSA>2.0.CO;2
1469 Saito, K., Ishida, J., Aranami, K., Hara, T., Segawa, T., Narita, M., & Honda, Y. (2007).
1470 Nonhydrostatic Atmospheric Models and Operational Development at JMA. *Journal of the*
1471 *Meteorological Society of Japan. Ser. II*, *85B*, 271–304. https://doi.org/10.2151/jmsj.85B.271
1472 Saito, M., Iwabuchi, H., Yang, P., Tang, G., King, M. D., & Sekiguchi, M. (2017). Ice particle
1473 morphology and microphysical properties of cirrus clouds inferred from combined CALIOP-

IIR measurements. *Journal of Geophysical Research: Atmospheres*, *122*(8), 4440–4462. https://doi.org/10.1002/2016JD026080

Sant, V., Posselt, R., & Lohmann, U. (2015). Prognostic precipitation with three liquid water classes in the ECHAM5–HAM GCM. *Atmospheric Chemistry and Physics*, *15*(15), 8717–8738. https://doi.org/10.5194/acp-15-8717-2015

Sasaki, W., Onishi, R., Fuchigami, H., Goto, K., Nishikawa, S., Ishikawa, Y., & Takahashi, K. (2016). MJO simulation in a cloud-system-resolving global ocean-atmosphere coupled model. *Geophysical Research Letters*, *43*(17), 9352–9360. https://doi.org/10.1002/2016GL070550

Sassen, K., Wang, Z., & Liu, D. (2008). Global distribution of cirrus clouds from CloudSat/Cloud-Aerosol Lidar and Infrared Pathfinder Satellite Observations (CALIPSO) measurements. *Journal of Geophysical Research: Atmospheres*, *113*(D8). https://doi.org/10.1029/2008JD009972

Sato, Y., Nishizawa, S., Yashiro, H., Miyamoto, Y., Kajikawa, Y., & Tomita, H. (2015). Impacts of cloud microphysics on trade wind cumulus: Which cloud microphysics processes contribute to the diversity in a large eddy simulation? *Progress in Earth and Planetary Science*, *2*(1), 23. https://doi.org/10.1186/s40645-015-0053-6

Sato, Y., Shima, S., & Tomita, H. (2018). Numerical Convergence of Shallow Convection Cloud Field Simulations: Comparison Between Double-Moment Eulerian and Particle-Based Lagrangian Microphysics Coupled to the Same Dynamical Core. *Journal of Advances in Modeling Earth Systems*, *10*(7), 1495–1512. https://doi.org/10.1029/2018MS001285

1495 Sato, Y., Miyamoto, Y., & Tomita, H. (2019). Large dependency of charge distribution in a tropical
1496 cyclone inner core upon aerosol number concentration. *Progress in Earth and Planetary*
1497 *Science*, *6*(1), 62. https://doi.org/10.1186/s40645-019-0309-7
1498 Satoh, M. (2002). Conservative Scheme for the Compressible Nonhydrostatic Models with the
1499 Horizontally Explicit and Vertically Implicit Time Integration Scheme. *Monthly Weather*
1500 *Review*, *130*(5), 1227–1245. https://doi.org/10.1175/1520-
1501 0493(2002)130<1227:CSFTCN>2.0.CO;2
1502 Satoh, M. (2003). Conservative Scheme for a Compressible Nonhydrostatic Model with Moist
1503 Processes. *Monthly Weather Review*, *131*(6), 1033–1050. https://doi.org/10.1175/1520-
1504 0493(2003)131<1033:CSFACN>2.0.CO;2
1505 Satoh, M., Matsuno, T., Tomita, H., Miura, H., Nasuno, T., & Iga, S. (2008a). Nonhydrostatic
1506 icosahedral atmospheric model (NICAM) for global cloud resolving simulations. *Journal of*
1507 *Computational Physics*, *227*(7), 3486–3514. https://doi.org/10.1016/j.jcp.2007.02.006
1508 Satoh, M., Nasuno, T., Miura, H., Tomita, H., Iga, S., & Takayabu, Y. (2008b). Precipitation
1509 Statistics Comparison Between Global Cloud Resolving Simulation with NICAM and
1510 TRMM PR Data. In K. Hamilton & W. Ohfuchi (Eds.), *High Resolution Numerical Modelling*
1511 *of the Atmosphere and Ocean* (pp. 99–112). Springer. https://doi.org/10.1007/978-0-387-
1512 49791-4_6
1513 Satoh, M, Inoue, T., & Miura, H. (2010). Evaluations of cloud properties of global and local cloud
1514 system resolving models using CALIPSO and CloudSat simulators. *Journal of Geophysical*
1515 *Research: Atmospheres*, *115*(D4). https://doi.org/10.1029/2009JD012247
1516 Satoh, M., Tomita, H., Yashiro, H., Miura, H., Kodama, C., Seiki, T., Noda, A. T., Yamada, Y.,
1517 Goto, D., Sawada, M., Miyoshi, T., Niwa, Y., Hara, M., Ohno, T., Iga, S., Arakawa, T., Inoue,

1518 T., & Kubokawa, H. (2014). The Non-hydrostatic Icosahedral Atmospheric Model:
1519 Description and development. *Progress in Earth and Planetary Science*, *1*(1), 18.
1520 https://doi.org/10.1186/s40645-014-0018-1
1521 Satoh, M., Roh, W., and Hashino, T. (2016). Evaluations of clouds and precipitations in NICAM
1522 using the joint simulator for satellite sensors. CGER'S SUPERCOMPUTER MONOGRAPH
1523 REPORT Vol.22. http://www.cger.nies.go.jp/publications/report/i127/i127.pdf.
1524 Satoh, M., Tomita, H., Yashiro, H., Kajikawa, Y., Miyamoto, Y., Yamaura, T., Miyakawa, T.,
1525 Nakano, M., Kodama, C., Noda, A. T., Nasuno, T., Yamada, Y., & Fukutomi, Y. (2017).
1526 Outcomes and challenges of global high-resolution non-hydrostatic atmospheric simulations
1527 using the K computer. *Progress in Earth and Planetary Science*, *4*(1), 13.
1528 https://doi.org/10.1186/s40645-017-0127-8
1529 Satoh, M, Noda, A. T., Seiki, T., Chen, Y.-W., Kodama, C., Yamada, Y., Kuba, N., & Sato, Y.
1530 (2018). Toward reduction of the uncertainties in climate sensitivity due to cloud processes
1531 using a global non-hydrostatic atmospheric model. *Progress in Earth and Planetary Science*,
1532 *5*(1), 67. https://doi.org/10.1186/s40645-018-0226-1
1533 Satoh, M., Stevens, B., Judt, F., Khairoutdinov, M., Lin, S.-J., Putman, W. M., & Düben, P. (2019).
1534 Global Cloud-Resolving Models. *Current Climate Change Reports*, *5*(3), 172–184.
1535 https://doi.org/10.1007/s40641-019-00131-0
1536 Saunders, R., Hocking, J., Turner, E., Rayer, P., Rundle, D., Brunel, P., Vidot, J., Roquet, P.,
1537 Matricardi, M., Geer, A., Bormann, N., & Lupu, C. (2018). An update on the RTTOV fast
1538 radiative transfer model (currently at version 12). *Geoscientific Model Development*, *11*(7),
1539 2717–2737. https://doi.org/10.5194/gmd-11-2717-2018

1540 Schär, C., Fuhrer, O., Arteaga, A., Ban, N., Charpilloz, C., Girolamo, S. D., Hentgen, L., Hoefler,
1541 T., Lapillonne, X., Leutwyler, D., Osterried, K., Panosetti, D., Rüdisühli, S., Schlemmer, L.,
1542 Schulthess, T. C., Sprenger, M., Ubbiali, S., & Wernli, H. (2020). Kilometer-Scale Climate
1543 Models: Prospects and Challenges. *Bulletin of the American Meteorological Society*, *101*(5),
1544 E567–E587. https://doi.org/10.1175/BAMS-D-18-0167.1

1545 Seifert, A. (2008). On the Parameterization of Evaporation of Raindrops as Simulated by a One-
1546 Dimensional Rainshaft Model. *Journal of the Atmospheric Sciences*, *65*(11), 3608–3619.
1547 https://doi.org/10.1175/2008JAS2586.1

1548 Seifert, A., & Beheng, K. D. (2001). A double-moment parameterization for simulating
1549 autoconversion, accretion and selfcollection. *Atmospheric Research*, *59–60*, 265–281.
1550 https://doi.org/10.1016/S0169-8095(01)00126-0

1551 Seifert, A., & Beheng, K. D. (2006). A two-moment cloud microphysics parameterization for
1552 mixed-phase clouds. Part 1: Model description. *Meteorology and Atmospheric Physics*, *92*(1),
1553 45–66. https://doi.org/10.1007/s00703-005-0112-4

1554 Seifert, A., Khain, A., Pokrovsky, A., & Beheng, K. D. (2006). A comparison of spectral bin and
1555 two-moment bulk mixed-phase cloud microphysics. *Atmospheric Research*, *80*(1), 46–66.
1556 https://doi.org/10.1016/j.atmosres.2005.06.009

1557 Seiki, T. (2021). Near-Global Three-Dimensional Hail Signals Detected by Using GPM-DPR
1558 Observations. *Journal of the Meteorological Society of Japan. Ser. II*, *advpub*.
1559 https://doi.org/10.2151/jmsj.2021-018

1560 Seiki, T., & Nakajima, T. (2014). Aerosol Effects of the Condensation Process on a Convective
1561 Cloud Simulation. *Journal of the Atmospheric Sciences*, *71*(2), 833–853.
1562 https://doi.org/10.1175/JAS-D-12-0195.1

1563 Seiki, T., Kodama, C., Noda, A. T., & Satoh, M. (2015a). Improvement in Global Cloud-System-
1564 Resolving Simulations by Using a Double-Moment Bulk Cloud Microphysics Scheme.
1565 *Journal of Climate*, *28*(6), 2405–2419. https://doi.org/10.1175/JCLI-D-14-00241.1
1566 Seiki, T., Kodama, C., Satoh, M., Hashino, T., Hagihara, Y., & Okamoto, H. (2015b). Vertical
1567 grid spacing necessary for simulating tropical cirrus clouds with a high-resolution
1568 atmospheric general circulation model. *Geophysical Research Letters*, *42*(10), 4150–4157.
1569 https://doi.org/10.1002/2015GL064282
1570 Seiki, T., Kodama, C., Satoh, M., Hagihara, Y., & Okamoto, H. (2019). Characteristics of Ice
1571 Clouds Over Mountain Regions Detected by CALIPSO and CloudSat Satellite Observations.
1572 *Journal of Geophysical Research: Atmospheres*, *124*(20), 10858–10877.
1573 https://doi.org/10.1029/2019JD030519
1574 Seiki, T., & Roh, W. (2020). Improvements in Supercooled Liquid Water Simulations of Low-
1575 Level Mixed-Phase Clouds over the Southern Ocean Using a Single-Column Model. *Journal*
1576 *of the Atmospheric Sciences*, *77*(11), 3803–3819. https://doi.org/10.1175/JAS-D-19-0266.1
1577 Seiki, T., Satoh, M., Tomita, H., & Nakajima, T. (2014). Simultaneous evaluation of ice cloud
1578 microphysics and nonsphericity of the cloud optical properties using hydrometeor video
1579 sonde and radiometer sonde in situ observations. *Journal of Geophysical Research:*
1580 *Atmospheres*, *119*(11), 6681–6701. https://doi.org/10.1002/2013JD021086
1581 Sekiguchi, M., & Nakajima, T. (2008). A k-distribution-based radiation code and its computational
1582 optimization for an atmospheric general circulation model. *Journal of Quantitative*
1583 *Spectroscopy and Radiative Transfer*, *109*(17), 2779–2793.
1584 https://doi.org/10.1016/j.jqsrt.2008.07.013

1585 Senf, F., Voigt, A., Clerbaux, N., Hünerbein, A., & Deneke, H. (2020). Increasing Resolution and
1586 Resolving Convection Improve the Simulation of Cloud-Radiative Effects Over the North
1587 Atlantic. *Journal of Geophysical Research: Atmospheres*, *125*(19), e2020JD032667.
1588 https://doi.org/10.1029/2020JD032667
1589 Sherwood, S. C., Webb, M. J., Annan, J. D., Armour, K. C., Forster, P. M., Hargreaves, J. C.,
1590 Hegerl, G., Klein, S. A., Marvel, K. D., Rohling, E. J., Watanabe, M., Andrews, T.,
1591 Braconnot, P., Bretherton, C. S., Foster, G. L., Hausfather, Z., Heydt, A. S. von der, Knutti,
1592 R., Mauritsen, T., Zelinka, M. D. (2020). An Assessment of Earth's Climate Sensitivity Using
1593 Multiple Lines of Evidence. *Reviews of Geophysics*, *58*(4), e2019RG000678.
1594 https://doi.org/10.1029/2019RG000678
1595 Shibuya, R., Miura, H., & Sato, K. (2016). A Grid Transformation Method for a Quasi-Uniform,
1596 Circular Fine Region Using the Spring Dynamics. *Journal of the Meteorological Society of*
1597 *Japan. Ser. II*, *94*(5), 443–452. https://doi.org/10.2151/jmsj.2016-022
1598 Shipway, B. J., & Hill, A. A. (2012). Diagnosis of systematic differences between multiple
1599 parametrizations of warm rain microphysics using a kinematic framework. *Quarterly Journal*
1600 *of the Royal Meteorological Society*, *138*(669), 2196–2211. https://doi.org/10.1002/qj.1913
1601 Shupe, M. D., & Intrieri, J. M. (2004). Cloud Radiative Forcing of the Arctic Surface: The
1602 Influence of Cloud Properties, Surface Albedo, and Solar Zenith Angle. *Journal of Climate*,
1603 *17*(3), 616–628. https://doi.org/10.1175/1520-0442(2004)017<0616:CRFOTA>2.0.CO;2
1604 Skamarock, W. C., Klemp, J. B., Duda, M. G., Fowler, L. D., Park, S.-H., & Ringler, T. D. (2012).
1605 A Multiscale Nonhydrostatic Atmospheric Model Using Centroidal Voronoi Tesselations and
1606 C-Grid Staggering. *Monthly Weather Review*, *140*(9), 3090–3105.
1607 https://doi.org/10.1175/MWR-D-11-00215.1

1608 Skamarock, W. C., Duda, M. G., Ha, S., & Park, S.-H. (2018). Limited-Area Atmospheric
1609 Modeling Using an Unstructured Mesh. *Monthly Weather Review*, *146*(10), 3445–3460.
1610 https://doi.org/10.1175/MWR-D-18-0155.1
1611 Sölch, I., & Kärcher, B. (2011). Process-oriented large-eddy simulations of a midlatitude cirrus
1612 cloud system based on observations. *Quarterly Journal of the Royal Meteorological Society*,
1613 *137*(655), 374–393. https://doi.org/10.1002/qj.764
1614 Song, X., Zhang, G. J., & Li, J.-L. F. (2012). Evaluation of Microphysics Parameterization for
1615 Convective Clouds in the NCAR Community Atmosphere Model CAM5. *Journal of Climate*,
1616 *25*(24), 8568–8590. https://doi.org/10.1175/JCLI-D-11-00563.1
1617 Stephens, G. L., Tsay, S.-C., Stackhouse, P. W., & Flatau, P. J. (1990). The Relevance of the
1618 Microphysical and Radiative Properties of Cirrus Clouds to Climate and Climatic Feedback.
1619 *Journal of the Atmospheric Sciences*, *47*(14), 1742–1754. https://doi.org/10.1175/1520-
1620 0469(1990)047<1742:TROTMA>2.0.CO;2
1621 Stephens, G. L., Vane, D. G., Tanelli, S., Im, E., Durden, S., Rokey, M., Reinke, D., Partain, P.,
1622 Mace, G. G., Austin, R., L'Ecuyer, T., Haynes, J., Lebsock, M., Suzuki, K., Waliser, D., Wu,
1623 D., Kay, J., Gettelman, A., Wang, Z., & Marchand, R. (2008). CloudSat mission: Performance
1624 and early science after the first year of operation. *Journal of Geophysical Research:*
1625 *Atmospheres*, *113*(D8). https://doi.org/10.1029/2008JD009982
1626 Stevens, B., & Feingold, G. (2009). Untangling aerosol effects on clouds and precipitation in a
1627 buffered system. *Nature*, *461*(7264), 607–613. https://doi.org/10.1038/nature08281
1628 Stevens, B., Satoh, M., Auger, L., Biercamp, J., Bretherton, C. S., Chen, X., Düben, P., Judt, F.,
1629 Khairoutdinov, M., Klocke, D., Kodama, C., Kornblueh, L., Lin, S.-J., Neumann, P., Putman,
1630 W. M., Röber, N., Shibuya, R., Vanniere, B., Vidale, P. L., … Zhou, L. (2019). DYAMOND:

1631 The DYnamics of the Atmospheric general circulation Modeled On Non-hydrostatic
1632 Domains. *Progress in Earth and Planetary Science*, *6*(1), 61. https://doi.org/10.1186/s40645-
1633 019-0304-z
1634 Stevens, B., Acquistapace, C., Hansen, A., Heinze, R., Klinger, C., Klocke, D., Rybka, H.,
1635 Schubotz, W., Windmiller, J., Adamidis, P., Arka, I., Barlakas, V., Biercamp, J., Brueck, M.,
1636 Brune, S., Buehler, S. A., Burkhardt, U., Cioni, G., Costa-Surós, M., … Zängl, G. (2020).
1637 The Added Value of Large-eddy and Storm-resolving Models for Simulating Clouds and
1638 Precipitation. *Journal of the Meteorological Society of Japan. Ser. II*, *98*(2), 395–435.
1639 https://doi.org/10.2151/jmsj.2020-021
1640 Stockdale, T. N. (1997). Coupled Ocean–Atmosphere Forecasts in the Presence of Climate Drift.
1641 *Monthly Weather Review*, *125*(5), 809–818. https://doi.org/10.1175/1520-
1642 0493(1997)125<0809:COAFIT>2.0.CO;2
1643 Sueki, K., Yamaura, T., Yashiro, H., Nishizawa, S., Yoshida, R., Kajikawa, Y., & Tomita, H.
1644 (2019). Convergence of Convective Updraft Ensembles With Respect to the Grid Spacing of
1645 Atmospheric Models. *Geophysical Research Letters*, *46*(24), 14817–14825.
1646 https://doi.org/10.1029/2019GL084491
1647 Suzuki, K., Nakajima, T. Y., & Stephens, G. L. (2010). Particle Growth and Drop Collection
1648 Efficiency of Warm Clouds as Inferred from Joint CloudSat and MODIS Observations.
1649 *Journal of the Atmospheric Sciences*, *67*(9), 3019–3032.
1650 https://doi.org/10.1175/2010JAS3463.1
1651 Suzuki, K., Stephens, G. L., Heever, S. C. van den, & Nakajima, T. Y. (2011). Diagnosis of the
1652 Warm Rain Process in Cloud-Resolving Models Using Joint CloudSat and MODIS

1653 Observations. *Journal of the Atmospheric Sciences*, *68*(11), 2655–2670.
1654 https://doi.org/10.1175/JAS-D-10-05026.1
1655 Suzuki, K., Golaz, J.-C., & Stephens, G. L. (2013). Evaluating cloud tuning in a climate model
1656 with satellite observations. *Geophysical Research Letters*, *40*(16), 4464–4468.
1657 https://doi.org/10.1002/grl.50874
1658 Suzuki, K., Stephens, G., Bodas-Salcedo, A., Wang, M., Golaz, J.-C., Yokohata, T., & Koshiro,
1659 T. (2015). Evaluation of the Warm Rain Formation Process in Global Models with Satellite
1660 Observations. *Journal of the Atmospheric Sciences*, *72*(10), 3996–4014.
1661 https://doi.org/10.1175/JAS-D-14-0265.1
1662 Swales, D. J., Pincus, R., & Bodas-Salcedo, A. (2018). The Cloud Feedback Model
1663 Intercomparison Project Observational Simulator Package: Version 2. *Geoscientific Model*
1664 *Development*, *11*(1), 77–81. https://doi.org/10.5194/gmd-11-77-2018
1665 Takahashi, K., Peng, X., Onishi, R., Ohdaira, M., Goto, K., Fuchigami, H., & Sugimura, T. (2008).
1666 Impact of Coupled Nonhydrostatic Atmosphere-Ocean-Land Model with High Resolution. In
1667 K. Hamilton & W. Ohfuchi (Eds.), *High Resolution Numerical Modelling of the Atmosphere*
1668 *and Ocean* (pp. 261–273). Springer. https://doi.org/10.1007/978-0-387-49791-4_15
1669 Takano, Y., & Liou, K.-N. (1989). Solar Radiative Transfer in Cirrus Clouds. Part I: Single-
1670 Scattering and Optical Properties of Hexagonal Ice Crystals. *Journal of the Atmospheric*
1671 *Sciences*, *46*(1), 3–19. https://doi.org/10.1175/1520-
1672 0469(1989)046<0003:SRTICC>2.0.CO;2
1673 Takano, Y., & Liou, K. N. (1995). Radiative Transfer in Cirrus Clouds. Part III: Light Scattering
1674 by Irregular Ice Crystals. *Journal of the Atmospheric Sciences*, *52*(7), 818–837.
1675 https://doi.org/10.1175/1520-0469(1995)052<0818:RTICCP>2.0.CO;2

1676 Takasuka, D., Miyakawa, T., Satoh, M., & Miura, H. (2015). Topographical Effects on Internally
1677 Produced MJO-Like Disturbances in an Aqua-Planet Version of NICAM. *Sola*, *11*, 170–176.
1678 https://doi.org/10.2151/sola.2015-038
1679 Takasuka, D., Satoh, M., Miyakawa, T., & Miura, H. (2018). Initiation Processes of the Tropical
1680 Intraseasonal Variability Simulated in an Aqua-Planet Experiment: What is the Intrinsic
1681 Mechanism for MJO Onset? *Journal of Advances in Modeling Earth Systems*, *10*(4), 1047–
1682 1073. https://doi.org/10.1002/2017MS001243
1683 Takayabu, Y. N. (2002). Spectral representation of rain profiles and diurnal variations observed
1684 with TRMM PR over the equatorial area. *Geophysical Research Letters*, *29*(12), 25-1-25–4.
1685 https://doi.org/10.1029/2001GL014113
1686 Taniguchi, H., Yanase, W., & Satoh, M. (2010). Ensemble Simulation of Cyclone Nargis by a
1687 Global Cloud-System-Resolving Model—Modulation of Cyclogenesis by the Madden-Julian
1688 Oscillation. *Journal of the Meteorological Society of Japan. Ser. II*, *88*(3), 571–591.
1689 https://doi.org/10.2151/jmsj.2010-317
1690 Tao, W.-K., Lang, S., Simpson, J., Sui, C.-H., Ferrier, B., & Chou, M.-D. (1996). Mechanisms of
1691 Cloud-Radiation Interaction in the Tropics and Midlatitudes. *Journal of the Atmospheric*
1692 *Sciences*, *53*(18), 2624–2651. https://doi.org/10.1175/1520-
1693 0469(1996)053<2624:MOCRII>2.0.CO;2
1694 Tao, W.-K., Chern, J.-D., Atlas, R., Randall, D., Khairoutdinov, M., Li, J.-L., Waliser, D. E., Hou,
1695 A., Lin, X., Peters-Lidard, C., Lau, W., Jiang, J., & Simpson, J. (2009). A Multiscale
1696 Modeling System: Developments, Applications, and Critical Issues. *Bulletin of the American*
1697 *Meteorological Society*, *90*(4), 515–534. https://doi.org/10.1175/2008BAMS2542.1

1698 Tatebe, H., Ogura, T., Nitta, T., Komuro, Y., Ogochi, K., Takemura, T., Sudo, K., Sekiguchi, M.,
1699 Abe, M., Saito, F., Chikira, M., Watanabe, S., Mori, M., Hirota, N., Kawatani, Y., Mochizuki,
1700 T., Yoshimura, K., Takata, K., O'ishi, R., … Kimoto, M. (2019). Description and basic
1701 evaluation of simulated mean state, internal variability, and climate sensitivity in MIROC6.
1702 *Geoscientific Model Development*, *12*(7), 2727–2765. https://doi.org/10.5194/gmd-12-2727-
1703 2019
1704 Thompson, G., Field, P. R., Rasmussen, R. M., & Hall, W. D. (2008). Explicit Forecasts of Winter
1705 Precipitation Using an Improved Bulk Microphysics Scheme. Part II: Implementation of a
1706 New Snow Parameterization. *Monthly Weather Review*, *136*(12), 5095–5115.
1707 https://doi.org/10.1175/2008MWR2387.1
1708 Thompson, G., Tewari, M., Ikeda, K., Tessendorf, S., Weeks, C., Otkin, J., & Kong, F. (2016).
1709 Explicitly-coupled cloud physics and radiation parameterizations and subsequent evaluation
1710 in WRF high-resolution convective forecasts. *Atmospheric Research*, *168*, 92–104.
1711 https://doi.org/10.1016/j.atmosres.2015.09.005
1712 Tomita, H. (2008a). A Stretched Icosahedral Grid by a New Grid Transformation. *Journal of the*
1713 *Meteorological Society of Japan. Ser. II*, *86A*, 107–119.
1714 https://doi.org/10.2151/jmsj.86A.107
1715 Tomita, H. (2008b). New Microphysical Schemes with Five and Six Categories by Diagnostic
1716 Generation of Cloud Ice. *Journal of the Meteorological Society of Japan. Ser. II*, *86A*, 121–
1717 142. https://doi.org/10.2151/jmsj.86A.121
1718 Tomita, H., Tsugawa, M., Satoh, M., & Goto, K. (2001). Shallow Water Model on a Modified
1719 Icosahedral Geodesic Grid by Using Spring Dynamics. *Journal of Computational Physics*,
1720 *174*(2), 579–613. https://doi.org/10.1006/jcph.2001.6897

1721 Tomita, H., & Satoh, M. (2004). A new dynamical framework of nonhydrostatic global model
1722 using the icosahedral grid. *Fluid Dynamics Research*, *34*(6), 357.
1723 https://doi.org/10.1016/j.fluiddyn.2004.03.003
1724 Tomita, H., Miura, H., Iga, S., Nasuno, T., & Satoh, M. (2005). A global cloud-resolving
1725 simulation: Preliminary results from an aqua planet experiment. *Geophysical Research*
1726 *Letters*, *32*(8). https://doi.org/10.1029/2005GL022459
1727 Trenberth, K. E., & Fasullo, J. T. (2010). Simulation of Present-Day and Twenty-First-Century
1728 Energy Budgets of the Southern Oceans. *Journal of Climate*, *23*(2), 440–454.
1729 https://doi.org/10.1175/2009JCLI3152.1
1730 Uchida, J., Mori, M., Nakamura, H., Satoh, M., Suzuki, K., & Nakajima, T. (2016). Error and
1731 Energy Budget Analysis of a Nonhydrostatic Stretched-Grid Global Atmospheric Model.
1732 *Monthly Weather Review*, *144*(4), 1423–1447. https://doi.org/10.1175/MWR-D-15-0271.1
1733 Uchida, J., Mori, M., Hara, M., Satoh, M., Goto, D., Kataoka, T., Suzuki, K., & Nakajima, T.
1734 (2017). Impact of Lateral Boundary Errors on the Simulation of Clouds with a Nonhydrostatic
1735 Regional Climate Model. *Monthly Weather Review*, *145*(12), 5059–5082.
1736 https://doi.org/10.1175/MWR-D-17-0158.1
1737 Vergara-Temprado, J., Ban, N., Panosetti, D., Schlemmer, L., & Schär, C. (2020). Climate Models
1738 Permit Convection at Much Coarser Resolutions Than Previously Considered. *Journal of*
1739 *Climate*, *33*(5), 1915–1933. https://doi.org/10.1175/JCLI-D-19-0286.1
1740 Voldoire, A., Decharme, B., Pianezze, J., Lebeaupin Brossier, C., Sevault, F., Seyfried, L.,
1741 Garnier, V., Bielli, S., Valcke, S., Alias, A., Accensi, M., Ardhuin, F., Bouin, M.-N., Ducrocq,
1742 V., Faroux, S., Giordani, H., Léger, F., Marsaleix, P., Rainaud, R., … Riette, S. (2017).
1743 SURFEX v8.0 interface with OASIS3-MCT to couple atmosphere with hydrology, ocean,

1744 waves and sea-ice models, from coastal to global scales. *Geoscientific Model Development*,
1745 *10*(11), 4207–4227. https://doi.org/10.5194/gmd-10-4207-2017
1746 Voors, R., Donovan, D., Acarreta, J., Eisinger, M., Franco, R., Lajas, D., Moyano, R., Pirondini,
1747 F., Ramos, J., & Wehr, T. (2007). ECSIM: The simulator framework for EarthCARE.
1748 *Sensors, Systems, and Next-Generation Satellites XI*, *6744*, 67441Y.
1749 https://doi.org/10.1117/12.737738
1750 Waliser, D. E., Li, J.-L. F., L'Ecuyer, T. S., & Chen, W.-T. (2011). The impact of precipitating ice
1751 and snow on the radiation balance in global climate models. *Geophysical Research Letters*,
1752 *38*(6). https://doi.org/10.1029/2010GL046478
1753 Walters, D., Baran, A. J., Boutle, I., Brooks, M., Earnshaw, P., Edwards, J., Furtado, K., Hill, P.,
1754 Lock, A., Manners, J., Morcrette, C., Mulcahy, J., Sanchez, C., Smith, C., Stratton, R.,
1755 Tennant, W., Tomassini, L., Van Weverberg, K., Vosper, S., … Zerroukat, M. (2019). The
1756 Met Office Unified Model Global Atmosphere 7.0/7.1 and JULES Global Land 7.0
1757 configurations. *Geoscientific Model Development*, *12*(5), 1909–1963.
1758 https://doi.org/10.5194/gmd-12-1909-2019
1759 Watanabe, M., Emori, S., Satoh, M., & Miura, H. (2009). A PDF-based hybrid prognostic cloud
1760 scheme for general circulation models. *Climate Dynamics*, *33*(6), 795–816.
1761 https://doi.org/10.1007/s00382-008-0489-0
1762 Wedi, N. P. (2014). Increasing horizontal resolution in numerical weather prediction and climate
1763 simulations: Illusion or panacea? *Philosophical Transactions of the Royal Society A:*
1764 *Mathematical, Physical and Engineering Sciences*, *372*(2018), 20130289.
1765 https://doi.org/10.1098/rsta.2013.0289

1766 Wedi, N. P., Polichtchouk, I., Dueben, P., Anantharaj, V. G., Bauer, P., Boussetta, S., Browne, P.,
1767 Deconinck, W., Gaudin, W., Hadade, I., Hatfield, S., Iffrig, O., Lopez, P., Maciel, P., Mueller,
1768 A., Saarinen, S., Sandu, I., Quintino, T., & Vitart, F. (2020). A Baseline for Global Weather
1769 and Climate Simulations at 1 km Resolution. *Journal of Advances in Modeling Earth Systems*,
1770 *12*(11), e2020MS002192. https://doi.org/10.1029/2020MS002192

1771 Weisman, M. L., Skamarock, W. C., & Klemp, J. B. (1997). The Resolution Dependence of
1772 Explicitly Modeled Convective Systems. *Monthly Weather Review*, *125*(4), 527–548.
1773 https://doi.org/10.1175/1520-0493(1997)125<0527:TRDOEM>2.0.CO;2

1774 Wilson, D. R., & Ballard, S. P. (1999). A microphysically based precipitation scheme for the UK
1775 meteorological office unified model. *Quarterly Journal of the Royal Meteorological Society*,
1776 *125*(557), 1607–1636. https://doi.org/10.1002/qj.49712555707

1777 Wing, A. A., Emanuel, K., Holloway, C. E., & Muller, C. (2017). Convective Self-Aggregation in
1778 Numerical Simulations: A Review. *Surveys in Geophysics*, *38*(6), 1173–1197.
1779 https://doi.org/10.1007/s10712-017-9408-4

1780 Winker, D. M., Vaughan, M. A., Omar, A., Hu, Y., Powell, K. A., Liu, Z., Hunt, W. H., & Young,
1781 S. A. (2009). Overview of the CALIPSO Mission and CALIOP Data Processing Algorithms.
1782 *Journal of Atmospheric and Oceanic Technology*, *26*(11), 2310–2323.
1783 https://doi.org/10.1175/2009JTECHA1281.1

1784 Wood, N., Staniforth, A., White, A., Allen, T., Diamantakis, M., Gross, M., Melvin, T., Smith, C.,
1785 Vosper, S., Zerroukat, M., & Thuburn, J. (2014). An inherently mass-conserving semi-
1786 implicit semi-Lagrangian discretization of the deep-atmosphere global non-hydrostatic
1787 equations. *Quarterly Journal of the Royal Meteorological Society*, *140*(682), 1505–1520.
1788 https://doi.org/10.1002/qj.2235

1789 Xiao, F., Okazaki, T., & Satoh, M. (2003). An Accurate Semi-Lagrangian Scheme for Raindrop
1790 Sedimentation. *Monthly Weather Review*, *131*(5), 974–983. https://doi.org/10.1175/1520-
1791 0493(2003)131<0974:AASSFR>2.0.CO;2
1792 Yamada, H., Nasuno, T., Yanase, W., & Satoh, M. (2016). Role of the Vertical Structure of a
1793 Simulated Tropical Cyclone in Its Motion: A Case Study of Typhoon Fengshen (2008). *Sola*,
1794 *12*, 203–208. https://doi.org/10.2151/sola.2016-041
1795 Yamada, Y., Oouchi, K., Satoh, M., Tomita, H., & Yanase, W. (2010). Projection of changes in
1796 tropical cyclone activity and cloud height due to greenhouse warming: Global cloud-system-
1797 resolving approach. *Geophysical Research Letters*, *37*(7).
1798 https://doi.org/10.1029/2010GL042518
1799 Yamada, Y., & Satoh, M. (2013). Response of Ice and Liquid Water Paths of Tropical Cyclones
1800 to Global Warming Simulated by a Global Nonhydrostatic Model with Explicit Cloud
1801 Microphysics. *Journal of Climate*, *26*(24), 9931–9945. https://doi.org/10.1175/JCLI-D-13-
1802 00182.1
1803 Yamada, Y., Satoh, M., Sugi, M., Kodama, C., Noda, A. T., Nakano, M., & Nasuno, T. (2017).
1804 Response of Tropical Cyclone Activity and Structure to Global Warming in a High-
1805 Resolution Global Nonhydrostatic Model. *Journal of Climate*, *30*(23), 9703–9724.
1806 https://doi.org/10.1175/JCLI-D-17-0068.1
1807 Yanase, W., Taniguchi, H., & Satoh, M. (2010). The Genesis of Tropical Cyclone Nargis (2008):
1808 Environmental Modulation and Numerical Predictability. *Journal of the Meteorological*
1809 *Society of Japan. Ser. II*, *88*(3), 497–519. https://doi.org/10.2151/jmsj.2010-314

1810 Yang, P., & Liou, K. N. (1995). Light scattering by hexagonal ice crystals: Comparison of finite-
1811 difference time domain and geometric optics models. *JOSA A*, *12*(1), 162–176.
1812 https://doi.org/10.1364/JOSAA.12.000162
1813 Yang, P., Bi, L., Baum, B. A., Liou, K.-N., Kattawar, G. W., Mishchenko, M. I., & Cole, B. (2013).
1814 Spectrally Consistent Scattering, Absorption, and Polarization Properties of Atmospheric Ice
1815 Crystals at Wavelengths from 0.2 to 100 μm. *Journal of the Atmospheric Sciences*, *70*(1),
1816 330–347. https://doi.org/10.1175/JAS-D-12-039.1
1817 Yang, Q., Leung, L. R., Lu, J., Lin, Y.-L., Hagos, S., Sakaguchi, K., & Gao, Y. (2017). Exploring
1818 the effects of a nonhydrostatic dynamical core in high-resolution aquaplanet simulations.
1819 *Journal of Geophysical Research: Atmospheres*, *122*(6), 3245–3265.
1820 https://doi.org/10.1002/2016JD025287
1821 Yoshida, R., Okamoto, H., Hagihara, Y., & Ishimoto, H. (2010). Global analysis of cloud phase
1822 and ice crystal orientation from Cloud-Aerosol Lidar and Infrared Pathfinder Satellite
1823 Observation (CALIPSO) data using attenuated backscattering and depolarization ratio.
1824 *Journal of Geophysical Research: Atmospheres*, *115*(D4).
1825 https://doi.org/10.1029/2009JD012334
1826 Yoshimura, H. (2012). Development of a nonhydrostatic global spectral atmospheric model using
1827 double Fourier series. CAS/JSC WGNE Research Activities in Atmospheric and Ocean
1828 Modeling, 42, 3.05–3.06.
1829 Zängl, G., Reinert, D., Rípodas, P., & Baldauf, M. (2015). The ICON (ICOsahedral Non-
1830 hydrostatic) modelling framework of DWD and MPI-M: Description of the non-hydrostatic
1831 dynamical core. *Quarterly Journal of the Royal Meteorological Society*, *141*(687), 563–579.
1832 https://doi.org/10.1002/qj.2378

1833 Zhang, F., Sun, Y. Q., Magnusson, L., Buizza, R., Lin, S.-J., Chen, J.-H., & Emanuel, K. (2019).
1834 What Is the Predictability Limit of Midlatitude Weather? *Journal of the Atmospheric*
1835 *Sciences*, *76*(4), 1077–1091. https://doi.org/10.1175/JAS-D-18-0269.1
1836 Zhang, G., Xue, M., Cao, Q., & Dawson, D. (2008). Diagnosing the Intercept Parameter for
1837 Exponential Raindrop Size Distribution Based on Video Disdrometer Observations: Model
1838 Development. *Journal of Applied Meteorology and Climatology*, *47*(11), 2983–2992.
1839 https://doi.org/10.1175/2008JAMC1876.1
1840 Zhang, M., Bretherton, C. S., Blossey, P. N., Austin, P. H., Bacmeister, J. T., Bony, S., Brient, F.,
1841 Cheedela, S. K., Cheng, A., Genio, A. D. D., Roode, S. R. D., Endo, S., Franklin, C. N.,
1842 Golaz, J.-C., Hannay, C., Heus, T., Isotta, F. A., Dufresne, J.-L., Kang, I.-S., … Zhao, M.
1843 (2013). CGILS: Results from the first phase of an international project to understand the
1844 physical mechanisms of low cloud feedbacks in single column models. *Journal of Advances*
1845 *in Modeling Earth Systems*, *5*(4), 826–842. https://doi.org/10.1002/2013MS000246
1846 Zhang, S., Fu, H., Wu, L., Li, Y., Wang, H., Zeng, Y., Duan, X., Wan, W., Wang, L., Zhuang, Y.,
1847 Meng, H., Xu, K., Xu, P., Gan, L., Liu, Z., Wu, S., Chen, Y., Yu, H., Shi, S., … Guo, Y.
1848 (2020). Optimizing high-resolution Community Earth System Model on a heterogeneous
1849 many-core supercomputing platform. *Geoscientific Model Development*, *13*(10), 4809–4829.
1850 https://doi.org/10.5194/gmd-13-4809-2020
1851 Zhang, Y., Li, J., Yu, R., Zhang, S., Liu, Z., Huang, J., & Zhou, Y. (2019). A Layer-Averaged
1852 Nonhydrostatic Dynamical Framework on an Unstructured Mesh for Global and Regional
1853 Atmospheric Modeling: Model Description, Baseline Evaluation, and Sensitivity
1854 Exploration. *Journal of Advances in Modeling Earth Systems*, *11*(6), 1685–1714.
1855 https://doi.org/10.1029/2018MS001539

Zhang, Y., Li, J., Yu, R., Liu, Z., Zhou, Y., Li, X., & Huang, X. (2020). A Multiscale Dynamical Model in a Dry-Mass Coordinate for Weather and Climate Modeling: Moist Dynamics and Its Coupling to Physics. *Monthly Weather Review*, *148*(7), 2671–2699. https://doi.org/10.1175/MWR-D-19-0305.1

Zhou, L., Lin, S.-J., Chen, J.-H., Harris, L. M., Chen, X., & Rees, S. L. (2019). Toward Convective-Scale Prediction within the Next Generation Global Prediction System. *Bulletin of the American Meteorological Society*, *100*(7), 1225–1243. https://doi.org/10.1175/BAMS-D-17-0246.1

Figure Captions and Tables

Figure 1. Typical spatiotemporal scales of some examples of weather and climate phenomena. The numerical weather prediction model (NWP), general circulation model (GCM), and global cloud resolving model (GCRM) cover different but partially overlapping scales.

Figure 2. Cloud images calculated by the GCRMs in the DYAMOND project and from the geostationary satellite Himawari-8 (After Fig. 2 in Stevens et al., 2019). From left to right: IFS with a horizontal resolution of 4 km, 9 km, and NICAM (top row); ARPEGE-NH, Himawari-8, and ICON (second row); FV3, GEOS5, and UM (third row); and SAM and MPAS (bottom row).

Figure 3. Cloud images calculated by the NICAM with horizontal resolutions of 14 km, 3.5 km and 0.87 km (after Kajikawa et al., 2016). Zoom images of a tropical cyclone are shown in the right column.

1880 Figure 4. A schematic image of the comparison between models and satellites using satellite
1881 simulators. From Masunaga et al. (2010), © American Meteorological Society. Used with
1882 permission.
1883
1884 Figure 5. Sample images of (a) the default NICAM with the global quasi-uniform icosahedral
1885 grid system, (b) stretched NICAM, and (c) diamond NICAM (after Uchida et al., 2017, ©
1886 American Meteorological Society. Used with permission.).
1887
1888 Figure 6. Comparison of the vertical profiles of annual mean ice water content (IWC) [mg m-
1889 3] from (a) CloudSat satellite observations [2B-CWC-RO product (Austin and Stephens 2001;
1890 Austin et al., 2009)], (b) NSW6 in NICAM.12, (c) NSW6 in NICAM.16, and NDW6 in NICAM.16.
1891 The solid lines represent 273-K isotherms. The global simulation data with horizontal resolution
1892 of 14 km and 38 vertical layers were provided by courtesy of C. Kodama and A. T. Noda.
1893
1894 Figure 7. Comparison of outgoing longwave radiation at the top of the atmosphere (OLR)
1895 from CERES satellite observations (solid lines with points) and NICAM simulations with various
1896 versions of NDW6 (solid lines) (after Satoh et al., 2018).
1897
1898 Figure 8. The vertical profiles of (a) downward shortwave radiation and (b) upward shortwave
1899 radiation (after Seiki et al., 2014). Thick lines indicate observations by radiometer sonde, thin solid
1900 lines indicate NICAM simulations using NDW6 with spherical SSPs, and thin dashed lines
1901 indicate NICAM simulations using NDW6 with nonspherical SSPs. The dashed rectangles indicate
1902 the location of a cirrus layer.

Figure 9. Comparison of (a) OLR and (b) outgoing shortwave radiation at the top of the atmosphere (OSR) from CERES satellite observations (solid lines) and NICAM.16 simulations with various settings of cloud and radiation coupling. NSW6 uses full coupling between cloud and radiation (dashed lines), NSW6-Mie assumes variable effective radii but spherical SSPs (long dashed short dashed lines), and NSW6-Mie-ReFIX assumes constant effective radii and spherical SSPs (dotted lines). The global simulation data were provided by courtesy of C. Kodama.

Figure 10. Cloud microphysical processes and cloud interaction among water classes (after Satoh et al., 2018). Solid lines indicate the processes that change the number and mass concentration of hydrometeors, while dashed lines indicate the processes that change only the mass concentration of hydrometeors. Hom/het indicates homogeneous/heterogeneous, respectively.

Figure 11. Breakdown of OLR change under global warming simulated by the NICAM (after Noda et al., 2016). An OLR change ΔF is attributed to a change in emissivity $\Delta\varepsilon$, a change in cloud-top temperature ΔT_{CT}, and a change in clear sky radiation ΔF^{CLR}. The breakdown was calculated by cloud size. Sum shows the summation of the contributions and the difference between ΔF and Sum indicates the error of the analysis.

Figure 12. The cloud-top and rain-top diagram using Ku-band radar echo and infrared brightness temperature from (a) satellite observations, (c) NSW6 in NICAM.12, and (e) NSW6 in NICAM.16. CFAD using Ku-band radar echo from (b) satellite observations, (d) NSW6 in

1926 NICAM.12, and (f) NSW6 in NICAM.16. Here, simulated results were processed by a Joint-
1927 Simulator. From Roh et al. (2017), © American Meteorological Society. Used with permission.
1928
1929 Figure 13. Joint probability density function of the depolarization ratio δ and the ratio of
1930 attenuated backscattering coefficients for successive layers x from (a) satellite observations, (b)
1931 NSW6 in NICAM.16, and (c) NDW6. Low-level clouds behind a frontal cloud system were
1932 sampled over the Southern Ocean. Signals of supercooled liquid water are highlighted by circles.
1933 From Roh et al. (2020), © American Meteorological Society. Used with permission.
1934
1935 Figure 14. Observation geometry of the EarthCARE satellite (from
1936 https://directory.eoportal.org/web/eoportal/satellite-missions/e/earthcare).
1937
1938 Figure 15. Overview of the ground observations used in the ULTIMATE project around the
1939 Tokyo metropolitan area.
1940
1941 Table 1. List of acronyms of models, satellites, and instruments.
1942
1943 Table 2. List of GCRMs. Short names and references to the model-frameworks and recent
1944 settings are summarized.
1945
1946 Table 3. GCRMs and cloud microphysics used for the DYAMOND project. The subscripts v,
1947 c, r, i, s, and g indicate vapor, cloud water, rain, cloud ice, snow, and graupel categories,
1948 respectively.

1949

1950 Table 4. Dependences of cloud-related processes on bulk cloud microphysical parameters.

1951

1952 Table 5. Optical sensors and corresponding sensitive physical parameters.

1 Table 1. List of acronyms of models, satellites, and instruments.

Acronym	Long name
AMSR-E	Advanced Microwave Scanning Radiometer-EOS
AROME	Applications of Research to Operations at Mesoscale
ARPEGE-NH	Action de Recherche Petite Echelle Grande Echelle-NonHydrostatic version
CALIPSO/CALIOP	Cloud-Aerosol Lidar and Infrared Pathfinder Satellite Observations/Cloud-Aerosol LIdar with Orthogonal Polarization
CAM	Community Atmosphere Model
COSP	The cloud feedback model intercomparison project Observation Simulator Package
CPR	Cloud Profiling Radar
CRTM	Community Radiative Transfer Model
DFSM	Double Fourier Series Model
EarthCARE	Earth Clouds, Aerosols and Radiation Explorer
ECHAM	European Centre Hamburg model
ECSIM	EarthCARE Simulator
FV3	Finite-Volume Cubed-Sphere Dynamical Core
GCOM-C/SGLI	Global Change Observation Mission-Climate/ Second-generation Global Imager
GEOS	Goddard Earth Observing System
GOES	Geostationary Operational Environmental Satellite
GPM/DPR/GMI	Global Precipitation Measurement mission/Dual-frequency Precipitation Radar/GPM Microwave Imager
GRIST	Global-to-Regional Integrated forecast SysTem
ICON	ICOsahedral Non-hydrostatic atmospheric model
IFS	Integrated Forecasting System
MIROC	Model for Interdisciplinary Research on Climate
MODIS	Moderate Resolution Imaging Spectroradiometer
MSSG	Multi-Scale Simulator for the Geoenvironment
MPAS	Model for Prediction Across Scales
MTSAT	Multi-functional Transport Satellite
NICAM	Nonhydrostatic ICosahedral Atmospheric Model
NOAA/AVHRR	National Oceanic and Atmospheric Administration /Advanced Very High Resolution Radiometer
POLARRIS	POLArimetric Radar Retrieval and Instrument Simulator
RTTOV	Radiative Transfer for the TIROS Operational Vertical Sounder
SAM	System for Atmospheric Modeling
SCALE	Scalable Computing for Advanced Library and Environment
SDSU	Satellite Data Simulator Unit
TRMM/PR/VIRS/TMI	Tropical Rainfall Measuring Mission/Precipitation Radar/ Visible Infrared Scanner/ TRMM Microwave Imager
UM	Unified Model
WRF	Weather Research and Forecasting Model

2

Table 2. List of GCRMs. Short names and references to the model-frameworks and recent settings are summarized.

Model name	References
ARPEGE-NH	Bubnová et al. (1995) Voldoire et al. (2017)
DFSM	Yoshimura (2012)
FV3	Lin and Rood (1997) Lin (2004), Zhou et al. (2019)
GEOS5	Putman and Lin (2007), Putman and Suarez (2011), Arnold et al. (2020)
GRIST	Zhang et al. (2019; 2020)
ICON	Zängl et al. (2014), Hohenegger et al. (2020)
IFS	Malardel et al. (2016), Dueben et al. (2020), Wedi et al. (2020)
MSSG	Takahashi et al. (2008), Sasaki et al. (2016), Ohnishi et al. (2019)
MPAS	Skamarock et al. (2012)
NICAM	Satoh et al. (2014), Kodama et al. (2021)
SAM	Khairoutdinov and Randall (2003), Satoh et al. (2019)
UM	Wood et al. (2014), Walters et al. (2019)

Table 3. GCRMs and cloud microphysics used for the DYAMOND project. The subscripts v, c, r, i, s, and g indicate vapor, cloud water, rain, cloud ice, snow, and graupel categories, respectively.

Model name	Cloud microphysics schemes
ARPAGE-NH	SMB with five categories (v, c, r, i, and s) Roehrig et al. (2020)
FV3	SMB with six categories (v, c, r, i, s, and g) Lin et al. (1983), Zhou et al. (2019)
GEOS	SMB with six categories (v, c, r, i, s, and g) Lin et al. (1983), Zhou et al. (2019)
ICON	SMB with six categories (v, c, r, i, s, and g) Lin et al. (1983), Baldauf et al. (2011)
IFS	SMB with five categories (v, c, r, i, and s) Forbes et al. (2011)
MPAS	Hybrid of SMB and DMB with six categories [v, c, r, i, s, and g (the number concentrations of rain and cloud ice are predicted with prescribed aerosols)] Thompson et al. (2008) modified for WRF 3.8.1.
NICAM	SMB with six categories (v, c, r, i, s, and g) Lin et al. (1983), Tomita (2008b), Roh and Satoh (2014)
SAM	SMB with six categories [v, c, r, i, s, and g (ice categories are diagnosed)] Khairoutdinov and Randall (2003)
UM	SMB with four categories [v, c, r, and i (cloud number concentration is diagnosed with climatological distribution of aerosols)] Wilson and Ballard (1999), Boutle et al. (2014), Walters et al. (2019)

11 Table 4. Dependences of cloud-related processes on bulk cloud microphysical parameters.

Processes	Dependences	References	Assumptions
Auto-conversion ($c \rightarrow r$)	$\rho \frac{\partial q_c}{\partial t} \propto (\rho q_c)^2 \overline{D_c}^6$	Seifert and Beheng (2001)	Long's kernel (Long, 1974) is used for the collection efficiency.
Auto-conversion ($i \rightarrow s$)	$\rho \frac{\partial q_i}{\partial t} \propto \rho q_i n_i \overline{D_i}^4$	Seiki et al. (2015)	Cloud ice is assumed to be spherical and sufficiently small to satisfy Stoke's law. $v_{t,i} \propto D^2$
Riming ($c \rightarrow j$) ($j = i, s, g$)	$\rho \frac{\partial q_j}{\partial t} \propto \rho q_c n_j \overline{D_j}^{2+d}$	Seiki and Roh (2020)	Power law is assumed between v_t and D as follows: $v_t \propto D^d$ with d typically ranging from 0.1 to 0.5 (e.g., Locatelli and Hobbs, 1974).
Condensation Evaporation Vapor Deposition Sublimation Melting	$\rho \frac{\partial q_j}{\partial t} \propto n_j \overline{D_j}$	Igel et al. (2015) Seiki and Roh (2020)	Spherical shape is assumed for ice particles.
Immersion freezing	$\rho \frac{\partial q_r}{\partial t} \propto \rho q_r \overline{D_r}^3$	Bigg (1953)	The equation is derived from experiment.
Cloud optical thickness τ_c	$\tau_c \propto n_c \overline{D_c}^2$	Liou (2002)	Extinction efficiency is assumed to be approximately constant (2) for most particles.
Visible cloud albedo R_c	$R_c = \frac{\sqrt{3}(1-g)\tau_c}{2+\sqrt{3}(1-g)\tau_c}$	Liou (2002) Fu (2007)	Two-stream approximation is used with the asymmetry factor g typically ranging from 0.75 to 0.9 (e.g., Fu, 2007)
Infrared emissivity of cirrus ε_{IR}	$\varepsilon_{IR} = 1 - \exp(-0.79\tau_c)$	Fu and Liou (1993)	The function is derived by fitting to results from a numerical model with experimental data.

12

13 Table 5. Optical sensors and corresponding sensitive physical parameters.

Optical sensors	Satellites/instruments	Physical parameters
Visible/near-infrared imager (0.3 to 4 μm)	Geostationary meteorological satellites (e.g., GOES, Himawari, Meteosat), NOAA/AVHRR, Aqua, Terra/MODIS, GCOM-C/SGLI, TRMM-VIRS	Cloud optical thickness, Cloud-top effective radius
Infrared imager (8 to 12 μm)		Cloud-top temperature, Ice cloud optical thickness Ice cloud-top effective radius
Microwave imager (10 to 20 GHz)	Aqua/AMSR-E, GCOM-W/AMSR2, TRMM/TMI, GPM/GMI	Liquid water path, Precipitation flux,
Microwave imager (80 to 90 GHz)		Ice water path
Lidar (532 nm, 1064 nm)	CALIPSO/CALIOP	Thermodynamic phase, Ice shape, Optical thickness
Cloud radar (94 GHz)	CloudSat/CPR	Ice water content, Liquid water content
Precipitation radar (13.6 GHz, 35.5 GHz)	TRMM/PR, GPM/DPR	Precipitation flux, Hydrometeor class

14

15

Figures and Tables

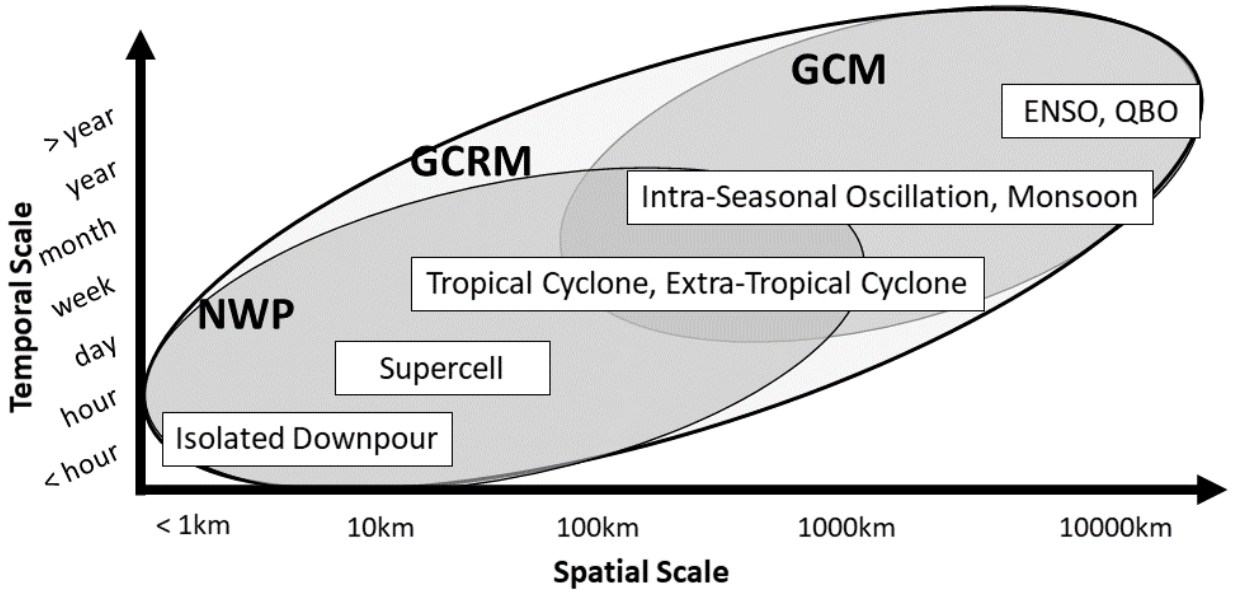

Figure 1. Typical spatiotemporal scales of some examples of weather and climate phenomena. The numerical weather prediction model (NWP), general circulation model (GCM), and global cloud resolving model (GCRM) cover different but partially overlapping scales.

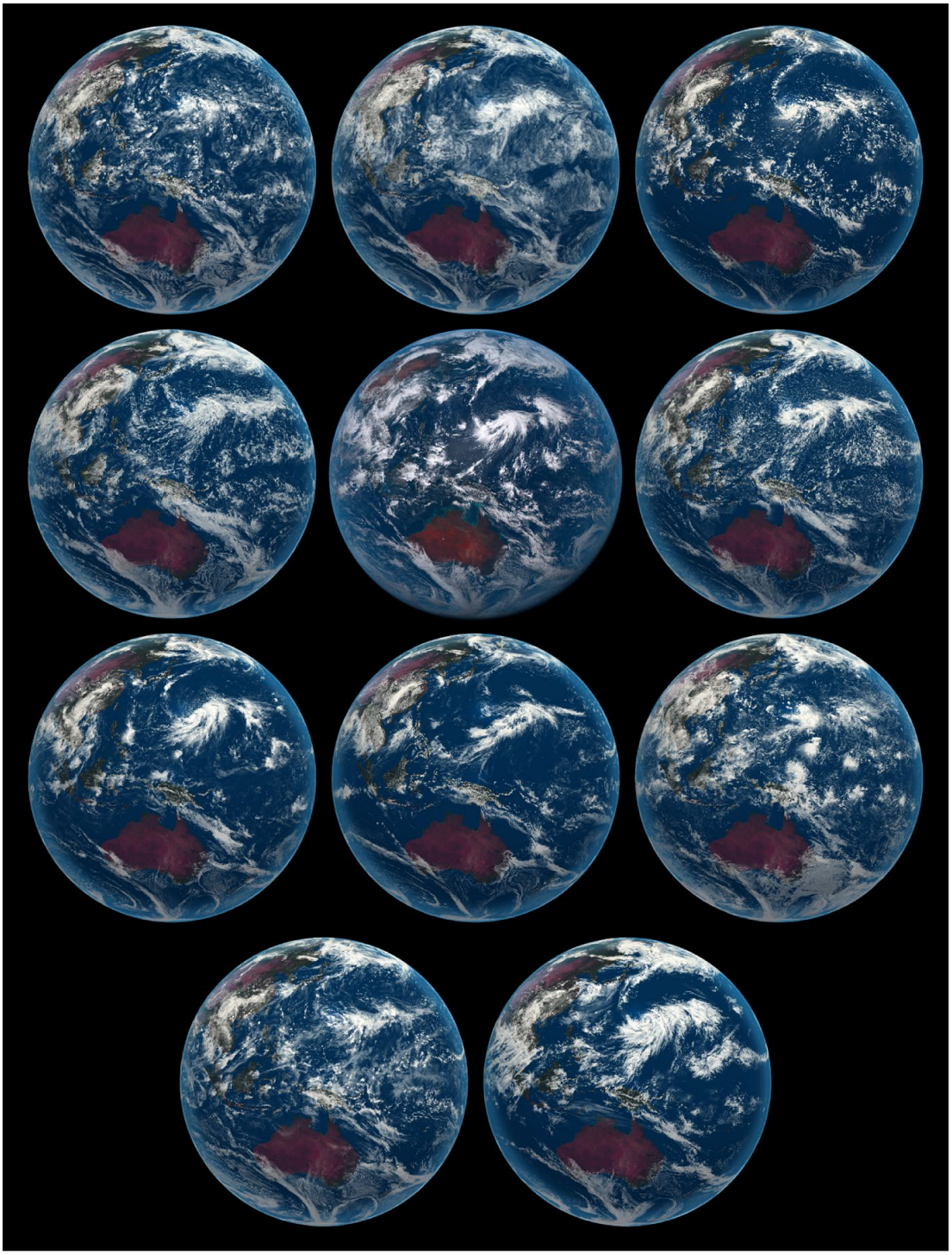

Figure 2. Cloud images calculated by the GCRMs in the DYAMOND project and from the geostationary satellite Himawari-8 (After Fig. 2 in Stevens et al., 2019). From left to right: IFS with a horizontal resolution of 4 km, 9 km, and NICAM (top row); ARPEGE-NH, Himawari-8, and ICON (second row); FV3, GEOS5, and UM (third row); and SAM and MPAS (bottom row).

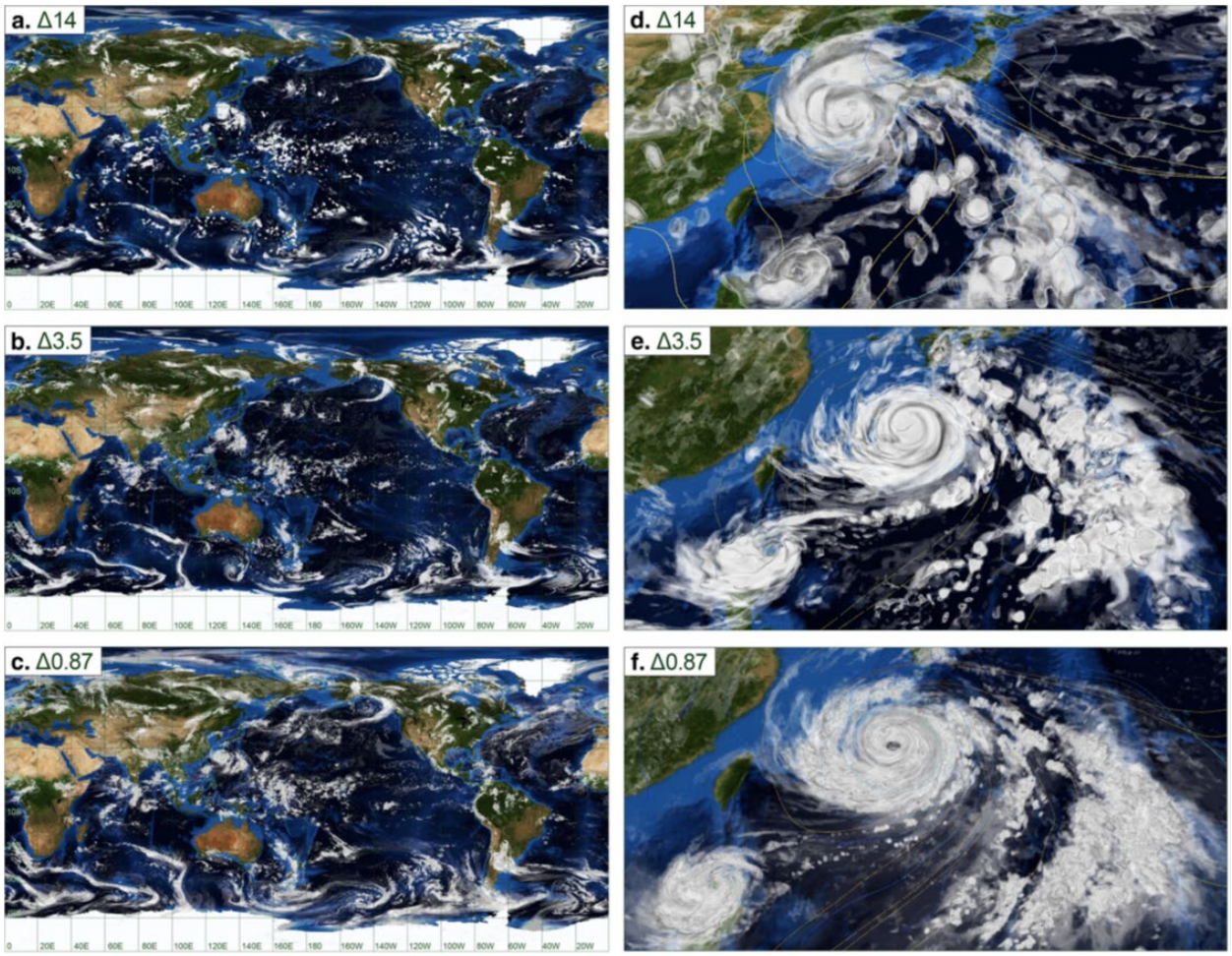

Figure 3. Cloud images calculated by the NICAM with horizontal resolutions of 14 km, 3.5 km and 0.87 km (after Kajikawa et al., 2016). Zoom images of a tropical cyclone are shown in the right column.

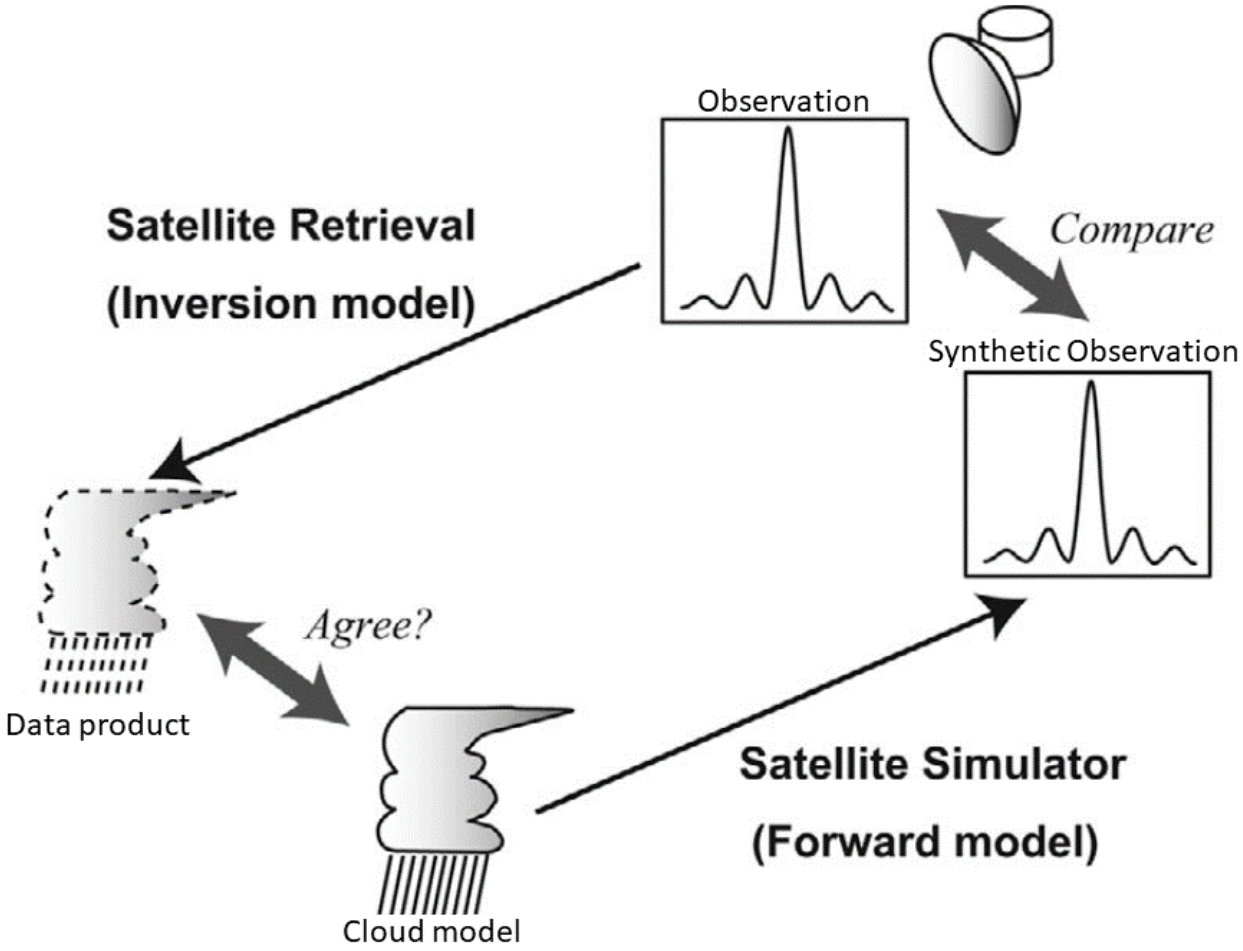

Figure 4. A schematic image of the comparison between models and satellites using satellite simulators. From Masunaga et al. (2010), © American Meteorological Society. Used with permission.

28

29

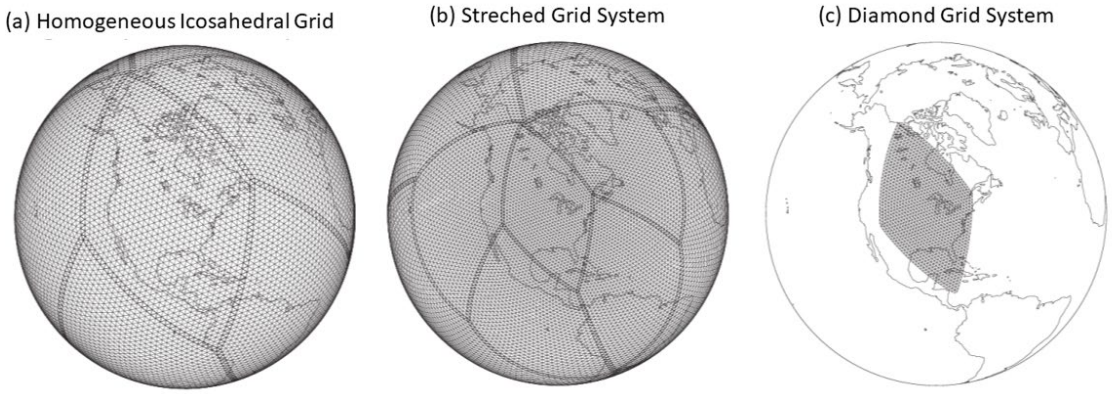

30

31 Figure 5. Sample images of (a) the default NICAM with the global quasi-uniform icosahedral grid
32 system, (b) stretched NICAM, and (c) diamond NICAM (after Uchida et al., 2017, © American
33 Meteorological Society. Used with permission.).
34

35

36

37

38

39

40

41

42

43

44

45

46

47

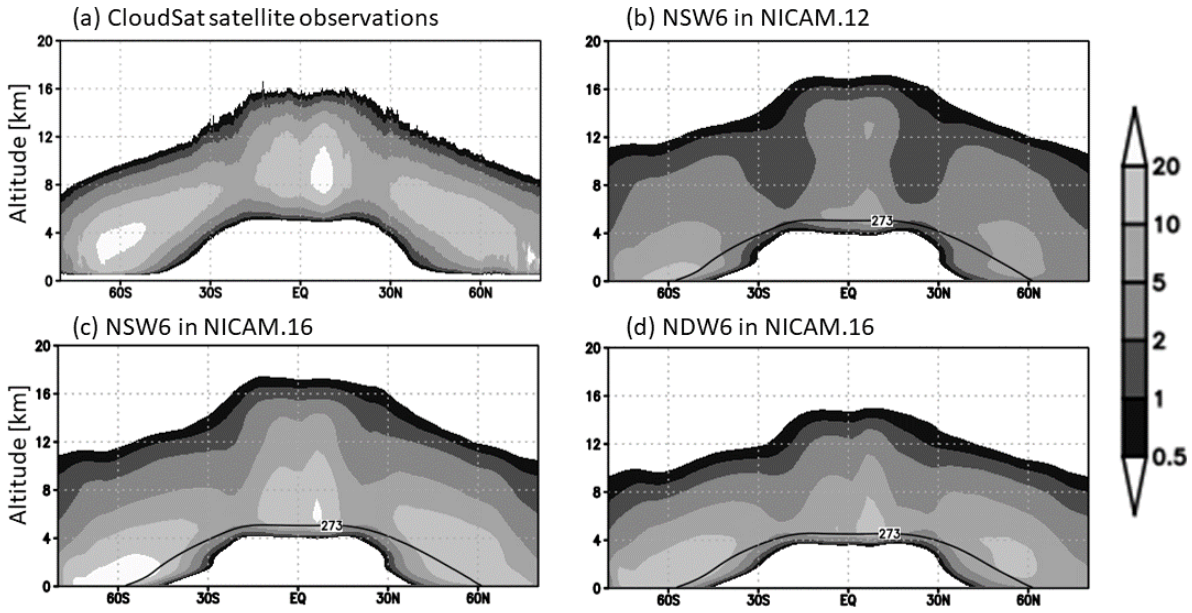

Figure 6. Comparison of the vertical profiles of annual mean ice water content (IWC) [mg m^{-3}] from (a) CloudSat satellite observations [2B-CWC-RO product (Austin and Stephens 2001; Austin et al., 2009)], (b) NSW6 in NICAM.12, (c) NSW6 in NICAM.16, and NDW6 in NICAM.16. The solid lines represent 273-K isotherms. The global simulation data with horizontal resolution of 14 km and 38 vertical layers were provided by courtesy of C. Kodama and A. T. Noda.

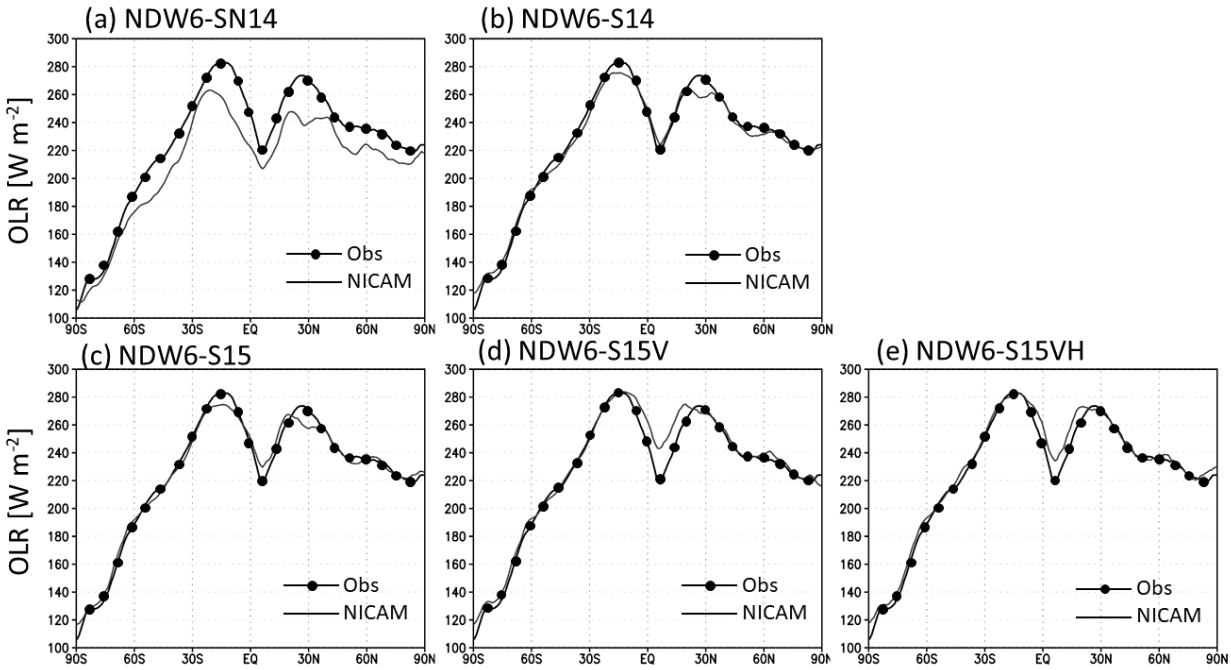

Figure 7. Comparison of outgoing longwave radiation at the top of the atmosphere (OLR) from CERES satellite observations (solid lines with points) and NICAM simulations with various versions of NDW6 (solid lines) (after Satoh et al., 2018).

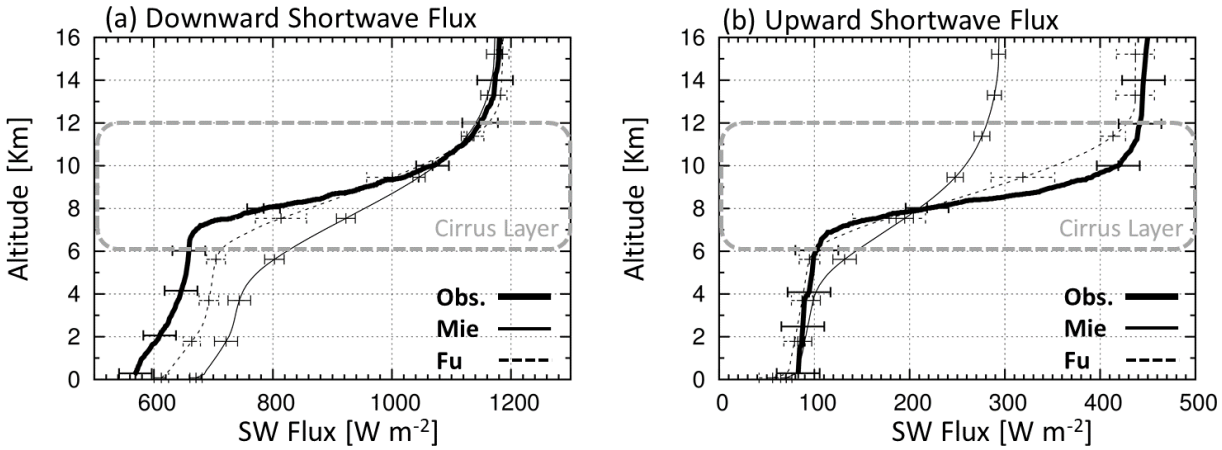

Figure 8. The vertical profiles of (a) downward shortwave radiation and (b) upward shortwave radiation (after Seiki et al., 2014). Thick lines indicate observations by radiometer sonde, thin solid lines indicate NICAM simulations using NDW6 with spherical SSPs, and thin dashed lines indicate NICAM simulations using NDW6 with nonspherical SSPs. The dashed rectangles indicate the location of a cirrus layer.

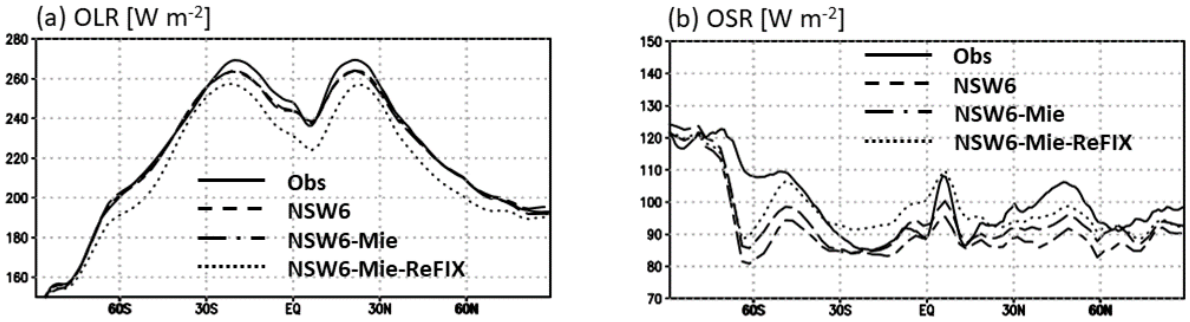

92

93 Figure 9. Comparison of (a) OLR and (b) outgoing shortwave radiation at the top of the atmosphere
94 (OSR) from CERES satellite observations (solid lines) and NICAM.16 simulations with various
95 settings of cloud and radiation coupling. NSW6 uses full coupling between cloud and radiation
96 (dashed lines), NSW6-Mie assumes variable effective radii but spherical SSPs (long dashed short
97 dashed lines), and NSW6-Mie-ReFIX assumes constant effective radii and spherical SSPs (dotted
98 lines). The global simulation data were provided by courtesy of C. Kodama.
99

100

101

102

103

104

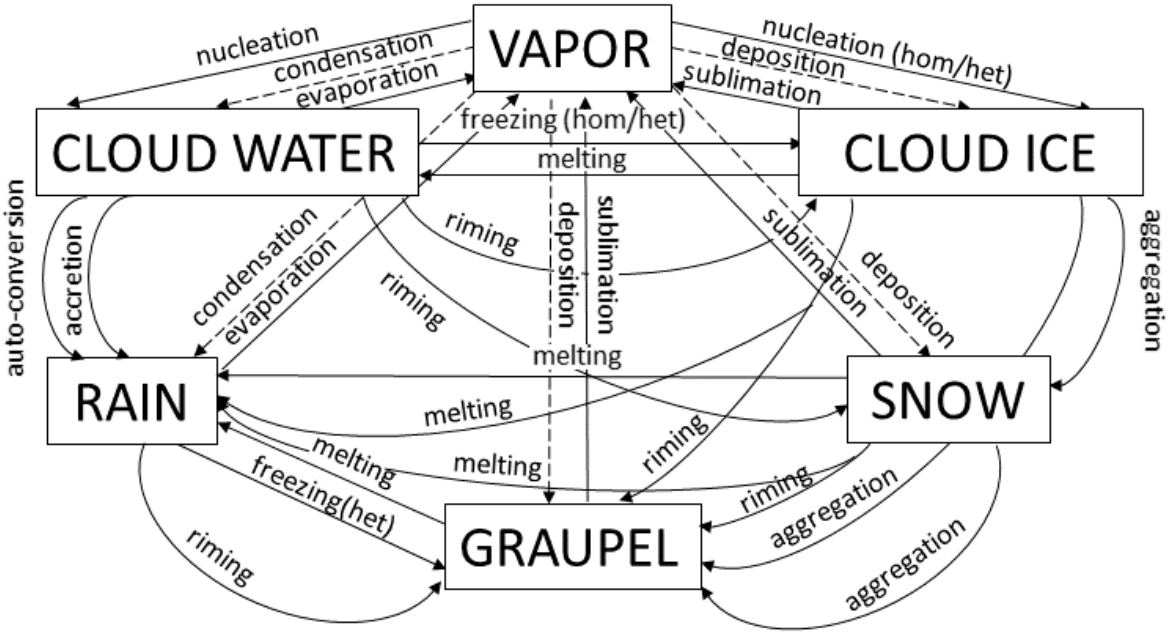

Figure 10. Cloud microphysical processes and cloud interaction among water classes (after Satoh et al., 2018). Solid lines indicate the processes that change the number and mass concentration of hydrometeors, while dashed lines indicate the processes that change only the mass concentration of hydrometeors. Hom/het indicates homogeneous/heterogeneous, respectively.

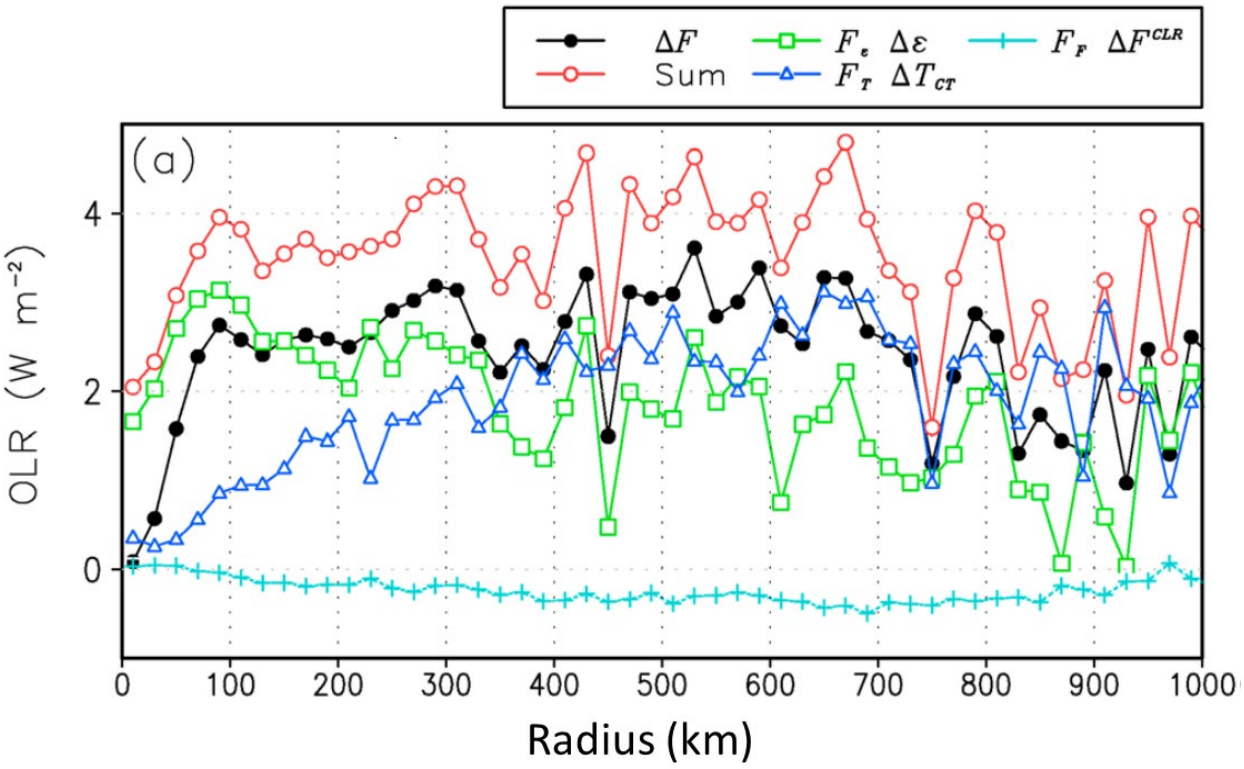

Figure 11. Breakdown of OLR change under global warming simulated by the NICAM (after Noda et al., 2016). An OLR change ΔF is attributed to a change in emissivity $\Delta\varepsilon$, a change in cloud-top temperature ΔT_{CT}, and a change in clear sky radiation ΔF^{CLR}. The breakdown was calculated by cloud size. Sum shows the summation of the contributions and the difference between ΔF and Sum indicates the error of the analysis.

129

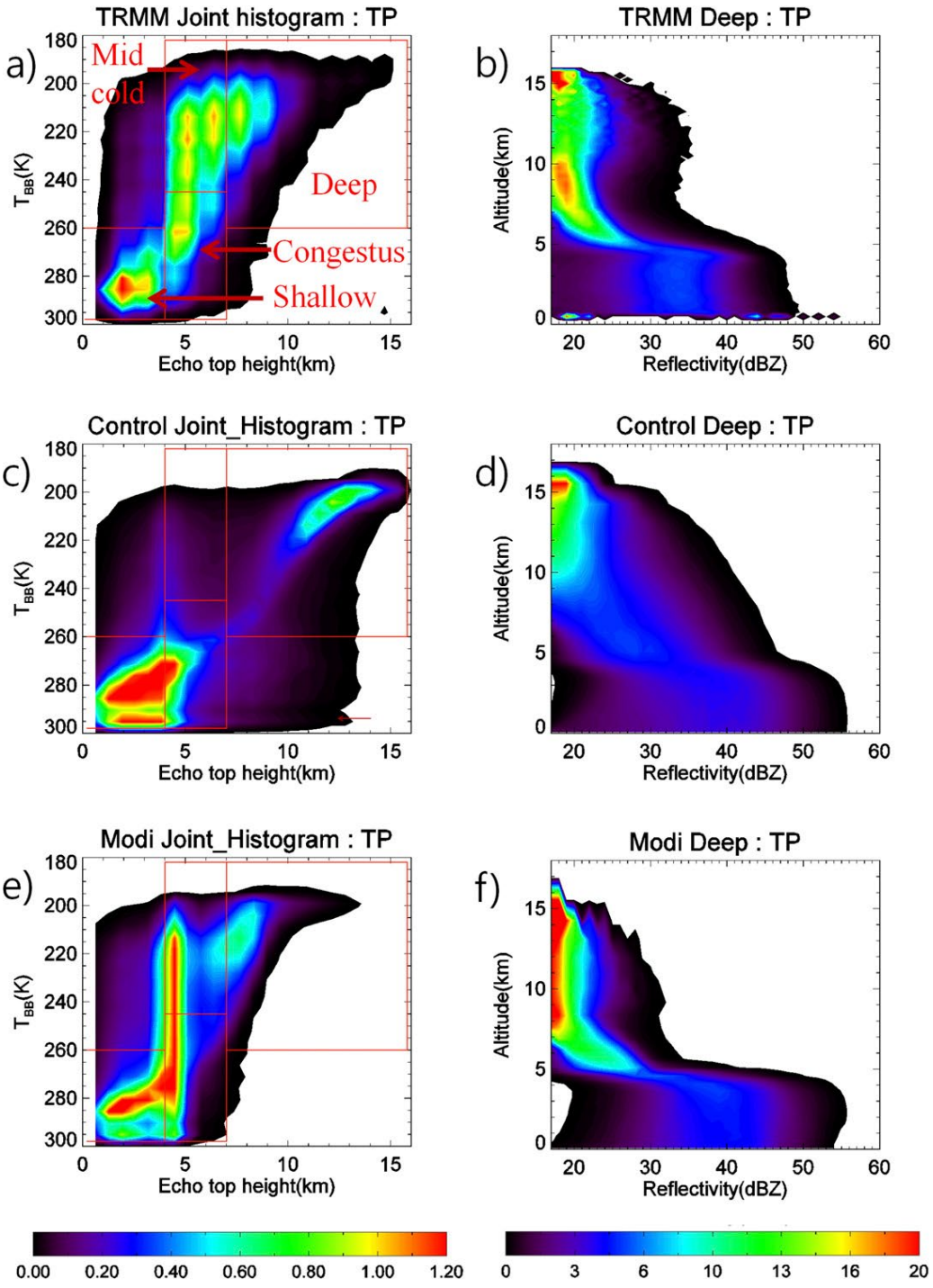

130

131 Figure 12. The cloud-top and rain-top diagram using Ku-band radar echo and infrared brightness
132 temperature from (a) satellite observations, (c) NSW6 in NICAM.12, and (e) NSW6 in NICAM.16.
133 CFAD using Ku-band radar echo from (b) satellite observations, (d) NSW6 in NICAM.12, and (f)
134 NSW6 in NICAM.16. Here, simulated results were processed by a Joint-Simulator. From Roh et
135 al. (2017), © American Meteorological Society. Used with permission.

136

137

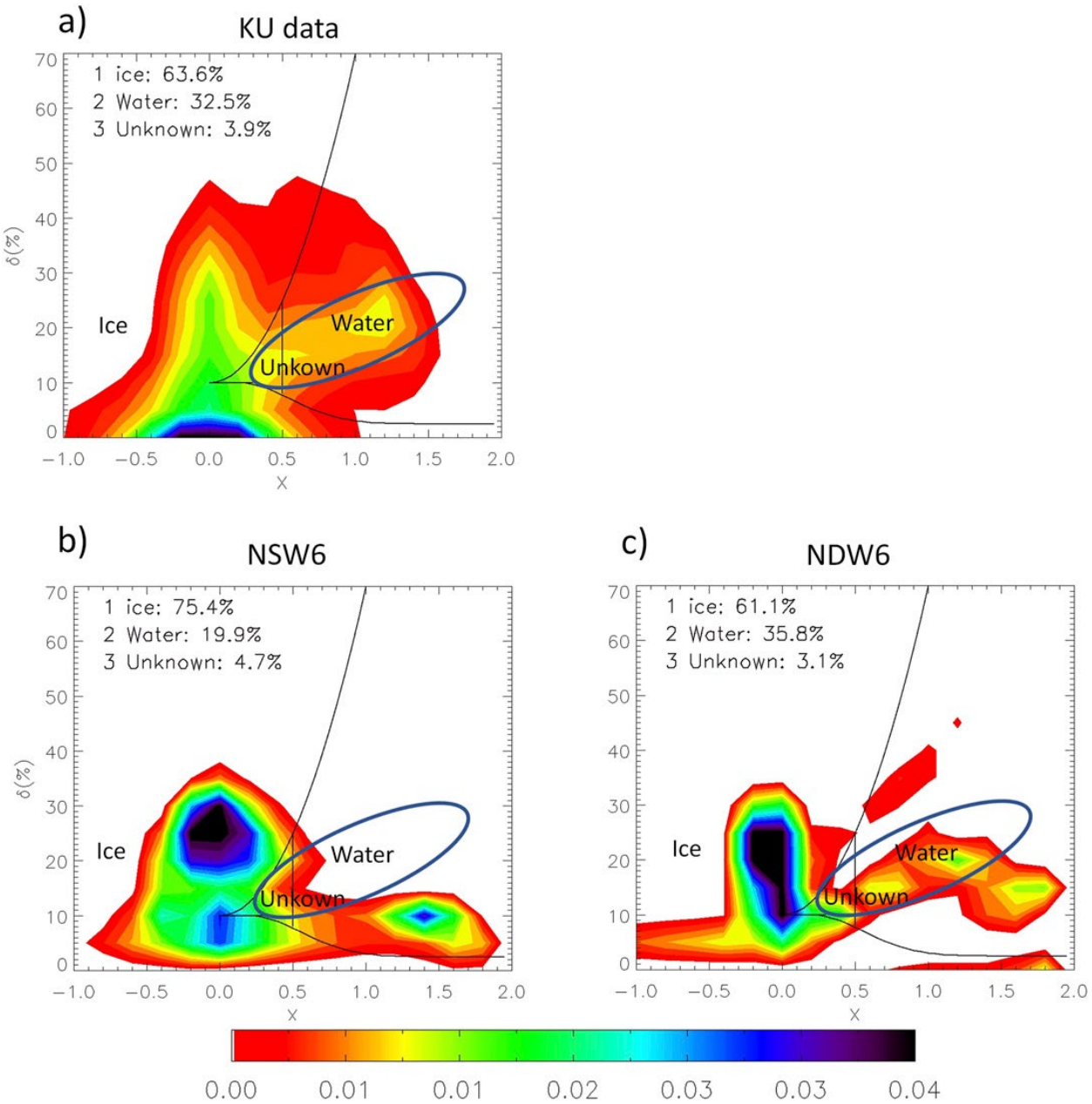

138

139 Figure 13. Joint probability density function of the depolarization ratio δ and the ratio of attenuated
140 backscattering coefficients for successive layers x from (a) satellite observations, (b) NSW6 in
141 NICAM.16, and (c) NDW6. Low-level clouds behind a frontal cloud system were sampled over
142 the Southern Ocean. Signals of supercooled liquid water are highlighted by circles. From Roh et
143 al. (2020), © American Meteorological Society. Used with permission.
144

145

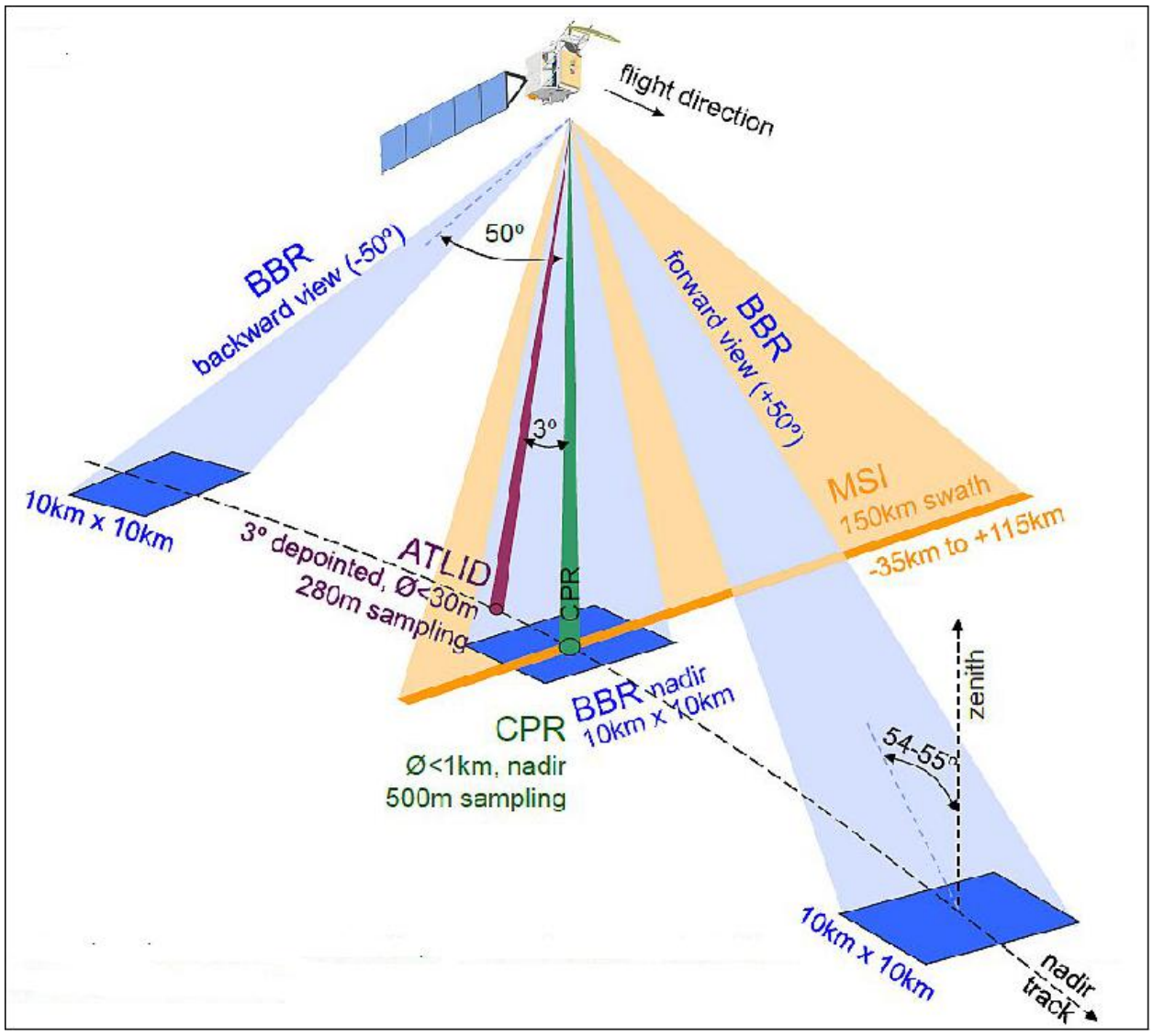

146

147 Figure 14. Observation geometry of the EarthCARE satellite (from
148 https://directory.eoportal.org/web/eoportal/satellite-missions/e/earthcare).
149
150

151

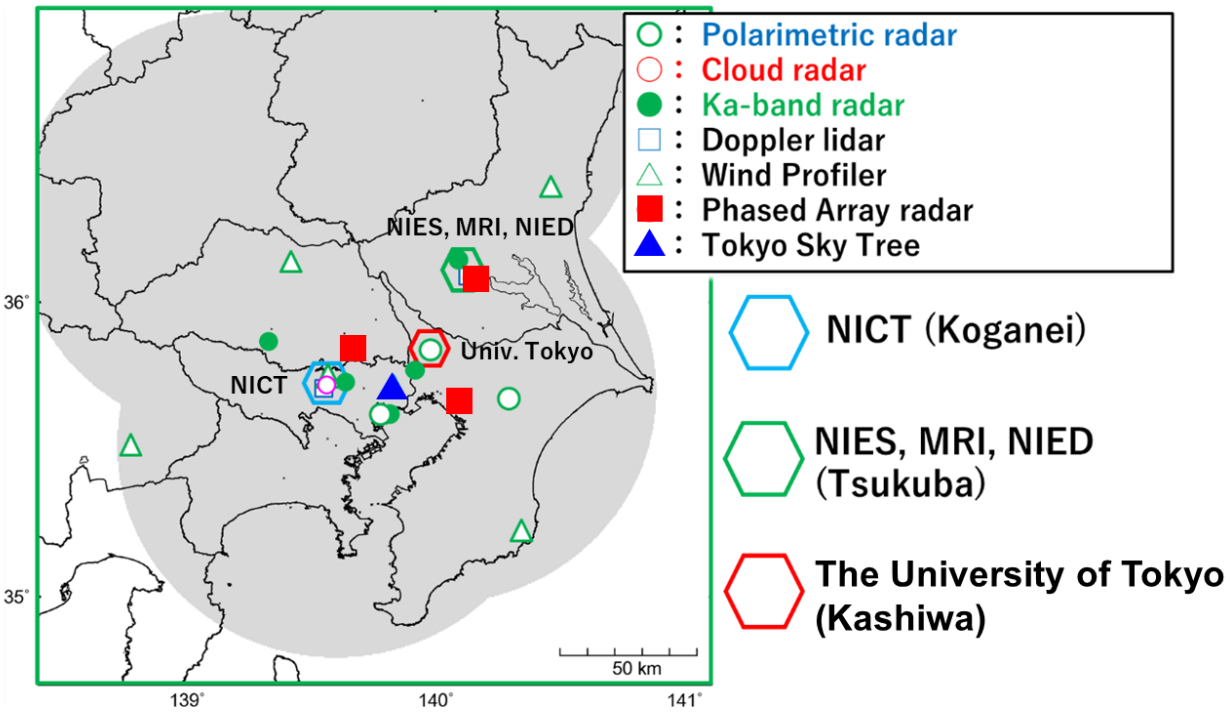

Figure. 15. Overview of the ground observations used in the ULTIMATE project around the Tokyo metropolitan area.